2-13-2014

Modeling the Mechanical Response of Polycrystalline Thin Films

Pedro Joaquin Madrid

Recommended Citation

Madrid, Pedro Joaquin. "Modeling the Mechanical Response of Polycrystalline Thin Films." (2014).
https://digitalrepository.unm.edu/math_etds/26

Pedro Joaquín Madrid Ramírez

Candidate

Mathematics and Statistics

Department

This dissertation is approved, and it is acceptable in quality and form for publication:

Approved by the Dissertation Committee:

Deborah Sulsky , Chairperson

Evangelos Coutsias

Jens Lorenz

Yu-Lin Shen

Modeling the Mechanical Response of Polycrystalline Thin Films

by

Pedro Joaquín Madrid Ramírez

M.Sc., Mathematics, University of New Mexico, 2011

DISSERTATION

Submitted in Partial Fulfillment of the
Requirements for the Degree of

Doctor of Philosophy
Mathematics

The University of New Mexico

Albuquerque, New Mexico

December, 2013

Dedication

I dedicate this thesis to the following people:

My mother Martha Lilia Ramírez de Madrid.

My late father José Arnulfo Madrid Aguilar.

My sister Lizbeth Suyapa Madrid Ramírez.

My brothers Ramón Francisco Madrid Ramírez and Luis Felipe Madrid Ramírez.

"God used beautiful mathematics in creating the world". –Paul Dirac

Acknowledgments

I want to express my gratitude to the following people, without their help this dissertation would not be possible:

Professor Deborah Sulsky for giving me the opportunity of doing research in the fields of materials science and solid mechanics, for her tremendous patience, for her valuable advices about my career and personal life. I have a special admiration to her verbal expression, her broad comprehension of different types of researches and the tremendous energy she deposits to her work, an example to follow in life. Professor Stanly Steinberg for letting me know about UNM and for taking care of my UNM application process. Professor Howard Schreyer for his valuable thesis corrections and for the suggestions he gave me during my research. Professor Yu-Lin Shen for accepting being part of my committee. Professors Evangelos Coutsias and Jens Lorenz for their comments and suggestions after my defense. Professor Lev Steinberg for his teaching and guidance of my masters thesis. The late professor Salvador Llopis and the Professors Adalid Gutiérrez, Jorge Destephen and Concepción Ferrufino for teaching me the basic concepts of mathematics.

Modeling the Mechanical Response of Polycrystalline Thin Films

by

Pedro Joaquín Madrid Ramírez

M.Sc., Mathematics, University of New Mexico, 2011

Ph.D., Mathematics, University of New Mexico, 2013

Abstract

Microelectromechanical systems (MEMS) are part of every modern technological advance. Electrodeposited thin nickel (Ni) polycrystalline films in MEMS often show fiber texture resulting in transverse isotropic elastic properties. It is of interest to determine these elastic properties, in particular the in-plane Young's modulus, since it plays a fundamental role in device performance. The fabrication process of MEMS films introduces uncertainties in the microstructure geometry, crystallographic texture, the crystal elastic constants, the physical film dimensions and other parameters. In this thesis the numerical value of the in-plane Young's modulus of thin Ni polycrystalline films is predicted. The predicted values lie between the Reuss-Voigt averages, a result that is consistent with theory. Additionally the uncertainties of the predictions of the in-plane Young's moduli are quantified by taking into account the uncertainties in microstructure geometry, crystallographic texture, and the numerical values of the Ni single-crystal constants. Representative volumes of the microstructure geometry are modeled with Voronoi diagrams. The crystallographic texture is numerically generated from real X-ray diffraction experimental data by using a texture discretization algorithm. The Young's modulus is estimated by simulating uniaxial stress tests on the numerically generated microstructures with a self-consistent fast Fourier transform (FFT) method. The uncertainties in microstructure geometry, crystallographic texture, and single-crystal elastic constant values are treated as epistemic due to the lack of available experimental data. The sensitivity of the in-plane Young's modulus is examined with respect to the three uncertainties addressed above. The study of the propagation of uncertainties throughout the model lead us to the conclusion that the in-plane Young's modulus of the electrodeposited thin Ni films is extremely sensitive only with respect to the uncertainties in the Ni crystal constants.

A Voronoi based algorithm that attempts to simulate the complete polycrystalline film microstructure geometry is also developed for future large-scale simulations. Finally a J_2 plasticity model that attempts to decribe the overall mechanical response of the Ni film is developed. The J_2 model is based on a phase-field dislocation model developed by Koslowski and it includes the Hall-Petch size effect. The numerical predictions of the J_2 model are compared with real tensile stress experiments performed on as-deposited and annealed Ni samples. The J_2 model predictions show good agreement with phase-field simulations, and capture aspects of size effects.

Contents

List of Figures

List of Tables

Glossary

$\boldsymbol{\sigma}$	Stress tensor.
$\mathbb{C}$	Stiffness tensor or elasticity tensor.
$\mathbb{S}$	Compliance elasticity tensor.
$\boldsymbol{\varepsilon}$	Total Strain tensor.
$\boldsymbol{\varepsilon}^e$	Elastic Strain tensor.
$\boldsymbol{\varepsilon}^p$	Plastic Strain tensor.
$(\boldsymbol{n}_i, \boldsymbol{s}_j)$	Slip system (i, j).
$\mathbb{E}_{\boldsymbol{\sigma}}$	Elastic domain.
$\partial\mathbb{E}_{\boldsymbol{\sigma}}$	Yield surface.
$f_i(\boldsymbol{\sigma}, \boldsymbol{q})$	$i-th$ yield function.
$\boldsymbol{m}_i$	Schmidt tensor.
τ_i	Resolved shear stress.
τ_i^c	Critical resolved shear stress.
b	Length of Burger's vector.

(ϕ_1, Φ, ϕ_2)	Euler angles in Bunge's convention.
$f(\boldsymbol{g})$	Orientation distribution function.
$\langle \mathbb{T}(\boldsymbol{x}) \rangle$	Volume average of the spatially-dependent tensor $\mathbb{T}$.
$\boldsymbol{n}_i \otimes \boldsymbol{s}_i$	Tensor product between vectors $\boldsymbol{n}_i$ and $\boldsymbol{s}_i$.

Chapter 1

Introduction

Microelectromechanical systems are small devices that are a combination of electrical and mechanical elements whose sizes range from the submicrometers to a few millimeters. The range of applications of MEMS devices is wide and it spans the areas of medicine (medical equipment), communications (cell phones, satellites), entertainment (video game consoles) and robotics (microrobots) just to mention a few examples.

All MEMS contain microscopic functional elements and these may be miniaturized structures, microsensors, microactuators and microelectronics. The most notable functional elements are the microsensors and microactuators [41, 10, 39]. Microsensors and microactuators are characterized by converting one form of energy into another. Microactuators use an energy source, electricity for example, and convert it into mechanical motion; microsensors do the opposite.

Nowadays many devices like motors, valves, pressure sensors and switches have been reduced to the microscale, forming part of MEMS technology. It is natural to ask why it is important to make efforts in developing miniaturized technology or MEMS devices. The reasons are the following [41, 10, 39]:

1. **MEMS optimize space usage:** Space optimization in MEMS is an advantage because it makes them portable with lower power consumption and more versatility compared to their macroscopic counterparts. For example, medical doctors can use very small biomedical devices so that they can be injected into the human bloodstream and selectively destroy sick cells or germs, leaving healthy body tissue intact. This would be impossible with the earlier macroscopic counterparts of MEMS. It is speculated that one day MEMS may even be used to manipulate DNA.

2. **MEMS performance exceeds those of their macroscale counterparts:** In spite of the microscopic size of MEMS it is surprising that many of them can cause effects at the macroscale. For example, MEMS researchers have placed small microactuators on the leading edge of airfoils of an aircraft and have been able to steer the aircraft using only these microscopic devices. Besides producing effects at the macroscale, MEMS performance is more efficient than their macroscale counterparts. One example is the microscopic version of pressure sensors. They tend to give more accurate pressure measurements than their earlier macroscopic versions.

3. **MEMS can be manufactured using batch fabrication techniques:** Most of the MEMS devices, especially their mechanical parts, are made of silicon. This has important implications in the MEMS fabrication process because silicon is the most abundant solid material in the Earth's crust and is a high strength solid. As a result MEMS have low fabrication cost and material strength is not a key limiting factor in MEMS performance and reliability. Another reason why MEMS have low cost is because generally they are batch fabricated using a process similar to that used in integrated circuit technology.

We can safely say that MEMS are part of every modern technological advance. Because of the wide range of applications of MEMS devices and their relevance in science, predicting their reliability and durability is considered an important problem in modern technology. All MEMS devices have failure mechanisms that are not well understood. One main reason is that at the microscopic level additional physical phenomena, usually not significant at the macroscopic level, become relevant. For example, van der Waals forces become important when microscopic surfaces are a few micrometers apart. Another interesting phenomenon, known as the Hall-Petch effect, appears in polycrystalline materials. When the grains of a polycrystalline material are nanometer size the yield stress of the polycrystalline material is bigger than the yield stress of coarser grained polycrystalline materials of the same material. Some other phenomena are not completely understood, for example the reverse Hall-Petch effect[1] and elastic strain recovery[2]. These physical phenomena usually can be ignored in the macro-scale but they become important in the micro-scale. Without sufficient attention to these factors, reliability and quality of MEMS devices can be so impaired that they are unusable.

Some common MEMS failure modes are the following [50]:

1. **Sticking:** Sticking can occur when surfaces come into contact. It can even affect elements that are not powered.

2. **Creep:** Creep is defined as the tendency of a solid material to deform slowly and permanently under the influence of stresses. The stresses are usually below the yield strength and this commonly happens in materials exposed to heat. But it has been observed that creep exists in some MEMS devices, even at room temperature.

---

[1] The Hall-Petch effect is associated with an increase in yield stress as grain size is reduced. This process of an increase of yield stress is reversed once the grains have sizes smaller than $20nm$ [60].

[2] This occurs when a load is released from a stress-strain test, some of the total deformation is recovered as elastic deformation [51].

3. **Electrostatic Clamping of Gears:** Evidence has been found to show that clamping of gears due to electrostatic charges present at certain energy levels prevents the gears from moving.
4. **Environmental attack:** MEMS are designed for a variety of applications where environmental effects can be important. This includes valves, sensors, and pumps where the contacting fluids, including water, can be corrosive. Experiments have shown that crack growth is a function of moisture.
5. **Particle Contamination:** Particles can affect the electrical and mechanical devices especially when introduced in small gaps between surfaces. Particles coming from the exterior are now a minor problem because of clean room enviroments. Special attention is given to internally generated particles in MEMS.

The Center for Prediction of Reliability, Integrity and Survivability of Microsystems (PRISM), located at Purdue University, investigates this kind of problem by developing models and software for MEMS simulation. One of the PRISM projects consists of predicting the reliability, integrity and survivability of the microswitch shown in Fig. 1.1. This microswitch is an example of a microactuator.

The top surface shown in Fig. 1.1 shows a cut away of a polycrystalline thin nickel film (or membrane) of length about $400\mu m$, width about $100\mu m$ and thickness between $1\mu m$ and $3\mu m$. The nickel crystals (or grains) forming the membrane are nanometer size. The grain geometry is V-shaped columnar and most of the grains have a preferred orientation producing a special type of texture in the thin film known as fiber texture. The grain geometry and the fiber texture are developed from a manufacturing technique known as electrodeposition.

The membrane is simply supported by two vertical anchors and is surrounded by air at room temperature at one atmosphere of pressure. This device can also

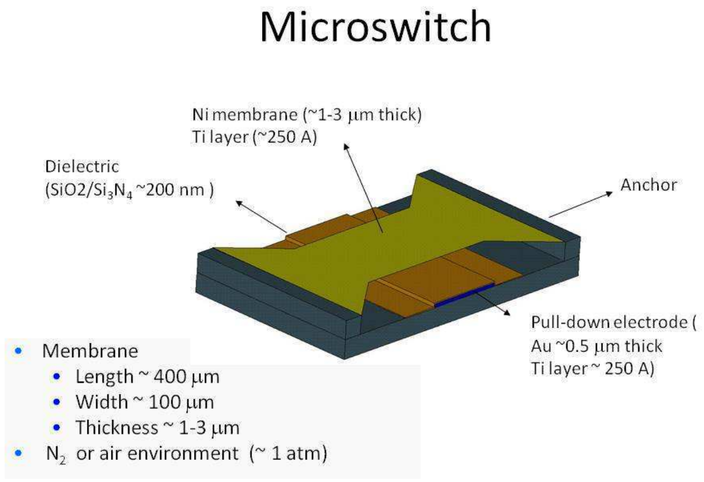

Figure 1.1: Microswitch studied in the PRISM project.

be pressurized by a surrounding gas like nitride (N2). The yellow-blue part below the membrane is an electrode that is connected directly to a voltage source. When the voltage is activated electric fields are generated from the electrode producing body forces in the thin film. As a result, the membrane bends until it contacts the electrode. When the voltage is deactivated, the membrane relaxes to the original configuration shown in Fig. 1.1.

The microswitch is considered to have a high quality lifetime if its performance after several activations and deactivations, typically on the order of billions, is still efficient. One important problem consists in identifying and understanding the failure mechanisms of this MEMS device. In this particular case, it has been observed that the MEMS switches are very sensitive to environmental contaminants and humidity. High humidity levels favor high adhesion forces that may lead to stiction between the membrane and electrode, a failure mechanism of the device. Also nearly-zero humidity is not ideal for the MEMS switches since it significantly increases the friction between the contacting surfaces, leading to premature failure. A second example that leads to stiction in the MEMS switches is related to the stiffness of the MEMS switch. It is known that larger stiffness of the MEMS switch increases the pull-in voltage necessary to activate the switch. Higher pull-in voltages accelerate charging of the electrode's dielectric coating, leading to permanent stiction between the membrane and electrode, and therefore leading to failure.

Like all MEMS, predicting the reliability of the MEMS switch requires expertise from different areas of knowledge. For example, knowledge from solid and fluid dynamics is required for the modeling of air damping in the membrane when it bends. Solid mechanics is required for modeling phenomena like creep, size effects and dynamical loading. Contact physics is used to model the surface chemistry and the interactions between surfaces [48]. Besides having the physical models and the numerical tools to make the simulations, uncertainties may play a significant role in the numerical solutions of mathematical models. For example, the vertical deflection of the membrane is modeled with a partial differential equation that depends on the film thickness, the Poisson's ratio and Young's modulus. These parameters are not known exactly but it is known that they lie in a known interval of finite length. The length of the inverval partially measures the amount of uncertainty of each parameter. Even if some parameters are known experimentally, measurements always carry errors and the exact values of the parameters always lie in an interval. It may happen that the solution of the governing equation is sensitive to one or more of these parameters. If this is the situation then parameter uncertainties must be reduced in order to obtain reliable simulations.

The possible range of the parameters does not describe completely the uncertainties. Also it is important to know their probability distribution (PDF). Knowing the PDF of uncertainties gives a better idea of what parameter values are more likely to occur in the uncertainty interval.

The science that studies the quantitative characterization and reduction of uncertainties in applications is known as uncertainty quantification (UQ). Uncertainties are ussually classified into two basic categories [49]:

1. **Aleatoric uncertainties:** These arise from physical variability present in a system or its enviroment [25], and are irreducible and naturally defined within a probabilistic framework [1]. For example, when measuring the crystal constant values of nickel, these may oscillate around a mean value, which can be described with a probability distribution function. This type of uncertainty can not be reduced because it is inherent to the laboratory equipment under normal operation, but still can be measured.

2. **Epistemic uncertainties:** These are defined as potential deficiencies due to a lack of knowledge [25]. These types of uncertainty are reducible and usually arise from assumptions or simplifications introduced in the derivation of a mathematical model or from physical quantities that cannot be measured experimentally due to technological limitations [1]. Because of their nature, epistemic uncertainties are described by finite length intervals and not by probability distribution functions [57]. For example, the in-plane Young's modulus of the MEMS nickel films can not be measured experimentally due to the presence of residual stresses. Therefore a reasonable estimate of this modulus can be obtained by deriving lower and upper bounds. These bounds can be the Reuss-Voigt averages and they can be improved with the Hashin-Shtrikman bounds. In any case, an interval of finite length describes the possible values of the in-plane Young's modulus.

In any application both kinds of uncertainties are often present. Uncertainty quantification works toward reducing epistemic uncertainties to aleatoric uncertainties. The aleatoric uncertainties are quantified with PDFs by doing hundreds or thousands of realizations. Sampling techniques are useful for the construction of the PDFs, for example the latin hypercube technique or Monte Carlo methods.

In this thesis we focus on the following problems:

1. **Estimate the stiffness of the thin nickel membrane and its sensitivity to experimental uncertainties like crystallographic texture, microstructure geometry, elastic crystal constant values and grain boundaries.**
2. **Model the polycrystalline geometry consistently with experimental data.**
3. **Develop constitutive models that match experimental measurements of the elastic-plastic behavior of the thin film.**

This thesis is organized as follows: Chapter 2 is background material, a brief introduction to crystallography, texture analysis and solid continuum mechanics is provided. In Chapter 3 we define the Reuss-Voigt averages of polycrystalline materials. We also prove analytically that the stiffness of the thin membrane of the MEMS switch is bounded between the Reuss-Voigt averages. Chapter 4 is our main result, whereby we calculate accurately the stiffness of the thin nickel membrane. The stiffness uncertainties are changed from epistemic (Reuss-Voigt averages) to aleatoric (a PDF of the stiffness is generated). Then we study how this stiffness is sensitive to uncertainties in the polycrystalline geometry, uncertainties in experimental texture and uncertainties in values of the elastic crystal constants. We conclude that the stiffness is most sensitive to uncertainties in elastic crystal constants. In Chapter 5 we model the polycrystalline microstructure geometry of the MEMS film with the use of Voronoi diagrams. An algorithm is developed and justified to generate always a desired output. The numerical microstructures are tested with real experimental microstructures. Some features are captured with high accuracy like the grain-size distribution and grain-size dependence on film thickness. Finally in Chapter 6 we develop a J_2 constitutive model in order to predict the elastic-plastic behaviour of the membrane. The numerical simulations are compared with real experimental data [18, 17] and dislocation dynamics simulations [31]. Chapter 7 provides concluding remarks.

Chapter 2

Crystallography and Texture Analysis Background

In this chapter we give a brief introduction to crystallography, texture analysis and solid continuum mechanics. In Section 2.1 we talk about crystallography, in Section 2.2 we discuss some texture analysis concepts and finally Section 2.4 reviews the neccesary material for solid continuum mechanics and elasticity theory.

2.1 Crystallography

Crystallography is the science that studies the arrangement of atoms in a crystal. A crystal is a solid whose molecular structure consists of a three dimensional periodic arrangement of atoms, ions or molecules. Perfect crystals are solid materials with anisotropic and homogeneous properties [4]. These macroscopic properties are induced because of their special molecular structure. The periodic arrangement of atoms can be as simple as $\alpha-$Polonium shown in Fig. 2.1a or apparently complicated like $K_2B_{12}H_{12}$, shown in Fig. 2.1b. Independently of how simple or complicated the

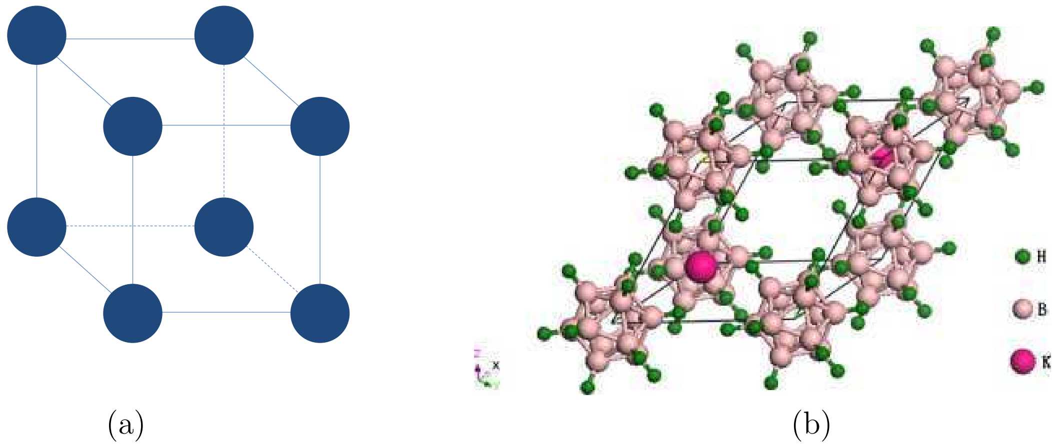

(a) (b)

Figure 2.1: (a) Crystal structure of alpha−polonium. (b) Crystal structure of $K_2B_{12}H_{12}$ [14].

atomic structure of crystals is, all crystals are described in terms of the following two concepts:

- Mathematical lattice.
- Motif.

A mathematical lattice is defined as the set of all integral linear combinations of a given set of linearly independent vectors. The integral linear combinations result in a periodic arrangement of points in space. An integral linear combination of vectors is a linear combination of vectors with coefficients restricted to the set of integers. The dimension of the lattice is defined as the number of linearly independent vectors that generate all points of the lattice. An example of a two dimensional lattice is shown in Fig. 2.2a, the generating vectors are $\boldsymbol{a}$ and $\boldsymbol{b}$. Note that the generating vectors are not unique, Fig. 2.2b shows two additional possible choices.

The motif of a crystal is defined as the physical object that appears repeatedly at each point of the given lattice. In crystallography the object can be as simple

(a)

(b)

Figure 2.2: (a) Two dimensional lattice with generating vertors $\boldsymbol{a}$ and $\boldsymbol{b}$. (b) The two dimensional lattice of Fig. 2.2a with three different pairs of generating vectors.

as an atom or complicated like a molecule. For example, the $\alpha-$Polonium crystal structure has a lattice generated by three orthogonal vectors of the same length, the motif is a single polonium (Po) atom located at each lattice point. The $K_2B_{12}H_{12}$ crystal structure has the three dimensional lattice shown in Fig. 2.7a, the motif is the complicated molecule $K_2B_{12}H_{12}$ located at every lattice point. We can observe that given a fixed lattice, different motifs describe different crystals, but the “skeleton” of the crystal relies on the mathematical concept of lattice. This is the reason why we center our attention on the concept of a mathematical lattice through the rest of this section. This concept facilitates the mathematization of geometric crystal properties.

In crystallography it is convenient to define a coordinate system within a crystal lattice in such a way that the origin coincides with a lattice point. The choice of the lattice point is arbitrary and the coordinate axes usually are defined to be aligned with a set of generating vectors. As a consequence the coordinate system may not be rectangular. Once the coordinate system is defined, every point $\boldsymbol{p}$ of the lattice is represented in the form

$$\boldsymbol{p} = u\boldsymbol{a} + v\boldsymbol{b} + w\boldsymbol{c},$$

where $\boldsymbol{a}$, $\boldsymbol{b}$, $\boldsymbol{c}$ are the generating vectors and u, v, w are integers. In crystallography negative integers are represented with a bar at the top of the number, for example negative four is represented by $\bar{4}$ instead of -4.

The parallelepided whose sides are represented by the vectors $\boldsymbol{a}$, $\boldsymbol{b}$, $\boldsymbol{c}$ is called the unit cell of the lattice. Fig. 2.3a shows a two dimensional unit cell of a two dimensional grid. The set whose elements are the lengths of the generating vectors together with the measure of the angles between the linearly independent vectors are called the lattice parameters or lattice constants of the lattice. Fig. 2.3b shows a unit cell in three dimensions with lattice parameters $\{|\boldsymbol{a}|, |\boldsymbol{b}|, |\boldsymbol{c}|, \alpha, \beta, \gamma\}$. Note that unit cells form a tessellation of the Eucledian space.

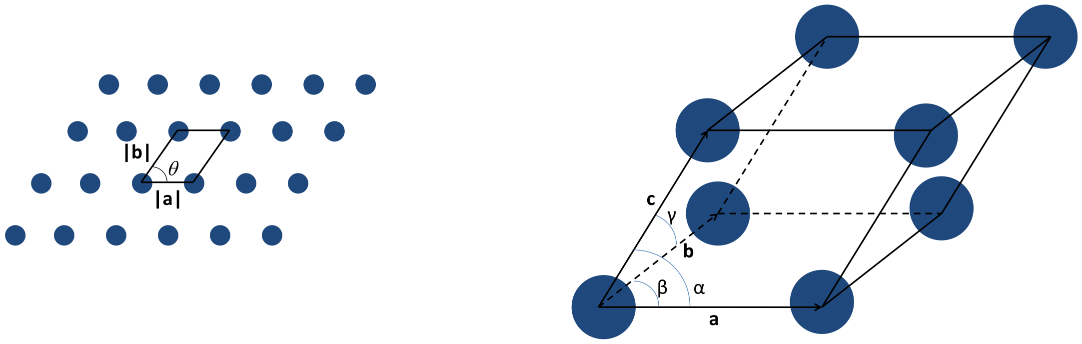

(a) (b)

Figure 2.3: (a) Unit cell with lattice parameters $\{|\boldsymbol{a}|, |\boldsymbol{b}|, \theta\}$. (b) Unit cell with lattice parameters $\{|\boldsymbol{a}|, |\boldsymbol{b}|, |\boldsymbol{c}|, \alpha, \beta, \gamma\}$.

Lattices can be rotated about any of their points or reflected about a line (two dimensional case) or plane (three dimensional case) and may remain unchanged. For example, a two dimensional lattice with lattice parameters $|\boldsymbol{a}| = |\boldsymbol{b}|$ and $\alpha = 90°$ remains unchanged when rotated 90° (clockwise or counterclockwise) about any of its lattice points. The lattice also remains unchanged when reflected with respect to any line that contains $\boldsymbol{a}$ or $\boldsymbol{b}$.

Amazingly there are five rotations such that for any given lattice there is at least one of these five rotations that leaves the lattice unchanged. The rotation angles are 0°, 60°, 90°, 120° and 180°. This is a very important result in crystallography because it classifies lattices from an infinite number to a finite number. We provide a justification of this result for two dimensional lattices [26].

Theorem 1. *For every two dimensional lattice the only rotations about a lattice point that can leave the lattice unaltered are* 0°, 60°*,* 90°*,* 120° *and* 180°*. These rotations are called one–fold, six–fold, four–fold, three–fold and two–fold respectively. In general, an* n*–fold rotation is a rotation angle of magnitude* $\frac{360°}{n}$ *that leaves a lattice unchanged. Here* n *is a natural number.*

Proof. Let us assume we have a general two dimensional lattice that contains an $n-$fold rotation. This means that the lattice remains unchanged after a rotation of $\theta = \frac{360°}{n}$. We want to show that $n = 1, 2, 3, 4$, or 6. Choose the origin of the coordinate system to be located at a lattice point. Define $\boldsymbol{a}$ as the vector that joins two lattice points with the restriction that there are no lattice points between the endpoints of $\boldsymbol{a}$. Now let us rotate $\boldsymbol{a}$ at an angle of θ clockwise and counterclockwise. Let us represent the rotated vectors by $\boldsymbol{b}$ and $\boldsymbol{c}$ respectively, then by definition of $n-$fold rotation we have that the endpoints of $\boldsymbol{b}$ and $\boldsymbol{c}$ are at a point of the lattice, see Fig. 2.4.

If the endpoints of $\boldsymbol{b}$ and $\boldsymbol{c}$ are at lattice points then the sum $\boldsymbol{b}+\boldsymbol{c} = \boldsymbol{d}$ is a vector that also joins lattice points. Note that $\boldsymbol{b}$ and $\boldsymbol{c}$ can be decomposed into the sum of two vectors, one orthogonal to $\boldsymbol{a}$ and the other parallel to $\boldsymbol{a}$. The components along

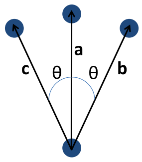

Figure 2.4: Clockwise and counterclockwise rotation of $\boldsymbol{a}$ at an angle θ.

the orthogonal direction of $\boldsymbol{a}$ cancel each other when summed, therefore

$$\boldsymbol{b} + \boldsymbol{c} = 2|\boldsymbol{a}| \cos\theta \hat{\boldsymbol{a}},$$

where $\hat{\boldsymbol{a}}$ is the unit vector along $\boldsymbol{a}$. Because $\boldsymbol{b} + \boldsymbol{c}$ joins two lattice points in the direction of $\boldsymbol{a}$ we have

$$2|\boldsymbol{a}| \cos\theta = m|\boldsymbol{a}|,$$

where m is an integer. This means $\cos\theta = \frac{m}{2}$, but $|\cos\theta| \leq 1$ implies $-1 \leq \frac{m}{2} \leq 1$. The only values of m that satisfy this property are $m = 0, \pm 1, \pm 2$, therefore the values of θ are 0°, 60°, 90°, 120° and 180°. $\square$

The previous theorem leads to the concept of Bravais lattice, a term used in honor of the physicist Auguste Bravais (1811-1863). There are only five types of two dimensional Bravais lattices, these are classified according to rotation symmetry and reflection symmetry properties of the lattice. The two dimensional Bravais lattices are: the oblique lattice, rectangular primitive lattice, rhombic lattice, hexagonal lattice and square lattice. Fig. 2.5 shows these lattices.

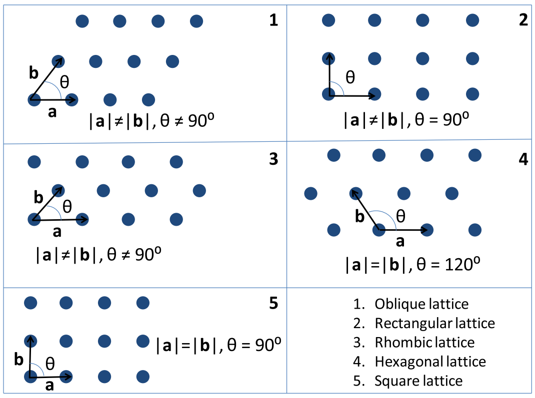

Figure 2.5: The five two dimensional Bravais lattices.

Three dimensional lattices also possess at least one of the five rotation symmetries mentioned above. This time the number of reflection symmetries increases with respect to the two dimensional case because there are more degrees of freedom. As a consequence the classification of Bravais lattices for the three dimensional case is more laborious. Notice that rotations and reflections are not equivalent operations, rotations preserve the coordinate system orientation while reflections invert orientations.

Three dimensional lattices are classified into fourteen Bravais lattices, and these are grouped into a family of seven lattice systems. The lattice systems are described in terms of the three basis vectors. For example, if the basis vectors are not orthogonal and of unequal length then we say the lattice generated by the three basis vectors belongs to the triclinic system. If the basis vectors are orthogonal and of equal length then we say the generated lattice belongs to the cubic system. The list of lattice systems together with their respective Bravais lattices can be found on pg. 90 of [4]. Here we mention only two lattice systems:

- Hexagonal system: This system has one Bravais lattice, the hexagonal closed packed (HCP) Bravais lattice.

- Cubic system: This system has three Bravais lattices, the simple cubic, the body centered cubic (BCC) and the face centered cubic (FCC) Bravais lattice.

The hexagonal and simple cubic lattices are shown in Fig. 2.6a and Fig. 2.6b, the FCC and BCC lattices are shown in Fig. 2.7a and Fig. 2.7b respectively. Nickel is an example of a crystal that has an FCC Bravais lattice where the motif is a single Ni atom.

(a) (b)

Figure 2.6: (a) The HCP Bravais lattice. (b) The simple cubic Bravais lattice.

In many applications it is important to describe mathematically directions, location of atoms (point sites) and planes of atoms within the crystal lattice. For example, in crystal plasticity theory it is known that crystals deform permanently along certain planes and specific directions. Also the orientation of a crystal with respect to a reference coordinate system can be described in terms of planes and directions defined within the crystal lattice. The next sections explain how point sites, directions and planes are described in a crystal lattice.

(a) (b)

Figure 2.7: (a) The FCC Bravais lattice. (b) The BCC Bravais lattice.

Representation of Lattice Points

Consider the unit cell shown in Fig. 2.3b. The basis vectors $\boldsymbol{a}$, $\boldsymbol{b}$, $\boldsymbol{c}$ have different lengths and they do not form an orthogonal system. This type of lattice is known as triclinic Bravais lattice. The vertices of the parallelepiped are lattice points. Without loss of generality assume the origin of the coordinate system is located at the lower left vertex of the frontal face of the parallelepiped. The coordinate axes are aligned with the basis vectors $\boldsymbol{a}$, $\boldsymbol{b}$ and $\boldsymbol{c}$. Let $\boldsymbol{P}$ be a lattice point, then there exists a unique vector $\boldsymbol{p}$ that represents the position of $\boldsymbol{P}$ with respect to the origin such that

$$\boldsymbol{p} = u\boldsymbol{a} + v\boldsymbol{b} + w\boldsymbol{c},$$

where u, v and w are integers. We can express the lattice point $\boldsymbol{P}$ in terms of the coordinates of $\boldsymbol{p}$,

$$\boldsymbol{P} = uvw.$$

In crystallography lattice points are represented as a triple of integers, parenthesis are not used like we do with Cartesian coordinates. The integers are the coordinates of the vector that represents the position of the lattice point with respect to the basis vectors $\boldsymbol{a}$, $\boldsymbol{b}$ and $\boldsymbol{c}$. For example, the lattice point $-\boldsymbol{a}$ is represented as $\bar{1}00$ and the lattice point $\boldsymbol{a}+\boldsymbol{c}$ as 101.

Representation of Crystallographic Directions

Consider a triclinic Bravais lattice with basis vectors $\boldsymbol{a}$, $\boldsymbol{b}$ and $\boldsymbol{c}$. A crystallographic direction is any vector joining two lattice points and is represented by a parallel vector of the same length with the origin as initial point. The notation is a triple of integers in square brackets that denotes the coordinates of the vector translated to the origin. The triple of integers is known as the Miller indices of the crystallographic direction. For example, assume we have a crystallographic direction joining the lattice points $\boldsymbol{P} = u_1v_1w_1$ and $\boldsymbol{Q} = u_2v_2w_2$, then the vector

$$\boldsymbol{p} = (u_2 - u_1)\boldsymbol{a} + (v_2 - v_1)\boldsymbol{b} + (w_2 - w_1)\boldsymbol{c}$$

is parallel to the given crystallographic direction. The vector $\boldsymbol{p}$ is identified with its coordinates $u = u_2 - u_1$, $v = v_2 - v_1$ and $w = w_2 - w_1$, then the crystallographic direction that joins $\boldsymbol{P}$ and $\boldsymbol{Q}$ is represented with the triple

$$[uvw].$$

In crystallography the triple $[uvw]$ does not only describe the crystallographic direction with initial point at the origin and terminal point uvw, it represents all crystallographic directions parallel to the vector $\boldsymbol{p} = u\boldsymbol{a} + v\boldsymbol{b} + w\boldsymbol{c}$. Figure 2.8 is the projection of the triclinic lattice onto the $a - b$ plane, it shows some of the crystallographic directions [210].

Now assume we have a cubic lattice, that is, a triclinic lattice with $|\boldsymbol{a}| = |\boldsymbol{b}| = |\boldsymbol{c}|$ and $\alpha = \gamma = \beta = 90°$. Consider the crystallographic directions [100], $[0\bar{1}0]$ and [001]. Notice that the directions [100] and [001] are not parallel but they are geometrically equivalent in the sense that both are perpendicular to a face of the cubic lattice. From

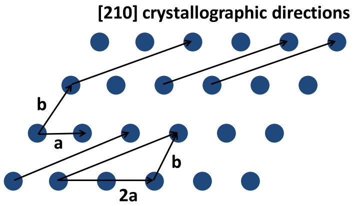

Figure 2.8: Projection of the triclinic lattice onto the $a-b$ plane. The longest vectors are a subset of [210].

a geometrical point of view the faces of the cubic lattice are indistinguishable, all faces look the same. In this particular case we say that [100] and [001] are crystallographic equivalent. Similarly we can verify that $[0\bar{1}0]$ is crystallographic equivalent to [100]. In crystallography a family of equivalent crystallographic directions is represented with angular brackets "<>", since all directions are equivalent, one representative is sufficient to describe the complete family. In our example, the notation

$$< 100 >,$$

represents the crystallographic directions [100], $[\bar{1}00]$, [010], $[0\bar{1}0]$, [001] and $[00\bar{1}]$. All directions are perpendicular to a face of the cubic lattice and are indistinguishable from a geometrical point of view. The family of equivalent directions $< 100 >$ depends of the lattice symmetry. Indeed, if we have the general triclinic Bravais lattice then [100] may not be equivalent to [010], or even to $[\bar{1}00]$.

Representation of Crystallographic Planes

Consider a triclinic Bravais lattice with basis vectors $\boldsymbol{a}$, $\boldsymbol{b}$ and $\boldsymbol{c}$. A crystallographic plane is any plane of a crystallographic lattice passing through at least one lattice point. We know a plane is determined from three noncollinear points. In crystallography planes are not represented in the conventional way of analytic geometry. The representation is better illustrated with examples. Consider a plane P that passes through the points 100, 020 and 001. These lattice points are located at the coordinate axes. The notation used to represent the plane passing through these three points consists first in taking the reciprocals of the multiples of the lattice parameters at which the plane intersects the coordinate axes. In this case the $a-$axis is intersected at one multiple of $|\boldsymbol{a}|$, then the first reciprocal number is one. The $b-$axis is intersected at two times the lattice parameter $|\boldsymbol{b}|$, then the second reciprocal number is $\frac{1}{2}$. The $c-$axis is intercepted at one multiple of $|\boldsymbol{c}|$, then the third reciprocal number is one. Next we write these reciprocals in ordinary parenthesis "()" as follows

$$(1\frac{1}{2}1),$$

finally we multiply all fractions by the least common multiple of the denominators so that all numbers become integers. In this case the least common multiple of the denominators is two, then the crystallographic plane that passes through 100, 020 and 001 is represented as

$$(212),$$

the integers of the triple (212) are called the Miller indices of P. Now consider a plane $P^{'}$ parallel to P that passes through the points 300, 060 and 003. If we follow the steps that define the Miller indices of a plane, we obtain that

$$(212),$$

are the Miller indices of the plane $P^{'}$. In conclusion, the notation (212) represents a family of planes. Indeed, it describes the plane P and all other planes parallel to P. The Miller indices of a family of planes are always relatively prime numbers, this means that they do not have common factors other than the unity.

Let us consider a more subtle example, let $P^{''}$ be a plane that passes through 100 and is parallel to the $bc-$plane. In this case there are no intercepts located at the $b-$axis and $c-$axis. When a plane has no intercepts with a coordinate axis, conventionally we denote the intercept by ∞. Following the convention $\frac{1}{\infty} = 0$, we conclude that the Miller indices of $P^{''}$ are (100).

Now assume we have a cubic lattice, consider the crystallographic planes (100), (010) and (001). Notice that these planes are not parallel but geometrically they are equivalent. This means that because the cubic lattice has $4-$fold rotations about the directions [100], [010] and [001], the planes (100), (010) and (001) are indistinguishable from a geometrical point of view. In crystallography a family of equivalent crystallographic planes is represented with curly brackets "{}". Since all planes are equivalent, one representative is sufficient to describe the complete family. In our example, the notation

$$\{100\},$$

represents the crystallographic planes (100), (010) and (001).

2.2 Orientation of Single Crystals

Many solid materials, like metals and ceramics, are composed of many crystals of varying sizes and orientations. Solid materials of this type are known as polycrystals. For the purpose of estimating mechanical properties of polycrystals, it is important to describe how their crystallites are oriented with respect to the polycrystal.

In order to describe the orientation of a single crystal living in a polycrystalline material, we first define a fixed rectangular coordinate system in the polycrystal. The way the sample coordinate system is chosen is, in principle, arbitrary [6]. Generally, the external shape of the sample will suggest the choice of the coordinate system. For example, in the case of a thin wire, it seems natural to place a coordinate axis along the wire axis, like in Fig. 2.9a. The choice of the second axis is arbitrary and perpendicular to the first axis and the third axis is naturally defined from the first two. Another example is the case of a thin sheet or a thin film, like the one shown in Fig. 2.9b. It is natural to choose a coordinate system whose axes coincide with the sides of the sample. In this work we consider samples with geometry like the one shown in Fig. 2.9b.

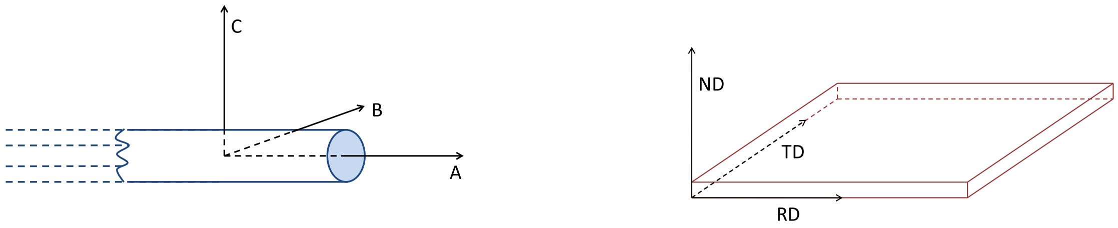

(a) (b)

Figure 2.9: (a) Thin wire, one of the sample's coordinate axes is chosen naturally to coincide with the wire axis. (b) Thin metallic film, the sample coordinate axes are chosen naturally to coincide with the three orthogonal sides of the sample.

Once the sample coordinate system is defined an additional coordinate system within each single crystal must also be defined. The choice of each crystal coordinate system is arbitrary. When the coordinate system in a particular crystallite is settled, the crystallographic coordinates of the coordinate system axes must be the same for all crystallites. It is conventional, from all possible selections of crystal coordinates, to choose a crystal coordinate system that is appropriate for the crystal symmetry [6]. In our case the crystallites of interest have cubic symmetry. For crystals possesing cubic symmetry it is appropriate to choose the coordinate axes to be aligned with the unit cell principal directions. Note that in this case there is still ambiguity in the choice of the coordinate axes. Indeed, there are 24 possible choices of coordinate axes that are aligned with the unit cell principal directions. Despite the ambiguity, any choice of the 24 possible selections gives the same crystal orientation.

Let us denote the sample coordinate system by C_S and the crystal coordinate system by C_C. The orientation of the crystallite within the polycrystalline sample is defined as the linear transformation R that gives the position of the crystal coordinate system with respect to the specimen coordinate system. The linear transformation

$$R : C_S \rightarrow C_C,$$

is by definition a rigid rotation that makes the coordinate system C_S coincide with C_C. Therefore R can be represented by an orthogonal matrix of determinant positive one. There are nine components for the matrix R, but they are not independent. Indeed, the third column of R can be obtained by taking the cross product between the first two columns of R. This reduces the total number of independent components from nine to six. Each column of R is described with a unit vector, setting the norms of the first two columns to one reduces the number of independent components from six to four. But the columns of R are orthogonal, taking the dot product between the first and second column of R and equating it to zero reduces the number of independent components from four to three.

In general, crystallographic orientations are described with three independent variables [52]. There is an intuitive explanation of why we need at most three independent parameters to describe a crystal orientation. Imagine the coordinate systems

C_S and C_C sharing the same origin but their axes not necessarily coincident. If we try to rotate C_S and make it coincide with C_C then the rotation must be done about a unit vector. The unit vector is represented with two independent variables and the rotation about the unit vector is represented with one varible, the angle of rotation. Therefore there is at most a total number of three independent variables for describing the orientation of C_C with respect to C_S.

There are many ways of representing mathematically a crystal orientation, but all representations, in principle, are equivalent and can be converted into one another [6]. Some examples are the Euler angles, quaternions, rotation matrices and the angle/axis representation. Depending on the type of application, each representation has an advantage over the others. In this thesis we shall consider the Euler angle and the rotation matrix representation. The Euler angle representation is based in the following Euler's Rotation Theorem:

Theorem 2. *Any two independent orthonormal coordinate frames can be related by a sequence of rotations (not more than three) about coordinate axes, where no two successive rotations may be about the same axis [32].*

The order in which the successive rotations are applied is not unique, also the choice of rotation axes is arbitrary. In materials science it is common to follow a convention known as the "Bunge Euler Angle Convention" and this is the one we follow in this thesis.

Bunge Euler Angle Convention

The Bunge Euler angle convention refers to three rotations which, when performed in the correct sequence make the coordinate system C_S coincide with C_C. Let the axes of C_S be represented by $\{RD, TD, ND\}$ and the axes of C_C by $\{[100], [010], [001]\}$.

Assume both coordinate systems share the same origin, then the successive rotations that define Bunge's convention are described in the following three steps:

1. Rotate an angle of ϕ_1 about the axis ND, transforming the axis TD into TD' and the axis RD into RD'. The magnitude of ϕ_1 is such that the axis RD' belongs to the plane that contains [100] and [010].
2. Rotate an angle of Φ about the axis RD', transforming the axis TD' into TD'' and the axis RD' into RD''. The magnitude of Φ is chosen so that the axes ND'' and [001] coincide.
3. Rotate an angle of ϕ_2 about the axis ND'' so that both coordinate systems coincide.

The angles ϕ_1, Φ and ϕ_2 are known as Euler angles in Bunge's convention. Analytically, the three successive rotations are expressed as

$$\begin{aligned}
R_{\phi_1} &= \begin{bmatrix} \cos\phi_1 & \sin\phi_1 & 0 \\ -\sin\phi_1 & \cos\phi_1 & 0 \\ 0 & 0 & 1 \end{bmatrix}, \\
R_{\Phi} &= \begin{bmatrix} 1 & 0 & 0 \\ 0 & \cos\Phi & \sin\Phi \\ 0 & -\sin\Phi & \cos\Phi \end{bmatrix}, \\
R_{\phi_2} &= \begin{bmatrix} \cos\phi_2 & \sin\phi_2 & 0 \\ -\sin\phi_2 & \cos\phi_2 & 0 \\ 0 & 0 & 1 \end{bmatrix}.
\end{aligned}$$

The rotation matrix R is related to the Euler angles in the following way:

$$R = R_{\phi_1} R_{\Phi} R_{\phi_2}, \tag{2.1}$$

where the elements of R are given by:

$$\begin{aligned}
R_{11} &= \cos\phi_1\cos\phi_2 - \sin\phi_1\sin\phi_2\cos\Phi, \\
R_{12} &= \sin\phi_1\cos\phi_2 + \cos\phi_1\sin\phi_2\cos\Phi, \\
R_{13} &= \sin\phi_2\sin\Phi, \\
R_{21} &= -\cos\phi_1\sin\phi_2 - \sin\phi_1\cos\phi_2\cos\Phi, \\
R_{22} &= -\sin\phi_1\sin\phi_2 + \cos\phi_1\cos\phi_2\cos\Phi, \\
R_{23} &= \cos\phi_2\sin\Phi, \\
R_{31} &= \sin\phi_1\sin\Phi, \\
R_{32} &= -\cos\phi_1\sin\Phi, \\
R_{33} &= \cos\Phi.
\end{aligned}$$

It follows from the definition of Bunge's convention that the angles ϕ_1, Φ and ϕ_2 are periodic with period 2π. It can be shown that the most general range of Euler angles in Bunge's convention satisfies [52]

$$0^\circ \leq \phi_1,\ \phi_2 \leq 360^\circ,\ 0^\circ \leq \Phi \leq 180^\circ.$$

2.3 The Euler Space

In many applications it is useful to represent the three parameters ϕ_1, Φ and ϕ_2 of a crystal orientation in a three-dimensional coordinate system whose axes are given by the three Euler angles. The set of all possible crystal orientations in this coordinate system is known as the Euler space. Points in the Euler space are denoted by $\boldsymbol{g} = (\phi_1, \Phi, \phi_2)$. Each point of the Euler space corresponds to a crystal orientation and reciprocally, each crystal orientation is represented by a point of the Euler space. It is important to notice that when $\Phi = 0$ the representation of a crystal orientation in the Euler space is not unique. From the definition of Bunge's convention it follows that when $\Phi = 0$ the crystal orientation is determined by the sum $\phi_1 + \phi_2 =$ constant. This means that all points in the line $\Phi = 0$, $\phi_1 + \phi_2 =$ constant represent the same crystal orientation. This phenomenon is known as the gimbal lock. Despite the non-uniqueness of ϕ_1 and ϕ_2 during the gimbal lock phenomenon, the crystal orientation remains clear, as will be seen in Chapter 4.

For the most general case the Euler space corresponds to the rectangular box

$$\Omega_0 = [0\,^\circ, 360\,^\circ] \times [0\,^\circ, 180\,^\circ] \times [0\,^\circ, 360\,^\circ].$$

The volume of this box can be reduced by taking into account the symmetries of the sample and the crystal. The higher the crystal symmetry and the sample symmetry, the smaller is the volume of the Euler space. The reason is because orientations have more equivalent descriptions as the symmetries increase. In our case the crystallites of interest possess cubic symmetry and the sample (thin Ni film) possesses orthorhombic symmetry. For this case it can be shown that the Euler space reduces to [28]

$$\Omega = [0\,^\circ, 90\,^\circ] \times [0\,^\circ, 90\,^\circ] \times [0\,^\circ, 90\,^\circ].$$

Crystallographic Texture

Polycrystalline materials have crystallites of different shapes, sizes and orientations. The effective material properties of these polycrystals depend on the material properties of the single crystals and the way these are oriented. Since crystals are anisotropic, that is, their material properties are directionally dependent, the crystallographic orientations of the crystallites play an important role in the effective material properties of the polycrystal. We define crystallographic texture as the phenomenon of crystallites within a polycrystal having a preferred set of orientations. When all possible orientations of the crystals occur with equal frequency, the effective response of the polycrystal is isotropic [6]. The reason is that the orientation dependence of the polycrystal dissapears when orientations of single crystals are averaged. Polycrystals with effective isotropic behaviour are said to have uniform texture. The branch of materials science that studies the development, the measurements and mathematical representation of crystallographic textures is known as texture analysis.

Textures are induced during material fabrication. For example, the making of metal wires or fibers induces all crystals to have nearly identical orientations along the axial direction, but nearly random radial orientations. Texture in ceramics usually arises because the crystallites in a slurry have shapes that depend on crystalline orientation, often needle- or plate-shaped. These particles align themselves as water leaves the slurry. Another example of texture occurs during the manufacturing process of polycrystalline thin films with thickness in the nanometer and micrometer range. The type of textures produced are known as fiber textures. These textures have the property that one of the crystallographic directions of the crystallites tends to be aligned with a unit vector of the polycrystal. In our case, the thin Ni membrane has a $< 001 >$ fiber texture. This means that for almost all the Ni crystals, one of the cubic crystallographic directions, $< 001 >$, tends to be parallel to the ND direction.

Texture plays an important role in applications because many material properties are highly dependent on the material texture. Some of these material properties are strength, magnetic susceptibility, stress corrosion cracking resistance and resistance to radiation damage. For example, the magnetic susceptibility of transformer cores can be modified by controling the crystallographic texture of the core's silicon steel sheets. As a consequence the magnetic hysteresis may be reduced indirectly and therefore reduce energy losses. During the fabrication process of certain materials some unfavorable crystallographic textures may be developed and these may contribute to a reduction of efficiency in device components. As a consequence the systematic choice of materials and manufacturing process plays an important role in the survivability and performance of engineered materials because of the development of certain kinds of favorable/unfavorable crystallographic textures.

Crystallographic textures have a mathematical representation and it is not obvious. It may seem natural to express all crystal orientations as a function of position, that is, $\boldsymbol{g}(x, y, z)$, where (x, y, z) is a point that belongs to the physical volume of the polycrystal. This vector-valued function is piecewise constant. It is continuous at interior points of the crystallites and discontinuous at the grain boundaries. This function has been experimentally determined for only a very few cases [6], and its mathematical treatment is very complicated and it is not practically applicable. Fortunately an easier mathematical representation of crystallographic textures exists. The main idea is to relate the frequency of occurence of crystal orientations with the volume fractions of orientations within the polycrystal. The spatial position of crystal orientations is ignored in this relationship.

Let V denote the total volume of the polycrystal, and $\Delta\mathrm{V}(\Delta\Omega_E)$ the totality of all volume of the polycrystal which possess the orientations $\boldsymbol{g} \in \Delta\Omega_E$, where $\Delta\Omega_E$ is a subregion of the Euler space Ω_E. It is assumed that there exists an orientation distribution function (ODF) denoted by $f(\boldsymbol{g})$ that satisfies

$$\frac{\Delta\mathrm{V}(\Delta\Omega_E)}{V} = \frac{\int_{\Delta\Omega_E} f(\boldsymbol{g})dg}{\int_{\Omega_E} f(\boldsymbol{g})dg}, \tag{2.2}$$

where dg is the volume differential in the Euler space. In [6] it is shown that the differential volume[1] $dg = \sin\Phi \; d\phi_1 d\Phi d\phi_2$. The left-hand side of (2.2) is called the physical volume fraction of the polycrystal and the right-hand side is known as the orientation volume fraction and both quotients are between zero and one. The right-hand side of (2.2) is interpreted as the probability of finding crystals within the sample with orientations in $\Delta\Omega_E$. An extreme case will be $\Delta\Omega_E = \Omega_E$, when all

---

[1] Intuitively the volume element dg is the product of three infinitesimal quantities: $d\phi_1$ $d\phi_2$ which correspond to the two polar angles ϕ_1 and ϕ_2 and the term $\sin\Phi \; d\Phi$ which corresponds to the contribution of the azimuthal angle Φ of spherical coordinates.

possible crystallographic orientations are taken into account. Intuitively the probability of finding crystals within the sample with orientations in Ω_E is unity because we are taking into account all possible orientations. Note that in this extreme case $\Delta\mathrm{V}(\Omega_E) = V$, consistent with (2.2). This means that the behaviour of f determines which orientations are more likely to happen (texture). For example, if f is sharply peaked in a neighbourhood of an orientation $\boldsymbol{g}$ and almost zero elsewhere, then almost all the crystallites within the polycrystal will have orientations about $\boldsymbol{g}$ and if f is constant then all crystallographic orientations of the Euler space are equally likely.

The ODF satisfies the following properties:

1. $f(\boldsymbol{g}) \geq 0$ for all orientations $\boldsymbol{g} \in \Omega_E$.
2. f is periodic.
3. $\int_{\Omega_E} f(\boldsymbol{g}) dg = \int_{\Omega_E} dg$.

The ODF behaves almost like a PDF, except for the second and third properties. In the case of a PDF the integral of the density function is performed over all space so that the result is unity. In the case of an ODF, the periodicity condition restricts the integration domain to the finite region Ω_E. Also the integral of a PDF is always unity, independently of the choice of parameters, while the integral of the ODF depends on the size of the Euler space, in other words, the crystal and sample symmetries.

Property three is imposed for convenience, if $f(\boldsymbol{g}) = c$, where c is a constant, then $c = 1$. This means that if all crystallites within the polycrystal have the same frequency of ocurrence then $f \equiv 1$, in other words all isotropic polycrystals have the ODF $f(\boldsymbol{g}) = 1$, for all $\boldsymbol{g} \in \Omega_E$. The units of an ODF are called “multiples of random distribution” (m.r.d.) because every ODF f is a multiple of the uniform distribution, that is, $f \equiv 1 \cdot f$.

The ODF of a polycrystal gives knowledge about the sample's crystallographic texture but other important details of the polycrystal are ignored. For example, the grain shapes are not taken into consideration in definition (2.2), only volume fractions. Indeed, given a collection of physical volume fractions, there are infinitely many polycrystals with different grain morphologies having the same set of physical volume fractions. The grain morphologies may be described analytically by associating the grain boundaries with mathematical surfaces in two variables. Constructing the algebraic expressions for the mathematical surfaces is as hard as constructing the spatial dependence of grain orientations $\boldsymbol{g}(x, y, z)$. This description is not practical and therefore an orientation distribution function of grain boundary surfaces is defined in order to facilitate the mathematics [6]. Other types of distribution functions exist and their purpose is to capture features of the polycrystal that other distributions may ignore. In this thesis we work only with the ODF because this is the only distribution we know from experimental measurements.

Crystallographic textures can be determined experimentally with different techniques, most of them are based on the diffraction of radiation by crystal lattices. Some of these methods are the neutron diffraction method, the electron backscatter diffraction (EBSD) method and the X-ray diffraction (XRD) method. Each method has its advantages and disadvantages. The features, advantages and disadvantages of the XRD method are summarized as follows [52]:

- **Features**
  - X-rays have a large penetration depth, typically $5\mu m$.
  - XRD has a spatial resolution that ranges from $25\mu m$ up to $1mm$.
- **Advantages**
  - XRD is a well established technique.

  - Relatively large areas are scanned in one scan, typically $10mm^2$.
  - A large number of grains, usually 10^4 grains, can be analyzed in one experiment.

- **Disadvantages**
  - The ODF is not obtained directly from XRD measurements, instead pole figures are generated. The ODF can be estimated from pole figure information but in some cases the calculations may be complicated leading to erroneous information about the crystallographic texture of the sample. Pole figures are discussed in the next section.
  - XRD measurements have poor spatial resolution, they are not appropriate for microscopic samples.

The features, advantages and disadvantages of the EBSD method are summarized as follows [52]:

- **Features**
  - EBSD measurements are surface sensitive because electrons have a small penetration depth, typically $20nm$.
  - EBSD has a spatial resolution of approximately $10nm$.
- **Advantages**
  - The direct calculation of the ODF is possible.
  - Other microstructural parameters may be measured, for example grain size.
  - Crystallographic texture of two phase materials can be measured easily.
- **Disadvantages**

  - It is expensive to use.
  - It is not adequate for some types of samples, for example polymers.
  - It is less practical for texture measurements of large grain-size materials.
  - It may give erroneous texture measurements if highly deformed grains are present.

In the majority of the cases XRD methods are used to measure crystallographic texture. Because of the advantages and disadvantages of the EBSD and XRD methods, in practice both techniques may be used to complement each other.

The neutron diffraction method is not as common as the XRD technique. The main reason is that the neutron diffraction method requires specialised facilities like a nuclear reactor. This method is used when there are clear advantages over the XRD method, some of these situations are [52]:

- Samples with irregular or large grains. The texture characterization of these polycrystals requires a larger penetration depth. Neutron diffraction methods also work well in porous materials.
- Samples with low crystal symmetry or multi-phase systems.
- When the speed of measurement becomes important, for example in situations of texture evolution.

The crystallographic texture of the thin Ni film shown in Fig. 1.1 was measured with XRD methods. A brief explanation of how crystallographic texture is obtained from the XRD method is provided in Appendix A. It was mentioned above that one disadvantage of the XRD method is that the ODF is not directly estimated, instead a plot of diffraction intensity peaks is obtained as a function of the reflection angle θ of crystallographic planes. The process of constructing the ODF from the diffraction intensity peaks is explained in the next section.

From XRD Measurements to the ODF

We know from Appendix A that XRD measurements lead to diffraction intensity peak plots. The crystallographic planes (hkl) that reflect high intensities at an angle θ can be calculated from Bragg's law and therefore the orientation of the crystallite with respect to the sample can be known. Assume we are interested in counting intensity peaks that correspond to reflections of (hkl) crystallographic planes of different crystals. The intensity peaks of the (hkl) planes may correspond to different reflection angles and therefore to different crystals. The (hkl) planes are identified with their unit normals and therefore these normals also represent the crystals orientations. The collection of unit normals within the sample represent geometrically the crystallographic texture of the material, in this case by showing the crystal orientations in terms of the plane unit normals. The problem with this representation is that it is three dimensional, the information lives in a unit sphere and it is difficult to interpret for thousands of crystals. Fortunately there exists a two dimensional representation of crystallographic texture known as a pole figure.

A pole figure of a polycrystal associated to the (hkl) crystallographic planes is defined as the collection of the stereographic projections of the unitary normals of the (hkl) planes onto the sample. A schematic representation of a pole figure is shown in Fig. 2.10. The circle that contains the RD and TD axes is the equator of the unit sphere. The center of the unit sphere coincides with the origin of the sample and the north and south poles of the sphere are located at the positive and negative ND axis respectively. The black dots located at the equator are the stereographic projections of the unit normals. The stereograhic projection of each normal may be done from the north pole or the south pole of the unit sphere. The pole is chosen so that the stereograhic projection falls inside the sphere on the equatorial plane.

In general, one pole figure is not sufficient to describe the polycrystal texture;

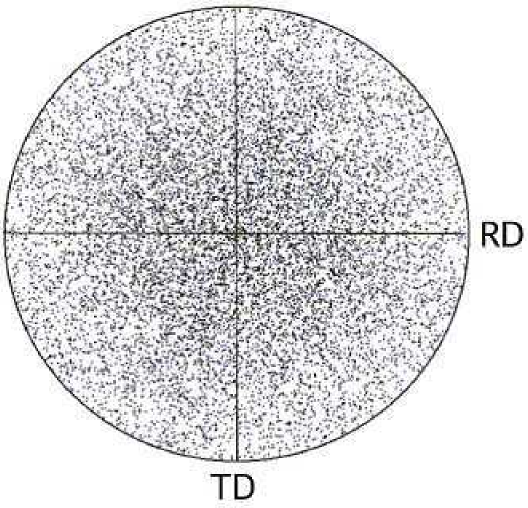

Figure 2.10: Schematic representation of a pole figure.

usually at least two pole figures are required but three are preferable even when the crystals have high symmetries [52]. In practice the pole figures are obtained from specialised software. Some examples of this software are the preferred orientation package - Los Alamos (popLA) and the Materials Analysis Using Diffraction (MAUD) software.

Once the pole figures are generated, these are used to approximate the ODF. This can be done with MTEX, a Matlab toolbox for quantitative texture analysis. The ODFs are generally described by the m.r.d. given on a grid defined in the Euler space with angles taken in steps of 5°. The case when the ODF is known only at a set of discrete values is called a discrete orientation distribution function. The term ODF is reserved for the continuos mathematical expression of $f(\phi_1, \Phi, \phi_1)$.

Table 2.1 shows a few entries of the discrete ODF of one of the MEMS switches.

ϕ_1	Φ	ϕ_2	$f(\phi_1, \Phi, \phi_2)$
0°	0°	0°	9.12178 m.r.d.
0°	0°	10°	9.11875 m.r.d.
0°	0°	15°	9.11197 m.r.d.
0°	0°	20°	9.10393 m.r.d.
0°	0°	25°	9.09851 m.r.d.
0°	0°	30°	9.10278 m.r.d.
0°	0°	35°	9.14714 m.r.d.
$\vdots$	$\vdots$	$\vdots$	$\vdots$
355°	90°	85°	7.88253 m.r.d.

Table 2.1: Discrete ODF of one of the MEMS switches.

The Euler angles range as follows:

$$\begin{aligned} \phi_1^j &= j5^\circ, \quad i = 0, 1, \ldots, 71, \\ \Phi^k &= k5^\circ, \quad k = 0, 1, \ldots, 18, \\ \phi_2^l &= l5^\circ, \quad l = 0, 1, \ldots, 17. \end{aligned} \tag{2.3}$$

At the end of Section 2.3 it was mentioned that the Euler space of a polycrystal with orthorhombic symmetry and cubic crystal symmetry is $\Omega_E = [0, \frac{\pi}{2}] \times [0, \frac{\pi}{2}] \times [0, \frac{\pi}{2}]$. Note that some of the discrete Euler angles (2.3) are outside the Euler space Ω_E. This is not a problem in texture calculations because any information outside Ω_E is redundant, f is a periodic function.

It is important to notice that any $< hkl >$ pole figure can be recovered from the discrete ODF. This is done by constructing a cumulative distribution function defined on a path through the set of discrete Euler angles. By a path we mean an ordering of the discrete Euler angles. Specifically, assume the angles (2.3) are ordered in an arbitrary way, this means that the grid points $(\phi_1^j, \Phi^k, \phi_2^l)$ may be placed along a line. Let us represent the ordering of these grid points by $\{\boldsymbol{g}_i\}_{i=1}^{24624}$

then a cumulative distribution function is defined as follows:

$$F_N = \sum_{i}^{N} \frac{\int_{B_{jkl}} f(\phi_1^j, \Phi^k, \phi_2^l) dg}{\int_B dg}, \quad 1 \leq N \leq 24624,$$

where B_{jkl} is a box centered around the grid point $(\phi_1^j, \Phi^k, \phi_2^l)$, the indices j, k, l correspond to the well ordered index i and $B = [0°, 360°] \times [0°, 90°] \times [0°, 90°]$. Note that each integer i is identified uniquely with an orientation $(\phi_1^j, \Phi^k, \phi_2^l)$. If N_{max} uniformly distributed random numbers $\{x_n\}_{n=1}^{N_{max}} \subset (0, 1)$ are generated, then there exist integers I such that $F_I \leq x_n < F_{I+1}$. We identify each x_n with the index I and therefore with the orientation $(\phi_1^j, \Phi^k, \phi_2^l)$ corresponding to the index I.

In this way crystal orientations $(\phi_1^j, \Phi^k, \phi_2^l)$ are generated with radom numbers x_n. Therefore the $< hkl >$ crystal directions with orientations $(\phi_1^j, \Phi^k, \phi_2^l)$ can be projected with the stereographic projection. When a large number of orientations is sampled, the $< hkl >$ pole figure is obtained. Typically the sampling number is in the thousands.

MTEX is a powerful quantitative texture analysis tool. Besides generating discrete ODFs from pole figures it can also generate pole figures from the discrete ODF. Figure 2.11 shows the $< 001 >$, $< 110 >$ and $< 111 >$ pole figures of the experimental discrete ODF of Table 2.1. The $< 001 >$ pole figure shows that the $< 001 >$ crystallographic directions are almost aligned with the ND direction of the sample. The blue rings observed in the $< 110 >$ and $< 111 >$ pole figures indicate that the in-plane orientations are uniformly distributed. These pole figures indicate that the polycrystal has fiber texture, where the isotropy plane is located in the RD-TD plane. MTEX can also compute other quantities that arise in texture analysis like mean orientations, reconstructed ODFs and misfits. These concepts are mentioned in Section 4.4 of Chapter 4.

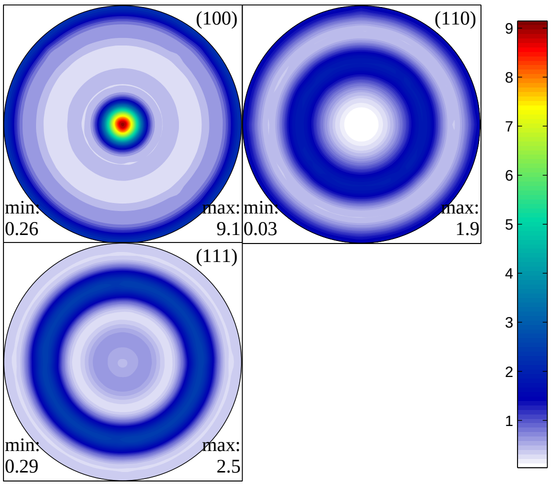

Figure 2.11: Experimental pole figures $< 001 >$, $< 110 >$ and $< 111 >$ of one MEMS device. The pole figures were generated from the discrete ODF using the MTEX software. The colorbar is a measure of the m.r.d. .

2.4 Governing Equations of Motion of Solid Deformable Bodies

Every solid body under the action of applied external forces exhibits deformation to some extent. By deformation we mean changes in volume, shape or motion. The deformation of the body is described mathematically in the following way. Let $B \subset \mathbb{R}^3$ be a body[2], $\varphi : B \times [0,T] \to \mathbb{R}^3$ a motion[3] of B. The scalar $T > 0$ represents the maximum time of interest. Assuming a coordinate system is defined, points in B are represented by capital letters $\boldsymbol{X}$ and are called material points while points in $\mathbb{R}^3$ are represented by lower case letters $\boldsymbol{x}$ and are called spatial points. For a particular time $t \in [0,T]$ we have the relationship [42]

$$\boldsymbol{x} = \varphi(\boldsymbol{X}, t),$$

---

[2] B is an open bounded set of $\mathbb{R}^3$ with piecewise smooth boundary.

[3] φ is a motion if it is smooth, orientation preserving and injective map.

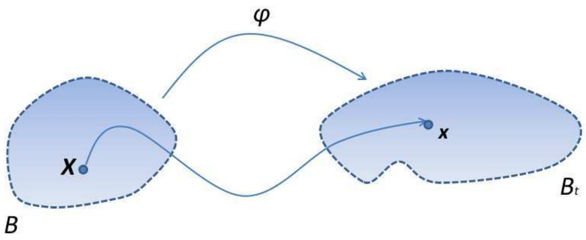

Figure 2.12: Motion of the body B in the time interval $[0,t]$. Material point $\boldsymbol{X}$ follows the indicated trajectory from $\boldsymbol{X}$ at time $t=0$ to $\boldsymbol{x}$ at time t.

which means that the material point $\boldsymbol{X}$ is at position $\boldsymbol{x}$ at time t. For $\boldsymbol{X}$ fixed and $t \in [0,T]$, the vector-valued function $\boldsymbol{\phi}_{\boldsymbol{X}}(t) = \varphi(\boldsymbol{X},t)$ describes the trajectory of material point $\boldsymbol{X}$ in the time interval $[0,T]$. This is illustrated in Fig. 2.12.

By definition, at time $t=0$ we have $B \equiv \varphi(B,0)$; this is called the initial configuration of the body B. For a particular time $t \in (0,T]$, the set $B_t \equiv \varphi(B,t)$ is called the current configuration of B. Let $\mathbf{b}(\mathbf{x},t)$ be a body force[4] per unit mass acting on B_t at $\boldsymbol{x}$ and time t and $\rho(\mathbf{x},t)$ be the mass density of B_t at point $\boldsymbol{x}$ and time t. The local forms of conservation of linear and angular momentum are summarized in the following initial boundary value problem (IBVP) [56]:

$$\begin{aligned} \rho\frac{d^2\mathbf{u}}{dt^2} &= div\ \boldsymbol{\sigma} + \rho\mathbf{b}, \\ \boldsymbol{\sigma} &= \boldsymbol{\sigma}^T, \end{aligned}$$

---

[4] Here $\mathbf{b}$ is a vector field acting on $B_t \times (0,T)$.

where the initial and boundary conditions are

$$\begin{aligned} \mathbf{u}(\mathbf{X},0) &= \mathbf{u_0}(\mathbf{X}), \qquad \frac{\partial \mathbf{u}}{\partial t}(\mathbf{X},0) = \mathbf{v_0}(\mathbf{X}), \\ \mathbf{u}|_{\partial_{\mathbf{u}}B} &= \bar{\mathbf{u}}, \qquad\qquad \boldsymbol{\sigma}\cdot\hat{\mathbf{n}}|_{\partial_{\boldsymbol{\sigma}}B} = \bar{\mathbf{t}}, \end{aligned}$$

in the above, $\mathbf{u} : \bar{B}_t \times [0,T] \to \mathbb{R}^3$ is the displacement field, $\hat{\mathbf{n}}$ is the unit normal vector to $\partial_{\boldsymbol{\sigma}}B$, $\boldsymbol{\sigma}(\mathbf{x},t)$ is the second order Cauchy stress tensor at $\boldsymbol{x}$ and time t, $\mathbf{u_0}$, $\mathbf{v_0}$ are prescribed displacements and velocities in B and $\bar{\mathbf{u}}$, $\bar{\mathbf{t}}$ are prescribed displacements and tractions on $\partial_{\mathbf{u}}B$ and $\partial_{\boldsymbol{\sigma}}B$ respectively. The sets $\partial_{\mathbf{u}}B$ and $\partial_{\boldsymbol{\sigma}}B$ are portions of the boundary ∂B that satisfy $\partial_{\mathbf{u}}B \cap \partial_{\boldsymbol{\sigma}}B = \phi$ and $\overline{\partial B} = \overline{\partial_{\mathbf{u}}B \cup \partial_{\boldsymbol{\sigma}}B}$. The displacement field at time t and position $\boldsymbol{x}$ is defined as $\boldsymbol{u} \equiv \boldsymbol{x} - \boldsymbol{X}$, where $\boldsymbol{X}$ is such that $\varphi(\boldsymbol{X},t) = \boldsymbol{x}$. Geometrically the displacement field $\boldsymbol{u}$ describes the position of points of the current configuration relative to their associated material points of the initial configuration. Therefore if $\boldsymbol{u}$ is known, then the deformation of the body is entirely determined [56].

The equations of conservation of linear and angular momentum can be solved assuming the stress $\boldsymbol{\sigma}$ is known. Generally this is not the case, a complementary set of equations for $\boldsymbol{\sigma}$ is required. Intuitively the motion of a body depends on material properties, indeed, a set of external forces applied to a solid rigid body will produce different motion than the same set of forces applied to a ”malleable” solid body.

The conservation laws contain no information about the material, therefore the required set of complementary equations must contain information of this type. This set of complementary equations are called constitutive equations. It has been observed from experiments that not all solid materials deform displaying the same set of features. For example, some materials, like rubber, may suffer big deformations under the action of external forces and recover their original shape when these forces are removed. Other solid materials, for example most metals, recover their original shape only for small deformations. Other materials, like glass, may suddenly break or fail after the application of forces greater than a given magnitude without showing deformation (or very small deformation) for forces smaller than the given magnitude. These types of materials are known as brittle materials. The list of features is numerous and new features are showing up with the development of new engineered materials. For example, polycrystalline nanomaterials may exhibit a Hall-Petch effect, a phenomenon that has been observed only in nanomaterials and not in bulk materials. The Hall-Petch effect is explained in Chapter 6.

The above observations on material deformation indicate that there is no single constitutive model that describes the deformation of all solid materials. It is practically impossible for a mathematical model to capture all experimental features. Developing constitutive models for solid materials is an art, and this can be done from physical principles or from purely mathematical relations which try to fit experimental data. The first class of constitutive models are known as mechanistic models and the second class are known as phenomenological models. The constitutive models we develop and study in this thesis are phenomenological. We start with the phenomenological linear model known as Hooke's law.

2.5 Hooke's Linear Constitutive Model

In the previous section it was mentioned that the deformation of the body B is completely determined if the displacement vector field $\boldsymbol{u}$ is known. The displacement can be used directly to describe the deformation of a solid body, but sometimes it may be of interest to know if the relative displacements between material points of the *current configuration* have changed. These relative displacements may not be evident to detect directly from $\boldsymbol{u}$. For example, motions like translations and rigid rotations of B have the property that the relative displacements between material points of the current configuration remain constant[5], but the displacement vector field $\boldsymbol{u}$ may be a complicated non-constant mathematical function of $\boldsymbol{x}$ and t.

The tensor field that describes changes of the relative displacements between material points in the current configuration is called the strain tensor. There is no universal definition of strain tensor, but when deformations are "small" it turns out that all definitions of the strain tensor are equivalent. In this thesis we adopt the following widely used definition :

$$\boldsymbol{\varepsilon} = \mathrm{sym}\left(\nabla \boldsymbol{u}\right), \tag{2.4}$$

where $\boldsymbol{\varepsilon}$ is the strain tensor, $\mathrm{sym}\left(\nabla \boldsymbol{u}\right) = \frac{1}{2}\left(\nabla \boldsymbol{u} + \left(\nabla \boldsymbol{u}\right)^T\right)$ is the symmetric part of the second order tensor $\nabla \boldsymbol{u}$ and ∇ is the gradient operator with respect to the spatial variable $\boldsymbol{x}$.

Most metals, in particular Ni, exhibit a stress-strain relationship like the one shown in Fig. 2.13. Naturally this plot is between one component of $\boldsymbol{\sigma}$ and one component of $\boldsymbol{\varepsilon}$. The following terminology is common in describing stress-strain relations:

1. There exists an initial approximate linear relationship between stress and strain; we call this the linear elastic range. By elastic we mean that when the stress is reduced to zero, the strain is also reduced to zero along the same line. In other words, when the external forces are removed, the body recovers its original shape. The stress in this region ranges from zero to a maximum value σ_0, called the proportional limit.

2. Generally there is a nonlinear region, still elastic, where stress takes values between σ_0 and $\sigma_y \geq \sigma_0$. The stress σ_y is known as the yield stress or elastic limit of the material. The yield stress σ_y is defined as the maximum stress at

---

[5] Neglecting relativistic effects.

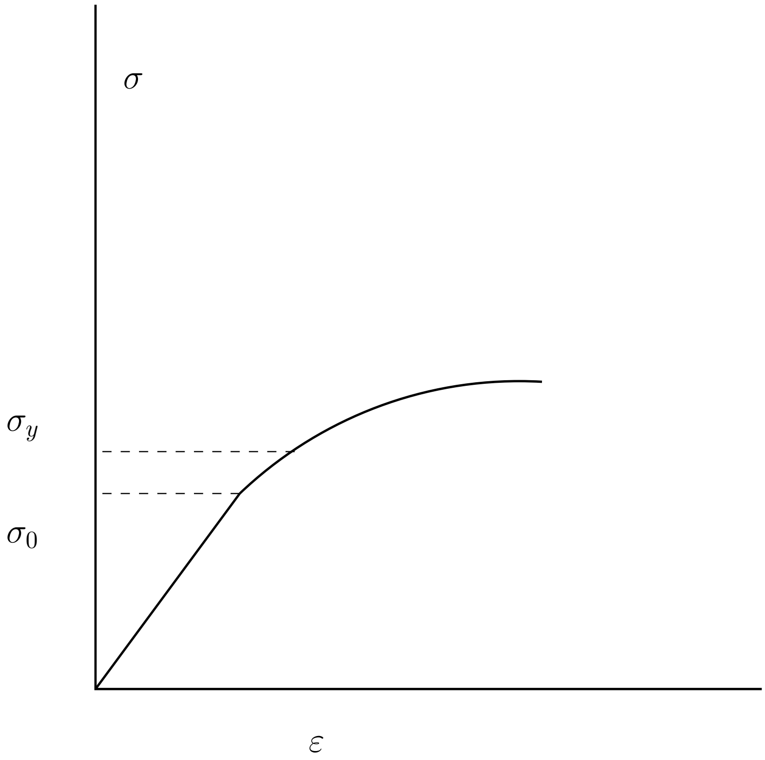

Figure 2.13: Relationship between stress and strain.

which a solid remains elastic. Experimentally it has been observed that many solids satisfy $\sigma_0 \approx \sigma_y$, but there exist cases where a significant difference is appreciated [27].

3. There exists a plastic behaviour, this is achieved when the stresses are higher than σ_y. Plastic behaviour is defined as a permanent deformation in a solid body; that is, after unloading to zero stress, a permanent non-zero strain remains in the solid. The plastic behaviour of polycrystals is studied in Chapter 6.

The linear elastic range is described mathematically with Hooke's law:

$$\boldsymbol{\sigma} = \mathbb{C} : \boldsymbol{\varepsilon}, \tag{2.5}$$

where $\mathbb{C}$ is the fourth order elastic stiffness tensor. The colon represents the standard double dot product between the stiffness and elasticity tensors. If a rectangular coordinate sytem is defined, then (2.5) takes the form

$$\sigma_{ij} = C_{ijkl}\varepsilon_{kl}, \tag{2.6}$$

where the scalars σ_{ij}, C_{ijkl} and ε_{kl} are the components of $\boldsymbol{\sigma}$, $\mathbb{C}$ and $\boldsymbol{\varepsilon}$ respectively. All subindices take values in the set $\{1, 2, 3\}$ and repeated indices follow Einstein's summation convention [42]. The relations $\boldsymbol{\sigma}^T = \boldsymbol{\sigma}$ and $\boldsymbol{\varepsilon}^T = \boldsymbol{\varepsilon}$ applied to (2.6) imply

$$C_{ijkl} = C_{jikl} = C_{jilk} = C_{ijlk},$$

these are known as minor symmetries of $\mathbb{C}$. Assuming the total elastic energy of the body is conserved [58] then $\mathbb{C}$ satisfies the additional symmetry

$$C_{ijkl} = C_{klij},$$

known as major symmetry. Hooke's law (2.5) can also be represented in the form

$$\boldsymbol{\varepsilon} = \mathbb{S} : \boldsymbol{\sigma}, \tag{2.7}$$

where $\mathbb{S} = \mathbb{C}^{-1}$ is the fourth order compliance tensor or flexibility tensor. The tensor $\mathbb{S}$ also satisfies minor and major symmetries. Note that $\mathbb{C}$ or $\mathbb{S}$ have a total number of eighty-one components, but only twenty-one are independent, this follows from their minor and major symmetries.

Voigt introduced a convenient notation where the components of the symmetric second order stress and strain tensors are put into a vector of length six, and the components of the fourth order compliance and stiffness tensors are put in a six-by-six matrix. In Voigt's notation, Hooke's law (2.6) is

$$\begin{bmatrix} \sigma_{11} \\ \sigma_{22} \\ \sigma_{33} \\ \sigma_{23} \\ \sigma_{13} \\ \sigma_{12} \end{bmatrix} = \begin{bmatrix} C_{1111} & C_{1122} & C_{1133} & C_{1123} & C_{1113} & C_{1112} \\ C_{2211} & C_{2222} & C_{2233} & C_{2223} & C_{2213} & C_{2212} \\ C_{3311} & C_{3322} & C_{3333} & C_{3323} & C_{3313} & C_{3312} \\ C_{2311} & C_{2322} & C_{2333} & C_{2323} & C_{2313} & C_{2312} \\ C_{1311} & C_{1322} & C_{1333} & C_{1323} & C_{1313} & C_{1312} \\ C_{1211} & C_{1222} & C_{1233} & C_{1223} & C_{1213} & C_{1212} \end{bmatrix} \begin{bmatrix} \epsilon_{11} \\ \epsilon_{22} \\ \epsilon_{33} \\ 2\epsilon_{23} \\ 2\epsilon_{13} \\ 2\epsilon_{12} \end{bmatrix}. \tag{2.8}$$

where the numerical values of the components of (2.8) depend on the choice of the coordinate sytem.

Some materials exhibit certain types of symmetries in the sense that when the coordinate system is rotated at a certain angle about an axis, the components of the stiffness matrix (2.8) remain unchanged. These types of symmetries are known as material symmetries. For the purpose of determining the matrix structure of the stiffness matrix (2.8) under material symmetries, it is useful to know how fourth order tensor components change under coordinate system transformations. Let D_{ijkl} denote the components of the fourth order tensor $\mathbb{D}$ with respect to a rectangular coordinate system $C1$. Assume the coordinate system $C1$ is rotated with respect to its origin to the coordinate system $C2$. Then there exists an orthogonal linear transformation $R : C1 \to C2$ with positive determinant such that

$$D^{'}_{ijkl} = R_{ti}R_{rj}R_{mk}R_{nl}D_{trmn}, \tag{2.9}$$

where $D^{'}_{ijkl}$ are the components of $\mathbb{D}$ with respect to the coordinate system $C2$. The relation (2.9) is known as fourth order tensor transformation.

Physically the material symmetries of most metals depend on how their crystallites are oriented. For example, if all crystallites are oriented identically, forming a single crystal, then the material symmetries are deduced from the crystal lattice symmetries. If the crystal orientations are not identical, e.g. they are described with an ODF, then the material symmetries of the stiffness matrix are deduced from averaging over the crystallographic texture which results in an effective elasticity matrix. This averaging process is explained in detail in Chapter 3.

Assuming that an effective elasticity matrix corresponds to a polycrystal, then its material symmetries lead to simplified forms of (2.8). For example, if the crystallites are randomly oriented (uniform texture), then the stiffness matrix in (2.8) is invariant under rotations. Using the fourth order tensor transformation (2.9) it can be shown that the stiffness matrix (2.8) reduces to the form

$$\boldsymbol{C} = \begin{bmatrix} \lambda+2\mu & \lambda & \lambda & 0 & 0 & 0 \\ \lambda & \lambda+2\mu & \lambda & 0 & 0 & 0 \\ \lambda & \lambda & \lambda+2\mu & 0 & 0 & 0 \\ 0 & 0 & 0 & \mu & 0 & 0 \\ 0 & 0 & 0 & 0 & \mu & 0 \\ 0 & 0 & 0 & 0 & 0 & \mu \end{bmatrix} \tag{2.10}$$

where λ and μ are independent constants known as Lamé constants. Materials exhibiting this type of symmetry are known as isotropic. Sometimes it is convenient to express (2.10) in terms of an alternative pair of constants which depend on the Lamé constants. The constants we use in this thesis are the bulk modulus K, the shear modulus G, the Young's modulus E and Poisson's ratio ν. These constants satisfy $\lambda = K - \frac{2}{3}G$, $\mu = G$, $E = \frac{9KG}{3K+G}$ and $\nu = \frac{3K-2G}{2(3K+G)}$. The stiffnes matrix for isotropic materials (2.10) in terms of the bulk and shear modulus takes the form

$$\boldsymbol{C} = \begin{bmatrix} K+\frac{4G}{3} & K-\frac{2G}{3} & K-\frac{2G}{3} & 0 & 0 & 0 \\ K-\frac{2G}{3} & K+\frac{4G}{3} & K-\frac{2G}{3} & 0 & 0 & 0 \\ K-\frac{2G}{3} & K-\frac{2G}{3} & K+\frac{4G}{3} & 0 & 0 & 0 \\ 0 & 0 & 0 & G & 0 & 0 \\ 0 & 0 & 0 & 0 & G & 0 \\ 0 & 0 & 0 & 0 & 0 & G \end{bmatrix}, \tag{2.11}$$

this form of $\boldsymbol{C}$ will be used in Chapter 3.

There are many other types of material symmetries that lead to simplified forms of the stiffness matrix provided the coordinate system is chosen appropriately. The material symmetries relevant in this work, besides isotropy, are cubic symmetry and plane isotropy.

A solid material is defined to have cubic symmetry if there exists a rectangular coordinate system such that its stiffness matrix takes the form

$$\boldsymbol{C} = \begin{bmatrix} C_{11} & C_{12} & C_{12} & 0 & 0 & 0 \\ C_{12} & C_{11} & C_{12} & 0 & 0 & 0 \\ C_{12} & C_{12} & C_{11} & 0 & 0 & 0 \\ 0 & 0 & 0 & C_{44} & 0 & 0 \\ 0 & 0 & 0 & 0 & C_{44} & 0 \\ 0 & 0 & 0 & 0 & 0 & C_{44} \end{bmatrix}, \tag{2.12}$$

where C_{11}, C_{12} and C_{44} are constants. The stiffness matrix (2.12) has the property that when the coordinate system is rotated in multiples of $\frac{\pi}{4}$ about any of its coordinate axes then its entries remain unchanged. The geometrical meaning of this is that materials with cubic symmetry possess nine planes of symmetry whose normals are on the three coordinate axes and on the coordinate planes making an angle of $\frac{\pi}{4}$ with the coordinate axes [59]. Single crystals falling in the cubic system category have this geometrical property when the axes of the coordinate system are aligned with the unit cell vectors. In particular, Ni which has an FCC lattice, has a stiffness matrix of the form (2.12) provided the coordinate system axes are aligned with the unit cell vectors.

Now assume a solid material has the property that the components of its stiffness matrix do not change when its reference coordinate system is rotated about a fixed line that contains one of its coordinate axis. The plane perpendicular to this line is called plane of symmetry. Without loss of generality assume this line contains the third axis of the coordinate system. Then from the fourth order tensor transformation (2.9) it follows that the stiffness matrix takes the form

$$\boldsymbol{C} = \begin{bmatrix} C_{11} & C_{12} & C_{13} & 0 & 0 & 0 \\ C_{12} & C_{11} & C_{13} & 0 & 0 & 0 \\ C_{13} & C_{13} & C_{33} & 0 & 0 & 0 \\ 0 & 0 & 0 & C_{44} & 0 & 0 \\ 0 & 0 & 0 & 0 & C_{44} & 0 \\ 0 & 0 & 0 & 0 & 0 & \frac{1}{2}\left(C_{11} - C_{12}\right) \end{bmatrix}, \qquad (2.13)$$

where C_{11}, C_{12}, C_{13}, C_{33} and C_{44} are constants. This type of material symmetry is known as plane isotropy or transverse isotropy. Materials with transverse isotropy symmetry have the same elastic loading paths when the components of stress and strain are restricted to the plane of symmetry. The slope common to all loading paths which are restricted to the plane of symmetry is known as the in-plane Young's modulus of the material and it is calculated as the reciprocal of the $1-1$ or $2-2$ component of the compliance matrix $\boldsymbol{S} = \boldsymbol{C}^{-1}$. The in-plane Young's modulus in terms of the fourth order compliance tensor is the reciprocal of the $1-1-1-1$ or $2-2-2-2$ component of $\mathbb{S}$, this follows from the equivalence between the tensor notation and Voigt's matrix notation.

An example of a solid exhibiting transverse isotropy is the polycrystalline thin Ni film of the MEMS device shown in Fig. 1.1. These devices are transverse isotropic because the electrodeposition process induces a crystallographic fiber texture in them. It is important to note that if $\boldsymbol{C}$ has the form (2.10), (2.12) or (2.13) then $\boldsymbol{S} = \boldsymbol{C}^{-1}$ also has the same matrix structure as $\boldsymbol{C}$.

Chapter 3

Bounding Effective Material Properties

The interest in determining the effective elastic behavior of polycrystalline materials started approximately in the end of the 1920's with the investigations of Voigt [61] and Reuss [53]. Voigt estimated the effective polycrystalline stiffness tensor $\mathbb{C}$ by assuming all crystals deform with the same strain $\boldsymbol{\varepsilon}$ throughout the polycrystal. Reuss estimated the effective polycrystalline compliance tensor $\mathbb{S}$ by assuming uniform stress $\boldsymbol{\sigma}$ throughout the polycrystal. Both assumptions are unrealistic. Voigt's assumption leads to a situation where the forces between grains can not be in equilibrium while Reuss's assumption leads to a configuration of deformed grains that can not fit together, that is, the strains are not compatible.

In 1952 Hill [20] demonstrated that some of the effective elastic moduli of isotropic polycrystalline aggregates are bounded below and above by the Reuss and Voigt averages respectively. The moduli that are bounded in [20] are the shear modulus G, the bulk modulus K and Young's modulus E. Bounds on polycrystalline aggregates with anisotropy were not developed in [20].

In 1962 Hashin and Shtrikman [15] developed variational principles which lead to tighter isotropic aggregate bounds compared to the Voigt and Reuss bounds. In [16] Hashin and Shtrikman applied their results to isotropic aggregates made of cubic crystals. Their theoretical estimates were tested on real materials like copper (Cu), gold (Au) and $\alpha-$iron ($\alpha-$Fe) [1]. The bounds were also compared with the already known Reuss-Voigt bounds. The numerical results of [16] were reported in a table similar to Table 3.1, where G is the shear modulus, G_R, G_V are the Reuss and Voigt effective shear moduli and G_1, G_2 are the Hashin-Shtrikman lower and upper bounds of the shear modulus G, respectively. The improvement of the Hashin-Shtrikman bounds over the Reuss-Voigt bounds is clear from Table 3.1.

Metal	C_{11}	C_{12}	C_{44}	G_R	G_V	G_1	G_2	G
Cu	171	122	69.1	40	54	44.8	47.2	45.5
Au	186	157	42	24	31	27	29	27.7
$\alpha-$Fe	237	141	116	74	89	80	83	83.1

Table 3.1: Hashin-Shtrikman bounds compared to the Reuss-Voigt bounds for Cu, Au and α-Fe. All material constants are in GPa.

Bounding effective material properties can be useful, specially when no geometrical or statistical information is known about the grain orientations. Knowing theoretical bounds on effective material properties can also help verify numerical simulations. One example of verification is shown in the next chapter for polycrystalline thin nickel films.

An interesting example of the importance of knowing bounds on effective material properties is shown in [62]. It is mentioned that the separation between the Voigt and Reuss bounds on the bulk and shear moduli of olivines can be as large as 4%. The Hashin-Shtrikman bounds developed in [62] reduced the separation to about 0.5%. For many practical purposes these numerical bounds can be considered as

---

[1] Copper and gold are FCC crystals and $\alpha-$iron is a BCC crystal.

exact.

The purpose of this chapter is to provide an analytical proof that the in-plane Young's modulus of polycrystalline materials with transverse isotropy is bounded between the Reuss-Voigt averages. The bounds do not follow directly from [20] because the polycrystalline microstructure of the MEMS device is not isotropic. The bounds were developed by combining results from [20] and [8, 46]. This chapter is organized as follows: First we discuss the Reuss-Voigt averages [53, 61] then Hill's result [20] on bounding effective material properties. Finally we provide the analytical proof that the in-plane Young's modulus of the polycrystalline microstructure is bounded between the Reuss-Voigt averages.

Crystal Averages

Let $\Omega \subset \mathbb{R}^3$ be the physical domain of a polycrystalline material, $\mathbb{T}(\boldsymbol{x})$ a tensorial quantity that depends on the position $\boldsymbol{x} \in \Omega$. The volume average of this tensorial quantity is defined as

$$\langle \mathbb{T}(\boldsymbol{x}) \rangle = \frac{1}{V} \int_{\Omega} \mathbb{T}(\boldsymbol{x}) dV,$$

where V is the volume of Ω and dV is the volume differential. In this chapter occasionally we use the notation $\mathbb{T}$ to represent the average $\langle \mathbb{T}(\boldsymbol{x}) \rangle$. The position $\boldsymbol{x} \in \Omega$ belongs to a single crystal and therefore it is identified with the corresponding crystal orientation $\boldsymbol{g}$. Based on the relation [6]

$$\frac{dV}{V} = f(\boldsymbol{g}) d\boldsymbol{g},$$

the average $\mathbb{T}$ can also be expressed in terms of the ODF $f(\boldsymbol{g})$ as follows:

$$\mathbb{T} = \int_{\Omega_0} \mathbb{T}(\boldsymbol{g}) f(\boldsymbol{g}) d\boldsymbol{g},$$

where Ω_0 is the Euler space. It is important to know that in general

$$\left\langle \mathbb{T}^{-1}(\boldsymbol{x}) \right\rangle \neq \left\langle \mathbb{T}(\boldsymbol{x}) \right\rangle^{-1}.$$

The problem of calculating effective elastic properties is formulated as follows: Assume the elastic stiffness $\mathbb{C}^c(\boldsymbol{x})$ of the individual crystals forming Ω are known. Also assume the texture of the polycrystal given by $f(\boldsymbol{g})$ is known. The macroscopic response of Ω is assumed to obey Hooke's law

$$\boldsymbol{\sigma} = \mathbb{C} : \boldsymbol{\varepsilon},$$

where $\boldsymbol{\sigma} = \langle \boldsymbol{\sigma}(\boldsymbol{x}) \rangle$, $\boldsymbol{\varepsilon} = \langle \boldsymbol{\varepsilon}(\boldsymbol{x}) \rangle$ and $\mathbb{C}$ is the effective elasticity tensor. **The goal is to determine $\mathbb{C}$ as a function of $\mathbb{C}^c$ and the material texture**. We now present Voigt and Reuss estimates of $\mathbb{C}$.

Reuss-Voigt Averages

Assume forces are applied to a linear elastic material Ω, then for all $\boldsymbol{x} \in \Omega$ we have:

$$\boldsymbol{\sigma}(\boldsymbol{x}) = \mathbb{C}^c(\boldsymbol{x}) : \boldsymbol{\varepsilon}(\boldsymbol{x}). \tag{3.1}$$

If we average both sides of the above equation we get

$$\langle \boldsymbol{\sigma}(\boldsymbol{x}) \rangle = \langle \mathbb{C}^c(\boldsymbol{x}) : \boldsymbol{\varepsilon}(\boldsymbol{x}) \rangle. \tag{3.2}$$

Voigt assumed all crystals deform with uniform strain $\boldsymbol{\varepsilon} = \langle \boldsymbol{\varepsilon}(\boldsymbol{x}) \rangle$. Under this assumption equation (3.2) takes the form

$$\boldsymbol{\sigma} = \langle \mathbb{C}^c(\boldsymbol{x}) \rangle : \boldsymbol{\varepsilon},$$

the quantity $\mathbb{C}^V = \langle \mathbb{C}^c(\boldsymbol{x}) \rangle$ is known as Voigt's average and it is an approximation to the macroscopic elasticity tensor $\mathbb{C}$. Voigt's average associated to the compliance tensor is defined as $\mathbb{S}^V = \left(\mathbb{C}^V\right)^{-1}$.

Instead of averaging (3.1), Reuss averaged

$$\boldsymbol{\varepsilon}(\boldsymbol{x}) = \mathbb{S}^c(\boldsymbol{x}) : \boldsymbol{\sigma}(\boldsymbol{x}),$$

where $\mathbb{S}^c(\boldsymbol{x}) = (\mathbb{C}^c)^{-1}(\boldsymbol{x})$. Instead of assuming all crystals deform identically, Reuss assumed all crystals had uniform stress $\boldsymbol{\sigma} = \langle \boldsymbol{\sigma}(\boldsymbol{x}) \rangle$, then under this assumption the average of the above expression takes the form

$$\boldsymbol{\varepsilon} = \langle \mathbb{S}^c(\boldsymbol{x}) \rangle : \boldsymbol{\sigma}.$$

The quantity $\mathbb{S}^R = \langle \mathbb{S}^c(\boldsymbol{x}) \rangle$ is known as Reuss's average and $\mathbb{C}^R := \left(\mathbb{S}^R\right)^{-1}$ is an approximation to the macroscopic elasticity tensor $\mathbb{C}$. In general $\mathbb{C}^R \neq \mathbb{C}^V$.

Hill's 1952 Result

In this section we summarize Hill's result [20]. It is known from Bishop and Hill [3] that if the polycrystalline aggregate Ω contains a sufficiently large number of grains and if it is macroscopically homogeneous then

$$\boldsymbol{\sigma} : \boldsymbol{\varepsilon} = \int_\Omega \boldsymbol{\sigma}(\boldsymbol{x}) : \boldsymbol{\varepsilon}(\boldsymbol{x})\, dV. \tag{3.3}$$

Let $\boldsymbol{\sigma}^*(\boldsymbol{x})$ denote the stress that would exist in a crystal having strain $\boldsymbol{\varepsilon}$. Similarly, denote by $\boldsymbol{\varepsilon}^*(\boldsymbol{x})$ the strain that would be produced in such a crystal by a stress $\boldsymbol{\sigma}$, in other words

$$\begin{aligned} \boldsymbol{\sigma}^*(\boldsymbol{x}) &= \mathbb{C}^c(\boldsymbol{x}) : \boldsymbol{\varepsilon}, && (3.4) \\ \boldsymbol{\varepsilon}^*(\boldsymbol{x}) &= \mathbb{S}^c(\boldsymbol{x}) : \boldsymbol{\sigma}. && (3.5) \end{aligned}$$

Consider the expression

$$\boldsymbol{\sigma}(\boldsymbol{x}) : \boldsymbol{\varepsilon}^*(\boldsymbol{x}).$$

If we use $\boldsymbol{\sigma}(\boldsymbol{x}) = \mathbb{C}^c(\boldsymbol{x}) : \boldsymbol{\varepsilon}(\boldsymbol{x})$ and (3.5) in the above equation we obtain

$$\begin{aligned} \boldsymbol{\sigma}(\boldsymbol{x}) : \boldsymbol{\varepsilon}^*(\boldsymbol{x}) &= (\mathbb{C}^c(\boldsymbol{x}) : \boldsymbol{\varepsilon}(\boldsymbol{x})) : (\mathbb{S}^c(\boldsymbol{x}) : \boldsymbol{\sigma}) \\ &= \boldsymbol{\sigma} : \boldsymbol{\varepsilon}(\boldsymbol{x}). \end{aligned}$$

Similarly, if we substitute $\boldsymbol{\varepsilon}(\boldsymbol{x}) = \mathbb{S}^c(\boldsymbol{x}) : \boldsymbol{\sigma}(\boldsymbol{x})$ and (3.4) in $\boldsymbol{\sigma}^*(\boldsymbol{x}) : \boldsymbol{\varepsilon}(\boldsymbol{x})$ we obtain

$$\begin{aligned} \boldsymbol{\sigma}^*(\boldsymbol{x}) : \boldsymbol{\varepsilon}(\boldsymbol{x}) &= (\mathbb{C}^c(\boldsymbol{x}) : \boldsymbol{\varepsilon}) : (\mathbb{S}^c(\boldsymbol{x}) : \boldsymbol{\sigma}(\boldsymbol{x})) \\ &= \boldsymbol{\sigma}(\boldsymbol{x}) : \boldsymbol{\varepsilon}. \end{aligned}$$

It is convenient to represent $\boldsymbol{\sigma}(\boldsymbol{x}) : \boldsymbol{\varepsilon}^*$ and $\boldsymbol{\sigma}^*(\boldsymbol{x}) : \boldsymbol{\varepsilon}(\boldsymbol{x})$ in the following equivalent forms:

$$\begin{aligned} \boldsymbol{\sigma}(\boldsymbol{x}) : \boldsymbol{\varepsilon}(\boldsymbol{x}) + (\boldsymbol{\sigma}(\boldsymbol{x}) - \boldsymbol{\sigma}^*(\boldsymbol{x})) : (\boldsymbol{\varepsilon}(\boldsymbol{x}) - \boldsymbol{\varepsilon}) &= \boldsymbol{\sigma}^*(\boldsymbol{x}) : \boldsymbol{\varepsilon} + 2(\boldsymbol{\varepsilon}(\boldsymbol{x}) - \boldsymbol{\varepsilon}) : \boldsymbol{\sigma}(\boldsymbol{x}), \\ \boldsymbol{\sigma}(\boldsymbol{x}) : \boldsymbol{\varepsilon}(\boldsymbol{x}) + (\boldsymbol{\sigma}(\boldsymbol{x}) - \boldsymbol{\sigma}) : (\boldsymbol{\varepsilon}(\boldsymbol{x}) - \boldsymbol{\varepsilon}^*(\boldsymbol{x})) &= \boldsymbol{\sigma} : \boldsymbol{\varepsilon}^*(\boldsymbol{x}) + 2(\boldsymbol{\sigma}(\boldsymbol{x}) - \boldsymbol{\sigma}) : \boldsymbol{\varepsilon}(\boldsymbol{x}). \end{aligned}$$

We claim that the second terms of the left-hand side of the previous two equations are nonnegative, indeed, we know that $\mathbb{C}^c(\boldsymbol{x})$ is positive definite for all $\boldsymbol{x} \in \Omega$, then

$$\begin{aligned} (\boldsymbol{\sigma}(\boldsymbol{x}) - \boldsymbol{\sigma}^*(\boldsymbol{x})) : (\boldsymbol{\varepsilon}(\boldsymbol{x}) - \boldsymbol{\varepsilon}) &= [(\mathbb{C}^c(\boldsymbol{x}) : \boldsymbol{\varepsilon}(\boldsymbol{x})) - (\mathbb{C}^c(\boldsymbol{x}) : \boldsymbol{\varepsilon})] : (\boldsymbol{\varepsilon}(\boldsymbol{x}) - \boldsymbol{\varepsilon}) \\ &= (\boldsymbol{\varepsilon}(\boldsymbol{x}) - \boldsymbol{\varepsilon}) : \mathbb{C}^c(\boldsymbol{x}) : (\boldsymbol{\varepsilon}(\boldsymbol{x}) - \boldsymbol{\varepsilon}) \\ &\geq 0, \end{aligned}$$

where the relation $\boldsymbol{\sigma}(\boldsymbol{x}) = \mathbb{C}^c(\boldsymbol{x}) : \boldsymbol{\varepsilon}(\boldsymbol{x})$ and (3.4) were used. Similarly we can show

$$(\boldsymbol{\sigma}(\boldsymbol{x}) - \boldsymbol{\sigma}) : (\boldsymbol{\varepsilon}(\boldsymbol{x}) - \boldsymbol{\varepsilon}^*(\boldsymbol{x})) \geq 0,$$

by using (3.5), $\boldsymbol{\varepsilon}(\boldsymbol{x}) = \mathbb{S}^c(\boldsymbol{x}) : \boldsymbol{\sigma}(\boldsymbol{x})$ and the positive definiteness of $\mathbb{S}^c(\boldsymbol{x})$. Therefore the previous two inequalities imply

$$\begin{aligned} \boldsymbol{\sigma}(\boldsymbol{x}) : \boldsymbol{\varepsilon}(\boldsymbol{x}) &\leq \boldsymbol{\sigma}^*(\boldsymbol{x}) : \boldsymbol{\varepsilon} + 2(\boldsymbol{\varepsilon}(\boldsymbol{x}) - \boldsymbol{\varepsilon}) : \boldsymbol{\sigma}(\boldsymbol{x}), \\ \boldsymbol{\sigma}(\boldsymbol{x}) : \boldsymbol{\varepsilon}(\boldsymbol{x}) &\leq \boldsymbol{\sigma} : \boldsymbol{\varepsilon}^*(\boldsymbol{x}) + 2(\boldsymbol{\sigma}(\boldsymbol{x}) - \boldsymbol{\sigma}) : \boldsymbol{\varepsilon}(\boldsymbol{x}). \end{aligned}$$

If we take volume averages of both sides of these two inequalities and use (3.3) we obtain

$$\begin{aligned} \boldsymbol{\sigma} : \boldsymbol{\varepsilon} &\leq \boldsymbol{\varepsilon} : \langle \boldsymbol{\sigma}^*(\boldsymbol{x}) \rangle, \\ \boldsymbol{\sigma} : \boldsymbol{\varepsilon} &\leq \boldsymbol{\sigma} : \langle \boldsymbol{\varepsilon}^*(\boldsymbol{x}) \rangle. \end{aligned}$$

But since $\boldsymbol{\sigma}^*(\boldsymbol{x}) = \mathbb{C}^c(\boldsymbol{x}) : \boldsymbol{\varepsilon}$ and $\boldsymbol{\varepsilon}^*(\boldsymbol{x}) = \mathbb{S}^c(\boldsymbol{x}) : \boldsymbol{\sigma}$, then the two previous inequalities take the form

$$\begin{aligned} \boldsymbol{\sigma} : \boldsymbol{\varepsilon} &\leq \boldsymbol{\varepsilon} : \langle \mathbb{C}^c(\boldsymbol{x}) \rangle : \boldsymbol{\varepsilon}, \\ \boldsymbol{\sigma} : \boldsymbol{\varepsilon} &\leq \boldsymbol{\sigma} : \langle \mathbb{S}^c(\boldsymbol{x}) \rangle : \boldsymbol{\sigma}. \end{aligned}$$

If we apply $\boldsymbol{\sigma} = \mathbb{C} : \boldsymbol{\varepsilon}$ and $\boldsymbol{\varepsilon} = \mathbb{S} : \boldsymbol{\sigma}$ to the left-hand side of the first and second inequalities above, respectively, and note $\mathbb{C}^V = \langle \mathbb{C}^c(\boldsymbol{x}) \rangle$ and $\mathbb{S}^R = \langle \mathbb{S}^c(\boldsymbol{x}) \rangle$ we obtain

$$\boldsymbol{\varepsilon} : \mathbb{C} : \boldsymbol{\varepsilon} \leq \boldsymbol{\varepsilon} : \mathbb{C}^V : \boldsymbol{\varepsilon}, \tag{3.6}$$

$$\boldsymbol{\sigma} : \mathbb{S} : \boldsymbol{\sigma} \leq \boldsymbol{\sigma} : \mathbb{S}^R : \boldsymbol{\sigma}, \tag{3.7}$$

for all $\boldsymbol{\sigma}$ and $\boldsymbol{\varepsilon}$. It is important to notice that inequalities (3.6) and (3.7) hold for any kind of crystal symmetry and sample symmetry. In [20] Hill proved that the bulk modulus, shear modulus and Young's modulus are bounded between the Reuss and Voigt averages when Ω is macroscopically isotropic. The proof of the bounds is essentially an application of the following theorem [13] to inequalities (3.6) and (3.7):

Theorem 3. *Let* $\boldsymbol{A}$ *and* $\boldsymbol{B}$ *be two symmetric* $n \times n$ *matrices that satisfy the inequality* $\boldsymbol{x}^T \boldsymbol{A} \boldsymbol{x} \leq \boldsymbol{x}^T \boldsymbol{B} \boldsymbol{x}$ *for all* n *dimensional vectors* $\boldsymbol{x}$. *If* $\{\lambda_1, \ldots, \lambda_n\}$ *and* $\{\beta_1, \ldots, \beta_n\}$ *are the eigenvalues of* $\boldsymbol{A}$ *and* $\boldsymbol{B}$ *written in increasing order, respectively, then* $\lambda_i \leq \beta_i$ *for* $i = 1, \ldots, n$.

Let us prove first that Voigt's average is an upper bound of the three elastic constants mentioned previously. It was already shown by Voigt and Reuss that if Ω has macroscopic isotropic properties then $\mathbb{C}^V$ and $\mathbb{S}^R$ must also be isotropic [61, 53]. The isotropy of $\mathbb{C}^V$ and $\mathbb{S}^R$ holds independently of the degree of anisotropy of the individual single crystals. Voigt and Reuss gave explicit expressions for the bulk modulus and shear modulus of $\mathbb{C}^V$ and $\mathbb{S}^R$ in terms of the elastic constants of the single crystals of Ω.

Because $\mathbb{C}$, $\mathbb{S}$, $\mathbb{C}^V$ and $\mathbb{S}^R$ are isotropic, two independent constants determine completely each fourth order tensor. Let G and K denote the shear and bulk modulus associated with $\mathbb{C}$ and $\mathbb{S}$. Similarly, let G_R, K_R denote the shear and bulk modulus associated with $\mathbb{C}^R$ and $\mathbb{S}^R$ and G_V, K_V the shear and bulk modulus associated with $\mathbb{C}^V$ and $\mathbb{S}^V$.

Now we assume (3.6) and (3.7) are expressed in Voigt's matrix notation, then the matrix $\boldsymbol{A}$ in Theorem 3 plays the role of Voigt's representation of $\mathbb{C}$ or $\mathbb{S}$ in (3.6) and (3.7). Similarly, matrix $\boldsymbol{B}$ in Theorem 3 plays the role of Voigt's representation of $\mathbb{C}^V$ or $\mathbb{S}^R$ in (3.6) and (3.7). The vector $\boldsymbol{x}$ plays the role of $\boldsymbol{\varepsilon}$ or $\boldsymbol{\sigma}$ because the second order tensors $\boldsymbol{\varepsilon}$ and $\boldsymbol{\sigma}$ are vectors in Voigt's notation.

Let $\boldsymbol{C}$ and $\boldsymbol{C}^V$ denote Voigt's representation of $\mathbb{C}$ and $\mathbb{C}^V$ respectively. Because Ω is isotropic then $\boldsymbol{C}$ takes the form (2.11) with respect to any orthonormal basis $\{\boldsymbol{e}_1, \boldsymbol{e}_2, \boldsymbol{e}_3\}$. The eigenvalues of $\boldsymbol{C}$ are G and $3K$. Similarly, the eigenvalues of $\boldsymbol{C}^V$ are G_V and $3K_V$. Then from the theorem it is clear that $G \leq G_V$ and $K \leq K_V$. The Young's modulus E of $\mathbb{C}$ can be expressed in terms of K and G as follows

$$\frac{1}{E} = \frac{1}{3G} + \frac{1}{9K}.$$

The inequalities $G \leq G_V$ and $K \leq K_V$ imply $\frac{1}{E} \geq \frac{1}{3G_V} + \frac{1}{9K_V}$. But by definition $\frac{1}{E_V} = \frac{1}{3G_V} + \frac{1}{9K_V}$, therefore $E \leq E_V$. Similarly, applying the above theorem to inequality (3.7) we can prove $G \geq G_R$, $K \geq K_R$ and $E \geq E_R$.

Apparently when Ω is orthotropic, like the MEMS films, it is harder to prove with the same methods employed above, that the in-plane Young's modulus of Ω lies between the Reuss-Voigt averages. The reason is that the number of independent constants of $\boldsymbol{C}$ increases to five and the eigenvalues of $\boldsymbol{C}$ are algebraically more complicated expressions that depend on these constants. The eigenvalues can be computed from (2.13). Directly from inequalities between the eigenvalues of $\boldsymbol{C}$, $\boldsymbol{C}^V$, $\boldsymbol{S}$ and $\boldsymbol{S}^R$ it is not easy to show $E_R \leq E \leq E_V$; we decided to follow a different path.

Based on experimental observations we assume $\mathbb{C}$ has plane isotropy. We do not know anything about $\mathbb{C}^V$ and $\mathbb{S}^R$. The symmetry of $\mathbb{C}^V$ and $\mathbb{S}^R$ depends on the crystallographic texture of Ω. We also do not know anything about the analytic form of the ODF $f(\boldsymbol{g})$. We know from XRD experiments that Ω has $< 001 >$ fiber texture.

In [8] it is mentioned that if the [001] crystallographic axis of almost all single crystals in Ω is aligned with an imaginary axis $\boldsymbol{v}$, then for any orthogonal coordinate system $\{\boldsymbol{e}_1, \boldsymbol{e}_2, \boldsymbol{e}_3\}$, with $\boldsymbol{e}_3$ and $\boldsymbol{v}$ aligned, the ODF f can be approximated with a function that depends only on the Euler angle Φ. We will show that this information is sufficient to prove that $\mathbb{C}^V$ and $\mathbb{S}^R$ share the same symmetry as $\mathbb{C}$.

By definition of Voigt's average we have

$$C^V_{ijkl} = \frac{1}{8\pi^2} \int_0^{2\pi} \int_0^{\pi} \int_0^{2\pi} C^s_{ijkl}(\phi_1, \Phi, \phi_2)\ f(\Phi)\ \sin\Phi\ d\phi_1\ d\Phi\ d\phi_2, \tag{3.8}$$

where $C^s_{ijkl}(\phi_1, \Phi, \phi_2) = R_{ti} R_{rj} R_{mk} R_{nl} C^c_{trmn}$ is the $ijkl-$component of the crystal stiffness with respect to the sample coordinate system, C^c_{trmn} is the $trmn-$component of crystal stiffness with respect to the crystal corrdinate system and R_{ij} is the $ij-$component of the rotation matrix (2.1). Note that R_{ij} depends on the Euler angles and C^c_{trmn} is constant. Simplifying (3.8) requires laborious symbolic calculations. For this process we decided to use Matlab's symbolic toolbox. The simplified result can be expressed as follows

$$\boldsymbol{C}^V = \begin{bmatrix} C^V_{1111} & C^V_{1122} & C^V_{1133} & 0 & 0 & 0 \\ C^V_{1122} & C^V_{1111} & C^V_{1133} & 0 & 0 & 0 \\ C^V_{1133} & C^V_{1133} & C^V_{3333} & 0 & 0 & 0 \\ 0 & 0 & 0 & C^V_{2323} & 0 & 0 \\ 0 & 0 & 0 & 0 & C^V_{2323} & 0 \\ 0 & 0 & 0 & 0 & 0 & \left(C^V_{1111} - C^V_{1122}\right)/2 \end{bmatrix}$$

where C^V_{1111}, C^V_{1122}, C^V_{1133}, C^V_{3333} and C^V_{2323} are complicated expressions that depend on the crystal constants C^c_{trmn} and on

$$\int_0^{\pi} f(\Phi)\ \sin^q \Phi\ d\Phi,$$

where $q = 1, 3, 5$. Fortunately the explicit form of the above constants is not relevant for our main purpose of proving $E_R \leq E \leq E_V$.

Note that $\boldsymbol{C}^V$ has the same matrix structure as $\boldsymbol{C}$, in other words we proved $\boldsymbol{C}^V$ preserves the transverse isotropic structure of $\boldsymbol{C}$ provided the ODF f depends only on Φ. Because $\boldsymbol{C}$ and $\boldsymbol{S}$ share the same kind of symmetries it follows that $\boldsymbol{S}^R$ has the same matrix structure as $\boldsymbol{C}^V$.

Now if we use Voigt's notation in (3.6) we have

$$\boldsymbol{\epsilon}^T \left(\boldsymbol{C}^V - \boldsymbol{C}\right) \boldsymbol{\epsilon} \geq 0, \tag{3.9}$$

where $\boldsymbol{\epsilon}$ is Voigt's vector representation of $\boldsymbol{\varepsilon}$. This means $\boldsymbol{C}^V - \boldsymbol{C}$ is a positive semi-definite matrix. Now we use the following theorem which is proved in Appendix B of [46]:

Theorem 4. *Let $\boldsymbol{A}$ and $\boldsymbol{B}$ be $n \times n$ matrices and let the symbol $\boldsymbol{A} \geq \boldsymbol{0}$ denote that $\boldsymbol{A}$ is a positive semi-definite matrix and $\boldsymbol{A} \geq \boldsymbol{B}$ denote $\boldsymbol{A} - \boldsymbol{B} \geq \boldsymbol{0}$. If $\boldsymbol{A} \geq \boldsymbol{B}$ then $\boldsymbol{B}^{-1} \geq \boldsymbol{A}^{-1}$.*

If we apply Theorem 4 to (3.9) then $\boldsymbol{C}^{-1} - \boldsymbol{C}^{-V} \geq \boldsymbol{0}$, it follows that all diagonal entries of $\boldsymbol{C}^{-1} - \boldsymbol{C}^{-V}$ must be non-negative. In particular the $1-1$ component of $\boldsymbol{C}^{-1} - \boldsymbol{C}^{-V}$ is non-negative, that is

$$\frac{1}{E} - \frac{1}{E_V} \geq 0,$$

therefore $E \leq E_V$. The proof that $E_R \leq E$ follows directly from (3.7).

Chapter 4

Quantifying Uncertainties of the In-plane Young's Modulus

Electrodeposited thin films in MEMS devices often show fiber texture resulting in transverse isotropic elastic properties. This is the case for the RF MEMS switches, made of nickel, studied at the Purdue PRISM Center. It is of interest to understand the elastic properties of these devices since these properties play a role in the lifetime and reliability of the switches. For example, larger stiffness of the bridge in these devices increases the pull-in voltage necessary to activate the switch. Higher pull-in voltages accelerate charging of the electrode's dielectric coating, a key failure mechanism in the device [7]. Hence, an accurate estimate of the true modulus is critical to the analysis and design of these MEMS switches.

Texture plays a fundamental role in the mechanical behavior of materials. Indeed, materials of the same type with different crystallographic texture may have different mechanical responses [28]. If the crystallites are oriented preferentially within the film, the Young's modulus of the film can vary significantly from the bulk value. For example, [18] found the in-plane Young's modulus of LIGA nickel structures to be 20% lower than handbook values for bulk polycrystalline Ni. The difference in modulus is observed to be related to the presence of $\langle 001 \rangle$ out-of-plane texture in the samples. This observation is based on calculations, assuming perfect fiber texture, of the average Young's modulus in the $\{001\}$ plane which gives values close to those measured in the microsamples.

Reference [7] demonstrates the importance of accounting for the degree of fiber texture in estimating the in-plane Young's modulus for the nickel polycrystalline bridges in the RF MEMS devices that we are studying. If perfect $\langle 001 \rangle$ out-of-plane texture is assumed, one would obtain an in-plane Young's modulus that is 18% less than the isotropic Young's modulus. However, there is not perfect $\langle 001 \rangle$ fiber texture. There is also a weak $\langle 111 \rangle$ texture present in the samples which has the effect of increasing the in-plane Young's modulus relative to the expected value for a film with perfect $\langle 001 \rangle$ fiber texture. The result is a predicted in-plane Young's modulus that is 5-7% less than the bulk isotropic value of the Young's modulus of nickel [7].

In addition to understanding material properties of devices, the PRISM Center has a focus on quantifying uncertainty in predictions of performance of the devices. Accordingly, we are interested in estimating the probability distribution of material properties for use in downstream simulations aimed at predictions of performance, lifetime or reliability. In this chapter we obtain a probability distribution function (PDF) of the in-plane Young's modulus, rather than a single value, because we take into account that the modulus itself depends on uncertainties due to fabrication conditions that lead to variations in quantities such as grain geometry, individual crystal properties and the crystal orientation distribution. Typically more uncertainty in these quantities leads to more uncertainty in an estimate of the Young's modulus. However, it might be the case that the modulus is not sensitive to variability in some fabrication condition. Thus, that condition would not lead to more uncertainty in predictions of the modulus. It is the aim of this chapter to explore and quantify how uncertainties in the fabrication process affect predictions of the in-plane Young's modulus. A more sharply peaked PDF of the modulus, with less spread, implies less uncertainty and a more spread out distribution means more uncertainty. The better we can quantify the uncertainty in the modulus, the better the downstream predictions based on this modulus will be.

In [18] and [7] estimates of the in-plane Young's modulus are made assuming that (i) the elastic properties of individual crystals are known precisely, and (ii) there is perfect fiber texture [18] or the texture is measured experimentally [7]. Under these circumstances, one can compute an estimate of the effective in-plane Young's modulus from the single-crystal elastic constants and the texture using the classical Hill average [20]. One way to quantify the uncertainty in this estimate is also to calculate the Reuss average [53] and Voigt average [61] which provide lower and upper bounds, respectively. In Section 4.1, the definition of the Hill average in-plane Young's modulus is provided. The Hill average serves as a reasonable prediction in the Reuss-Voigt range. But in principle, the true in-plane Young's modulus is between the Reuss-Voigt range and can be quite far away from Hill's average. If we only count with this information, a reasonable PDF of the in-plane Young's modulus would be a uniform distribution over the Reuss-Voigt range.

In order to obtain more detailed information about the PDF of in-plane Young's modulus, we use numerical simulations. These simulations, described in Section 4.2, necessitate a model for the microstructure geometry of polycrystals and an assignment of fiber texture consistent with experimental observations. With these inputs, and specification of elastic properties of the constituent individual grains, we numerically perform uniaxial tension tests on this microstructure in order to determine the effective modulus. The numerical simulation method is a full-field method based on a fast Fourier Transform (FFT) technique [34]. As an illustration, in Section 4.6, we show that if the texture and the elastic moduli of single crystals are known, then the numerical simulations provide a computed PDF of Young's modulus that is sharply peaked about the Hill average value. This result is insensitive to the underlying microstructure geometry. In Section 4.7, we examine the affect of varying the crystallographic texture and in Sections 4.8 and 4.9 we consider the effect of different types of uncertainty in the single-crystal elastic constants.

4.1 Preliminary Information

In this section we briefly summarize how texture is measured for the PRISM Center MEMS devices. Next we discuss how the Hill's average of the in-plane Young's modulus is defined and finally the implications the Reuss-Voigt averages have on the quantification of uncertainties.

Texture Measurement

In Section 2.3 of Chapter 2 we mentioned that crystallographic texture is typically represented with an ODF. There are several methods for experimentally measuring texture to determine the ODF. The details of efficient and accurate methods used at the PRISM Center can be found in [7]. Briefly, crystal orientation is measured experimentally using 2D X-ray diffraction (XRD). For more details on the XRD method see Appendix A. From the XRD data, texture analyses are then carried out using the Rietveld refinement software MAUD [38] to calculate inverse pole figures. These pole figures are then imported into MTEX [19, 40] for further analysis. Finally MTEX produces a discrete ODF whose format is shown in Table 2.1. This process is done per MEMS device. For illustrative purposes, in our computations we use 10 ODFs named ODF1, ODF2, and so on, corresponding to texture measurements of

10 RF MEMS switches labeled batch #1 in [7].

Calculation of the In-Plane Young's Modulus

We know from Chapter 3 that if the ODF and the crystal elastic constants of a polycrystalline microstructure are known then the effective elastic properties of the sample can be estimated by averaging over the Euler space. The averages we studied are the classical Reuss-Voigt averages. We also showed that some of the elastic constants corresponding to isotropic and transverse isotropic materials are bounded between these averages. In particular we showed that the in-plane Young's modulus $E_{in-plane}$ of transverse isotropic materials is between the Reuss-Voigt averages.

Assume we have a polycrystalline aggregate, let $\mathbb{S}^R$ denote its Reuss average compliance tensor and $\mathbb{C}^V$ its Voigt average stiffness tensor, then its Hill average compliance tensor is defined as follows:

$$\mathbb{S}^{\text{Hill}} = \frac{1}{2}\left(\mathbb{S}^R + \mathbb{S}^V\right),$$

where $\mathbb{S}^V = \mathbb{C}^{-V}$. We know from Chapter 3 that if the sample has fiber texture then the Voigt and Reuss averages, as well as the effective properties exhibit transverse isotropy. If we choose an orthonormal basis, $\mathbf{e}_1$, $\mathbf{e}_2$, $\mathbf{e}_3$, with $\mathbf{e}_3$ perpendicular to the plane of symmetry, then the Hill average in-plane Young's modulus is defined as

$$E^{\text{Hill}}_{in-plane} = \frac{1}{\mathbb{S}^{\text{Hill}}_{1111}} = \frac{1}{\mathbb{S}^{\text{Hill}}_{2222}}. \tag{4.1}$$

Consider the results from [7] for batch #1 devices, reproduced here in Table 4.1. In that work, the single-crystal elastic constants of Ni are assumed known and taken to be C_{11} = 249 GPa, C_{12} = 155 GPa, and C_{44} = 114 GPa, the mean values of experimental measurements shown in Table 4.2 [36]. As noted above, the mean in-plane Young's modulus calculated with the experimental ODF, which is predominantly ⟨001⟩ fiber texture, but also includes weak ⟨111⟩ texture, is intermediate between the mean modulus calculated assuming perfect ⟨001⟩ fiber texture and the bulk isotropic value. However, the range of possible values, given by the Reuss and Voigt bounds, is narrower if perfect ⟨001⟩ fiber texture is assumed compared to the experimental texture. It is observed experimentally that the Hill average modulus is close to experimentally measured effective properties of polycrystals; although, there is no theoretical basis for this observation. Thus, it is reasonable to use the Hill average as an estimate of the true effective response. In order to quantify the uncertainty in this estimate, without any other information, we would assume that any value of the in-plane Young's modulus between the Reuss and Voigt bounds is equally likely. Accordingly, the PDF of in-plane Young's modulus would be a uniform distribution on this range, as illustrated in Fig. 4.1. Notice that different assumptions about texture in the sample significantly impacts the PDF of in-plane Young's modulus, again emphasizing the importance of knowing the ODF for the sample.

	Perfect ⟨001⟩ Texture (GPa)	RF MEMS Switches (batch #1) (GPa)	Uniform Texture (GPa)
$E^{R}_{in-plane}$	163.3	178.8 ± 1.1	192.4
$E^{Hill}_{in-plane}$	172.4	194.7 ± 1.3	209.7
$E^{V}_{in-plane}$	182.7	210.3 ± 1.5	225.7

Table 4.1: The Reuss, Hill, and Voigt average in-plane Young's moduli of three different types of texture: A simulated perfect ⟨001⟩ fiber texture sample, an experimentally measured texture calculated from batch #1 of RF MEMS switches and a uniform texture sample from [7]. Here $E^{R}_{in-plane}$, $E^{Hill}_{in-plane}$ and $E^{V}_{in-plane}$ denote the Reuss, Hill, and Voigt average in-plane Young's moduli respectively.

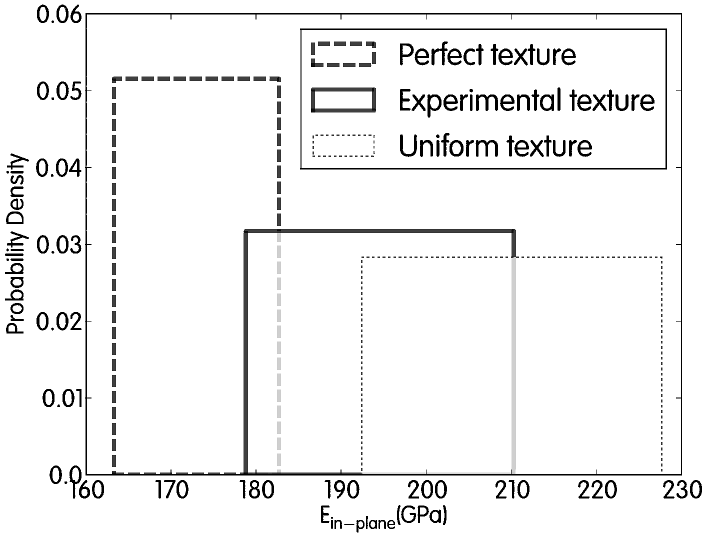

Figure 4.1: PDF of in-plane Young's modulus for perfect texture, experimental texture, and uniform texture assuming a uniform distribution on the Voigt-Reuss range.

	C_{11} GPa	C_{12} GPa	C_{44} GPa
Exp.	249 ± 4	155 ± 7	114 ± 12

Table 4.2: Single Crystal Elastic stiffness constants for Nickel [36].

4.2 Effect of Microstructure Geometry on In-plane Young's Modulus

The uniform distribution determined in the last section is pessimistic. In this section we will see that if we take into account actual geometry of the microstructure, assign grain orientations to the geometry consistent with the experimentally determined ODF, and use numerical simulations to calculate the effective modulus, we greatly reduce the uncertainty in our estimate of the in-plane Young's modulus. For now, we continue to assume we know the elastic moduli of the individual crystals, and use the mean values from Table 4.2. In order to carry out this analysis, we must specify the geometry, the method for assigning texture to that geometry, and the numerical procedure for computing the effective modulus once these specifications are made. We next address these issues in turn.

4.3 Microstructure Geometry

We imagine cutting a small, rectangular parallelepiped sample of approximately 1000 grains from the MEMS devices under consideration. Electrodeposition tends to produce V-shaped columnar grains with the grain axis perpendicular to the plane of the film. A schematic representation of a cross-section of the thin film microstructure is shown in Fig. 5.1 of Chapter 5. We consider the rectangular parallelepiped sample to be at the near top of the thin film where grains tend to be perfectly columnar. Thus, we represent the microstructure geometry of this sample with perfectly columnar grains based on a Voronoi diagram construction. Columnar grains are obtained by distributing generating points for the Voronoi diagram in a single plane, constructing a tessellation of the plane to represent grain cross-sections, and then extending the grain geometry to the third dimension to make columns.

To be more specific, recall the definition of a Voronoi diagram in a plane. Given a non-empty set $\mathcal{R} \subset \mathbb{R}^2$ and a finite set of generating points, $\{p_k\}_{k=1}^N \subset \mathcal{R}$, the Voronoi diagram of $\mathcal{R}$ associated with the points $\{p_k\}_{k=1}^N$ is defined as the collection of all sets of the form

$$V_j = \{x \mid x \in \mathcal{R},\ |x - p_j| \leq |x - p_i| \text{ and for all } i \neq j\}.$$

The set V_j is called the jth Voronoi cell associated with the point p_j. The collection of all cells $\{V_j\}_{j=1}^N$ forms a tessellation of $\mathcal{R}$, each V_j is a convex set, and

$$\bigcup_{j=1}^{N} V_j = \mathcal{R}.$$

In this work the set $\mathcal{R}$ is a rectangle. The cells V_j contained in $\mathcal{R}$ are extended perpendicular to the plane of the rectangle to form columns making a sample that is a rectangular parallelepiped. The extended cells will also be denoted by V_j, and these cells represent crystal grains in the numerically constructed polycrystalline sample.

For numerical purposes, we prefer periodic Voronoi diagrams generated from the regular Voronoi diagrams in the following way:

- Define a rectangle $\mathcal{R} \subset \mathbb{R}^2$.
- Choose uniformly randomly distrubuted generating points in $\mathcal{R}$.
- Extend $\mathcal{R}$ periodically, together with the generating points, in all directions.
- Compute the tessellation of the extended periodic space.
- Compute the intersection between the cells of the periodic space with $\mathcal{R}$. The resulting collection of subsets contained in $\mathcal{R}$ defines the periodic Voronoi diagram of $\mathcal{R}$ associated with the generating points.

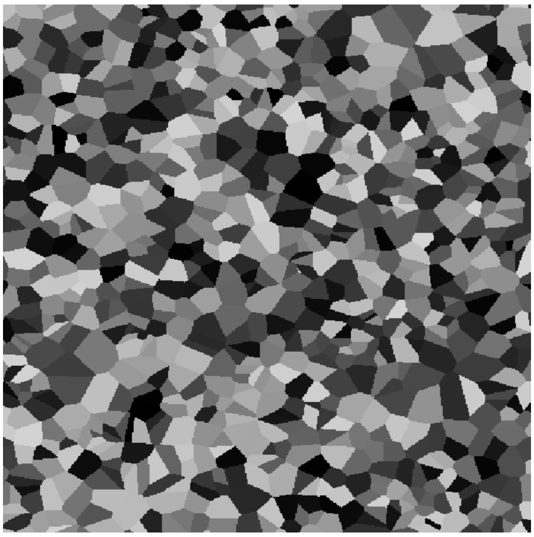

Figure 4.2: Periodic Voronoi diagram composed of 1000 cells.

An example of a two dimensional periodic Voronoi diagram is shown in Fig. 4.2. The next step is to assign orientations to the crystals represented by these Voronoi cells consistent with the experimental ODF.

4.4 The Texture Discretization Algorithm

As we have already seen, the mechanical response of polycrystalline materials is highly influenced by crystallographic texture. Therefore the prediction of effective material properties, like the in-plane Young's modulus of MEMS devices, depends on the accurate numerical representation of the texture. By accurate numerical texture we mean that all numerically generated crystal orientations should statistically represent experimental texture coming from the XRD measurements. The measure that indicates how close the numerical texture is to experimentally measured texture is called misfit. This measure depends on the experimental ODF, which is known, and a recalculated ODF that is obtained from the results of the texture discretization algorithm discussed in this section.

Assume a model microstructure is given, for example one generated using the Voronoi construction of the last section. Note, we are considering microstructures where the grains are of unequal volume. We follow a modified version of the algorithm suggested by [44] to assign orientations to the microstructure. First, the sample is divided into N_u elementary volumes each of identical volume V_u. Each grain contains many elementary volumes.

Next, the Euler space is divided into N cubic cells C_i, $i = 1, 2, \ldots, N$, with a side length of 5°. The volume fraction of each cell in the orientation space is given by

$$f_i = \frac{\int_{C_i} f(\boldsymbol{g}) d\boldsymbol{g}}{\int_{\Omega_0} f(\boldsymbol{g}) d\boldsymbol{g}}, \quad i = 1, 2, \ldots, N.$$

A cumulative distribution function of volume fractions is defined in the following way

$$F(M) = \sum_{i=1}^{M} f_i, \quad 1 \leq M \leq N.$$

By construction, we have $0 < F(M) \leq 1$. Each integer M is identified with a value $F(M)$ and an orientation $\boldsymbol{g}_M$ at the center of C_M. This establishes a 1-1 correspondence between the numbers $F(i)$ and the orientations $\boldsymbol{g}_i$, $i = 1, \ldots, N$.

The texture discretization algorithm or the numerical method that assigns orientations to crystals of a polycrystalline microstructure is summarized in the following four steps:

1. Sample N_u uniformly distributed random numbers between zero and one. Each random number, x, will satisfy $F(i) \leq x < F(i+1)$ for some i, $1 \leq i \leq N$. In this way, identify each x with the orientation $\boldsymbol{g}_i$, producing a list of N_u orientations.

2. Select the biggest grain of the microstructure. Represent the grain with index G, and call N_G the number of elementary volumes in the grain. Randomly select one of the orientations generated in step 1. Find the remaining $N_G - 1$ orientations out of the list so that the disorientation between the first and the remaining is less than a given threshold value. Following [44] we choose 7° for the threshold value.
3. Compute the mean orientation[1] of the N_G orientations selected in step two. The resulting mean orientation is the orientation assigned to grain G. Remove this set of N_G orientations from the list created in step one.
4. Go back to step two and repeat until all grains are selected.

The accuracy of the above algorithm is measured with the misfit

$$\text{Misfit} = \frac{\int_{\Omega_0} \left(f_{\text{exp}}(\boldsymbol{g}) - f_{\text{rec}}(\boldsymbol{g})\right)^2 d\boldsymbol{g}}{\int_{\Omega_0} \left(f_{\text{exp}}(\boldsymbol{g})\right)^2 d\boldsymbol{g}},$$

where f_{exp} stands for the experimental ODF and f_{rec} is the reconstructed ODF from the orientations determined above using the texture discretization algorithm. We calculate f_{rec} with the MTEX software. The input parameters for MTEX are the crystal symmetry, sample symmetry and the volume fractions of both, physical and orientation space. As a rule of thumb, misfits less than 15% are considered acceptable numerical representations of experimental crystallographic texture.

It is possible for this algorithm to fail if we cannot find N_G orientations all within the threshold disorientation. In this case, we use whatever number of orientations that are found within the threshold and compute the mean in step 3 using this reduced number. Independently of the success of step 2 , the accuracy of the algorithm is determined with the misfit.

---

[1] This step may lead to gimbal lock.

4.5 Numerical Method

The polycrystal is modeled as an aggregate of perfectly bonded single-crystal grains with different orientations. We use a spectral formulation [47, 33, 5, 35] to perform virtual uniaxial tension tests on our numerically-generated samples to obtain the effective in-plane Young's modulus of each sample. The numerical method gives the effective elastic response based on full-field micromechanical solutions obtained efficiently using Fast Fourier Transforms (FFT).

The elastic FFT-based formulation uses Green's functions and Fourier transforms to find a strain field, associated with a kinematically-admissible displacement field, that minimizes the average of the local strain energies, fulfilling the constitutive stress-strain relation under the constraint imposed by the stress equilibrium conditions. The problem is solved for a periodic unit cell of material, discretized into a regular grid of points. Since the microstructures of interest are columnar, a $512 \times 512 \times 1$ grid is sufficient for an accurate calculation of $E_{in-plane}$. The use of this grid represents the smallest Voronoi grain with roughly 115 points. Note that only one layer of points is needed through the thickness because the cross-sections of the columnar grains are identical and therefore, have the same mechanical response.

The local elastic constitutive relation is given by

$$\sigma_{ij}\left(\boldsymbol{x}\right) = C_{ijkl}\left(\boldsymbol{x}\right)\varepsilon_{kl}\left(\boldsymbol{x}\right) \tag{4.2}$$

where C_{ijkl} are the components of the anisotropic local elastic stiffness tensor, functions of the grain orientation associated with point $\boldsymbol{x}$. Adding and subtracting an expression involving C^0_{ijkl}, the components of the stiffness of a reference linear medium, from the stress, gives

$$\sigma_{ij}\left(\boldsymbol{x}\right) = \sigma_{ij}\left(\boldsymbol{x}\right) + C^0_{ijkl}u_{k,l}\left(\boldsymbol{x}\right) - C^0_{ijkl}u_{k,l}\left(\boldsymbol{x}\right), \tag{4.3}$$

where $u_{k,l}\left(\boldsymbol{x}\right)$ is the displacement gradient tensor, i.e.

$$\varepsilon_{kl}\left(\boldsymbol{x}\right) = \left(u_{k,l}\left(\boldsymbol{x}\right) + u_{l,k}\left(\boldsymbol{x}\right)\right)/2.$$

Regrouping terms in (4.3)

$$\sigma_{ij}\left(\boldsymbol{x}\right) = C^0_{ijkl} u_{k,l}\left(\boldsymbol{x}\right) + \varphi_{ij}\left(\boldsymbol{x}\right), \tag{4.4}$$

where the polarization field is given by

$$\varphi_{ij}\left(\boldsymbol{x}\right) = \sigma_{ij}\left(\boldsymbol{x}\right) - C^0_{ijkl} \varepsilon_{kl}\left(\boldsymbol{x}\right), \tag{4.5}$$

and combining expression (4.5) with the equilibrium equation $\sigma_{ij,j}\left(\boldsymbol{x}\right) = 0$, we obtain

$$C^0_{ijkl} u_{k,lj}\left(\boldsymbol{x}\right) + \varphi_{ij,j}\left(\boldsymbol{x}\right) = 0. \tag{4.6}$$

Solving differential equation (4.6) for a periodic unit cell under an applied strain $E_{ij} = \langle \varepsilon_{ij}\left(\boldsymbol{x}\right) \rangle$ using the Green's function method requires writing the following auxiliary problem

$$C^0_{ijkl} G_{km,lj}\left(\boldsymbol{x} - \boldsymbol{x'}\right) + \delta_{im} \delta\left(\boldsymbol{x} - \boldsymbol{x'}\right) = 0, \tag{4.7}$$

where $G_{km}\left(\boldsymbol{x}\right)$ is the Green's function associated with the displacement field $u_k\left(\boldsymbol{x}\right)$. The solution for the displacement gradient is given by the convolution integral

$$u_{k,l}\left(\boldsymbol{x}\right) = \int_{\mathbb{R}^3} G_{ki,jl}\left(\boldsymbol{x} - \boldsymbol{x'}\right) \varphi_{ij}\left(\boldsymbol{x'}\right) d\boldsymbol{x'}. \tag{4.8}$$

Solving (4.8) in Fourier space using the convolution theorem, the compatible strain field deriving from the solution of (4.8) is given by

$$\varepsilon_{ij}\left(\boldsymbol{x}\right) = E_{ij} + FT^{-1}\left(\text{sym}\left(\hat{\Gamma}^0_{ijkl}\left(\boldsymbol{k}\right)\right) \hat{\varphi}_{kl}\left(\boldsymbol{k}\right)\right) \tag{4.9}$$

and (4.2) can be used to obtain the corresponding stress field. In (4.9), the hat symbol "ˆ" indicates Fourier transform (FT) and $\boldsymbol{k}$ is a point (frequency) in Fourier space. The Green operator in Fourier space, which is only a function of the reference stiffness tensor and the frequency, is given by

$$\hat{\Gamma}^0_{ijkl}\left(\boldsymbol{k}\right) = -k_j k_l \hat{G}_{ik}\left(\boldsymbol{k}\right), \tag{4.10}$$

with $\hat{G}_{ik}\left(\boldsymbol{k}\right) = \left[C^0_{kjil} k_l k_j\right]^{-1}$. Since the polarization field, defined in (4.5), is precisely a function of the sought strain field, an iterative procedure is required, such that the i-guess of the strain field $\varepsilon^i_{ij}\left(\boldsymbol{x}\right)$ is used in (4.2) through (4.8) to obtain the $(i+1)$-guess $\varepsilon^{i+1}_{ij}\left(\boldsymbol{x}\right)$ given by (4.9), until two consecutive strain fields coincide within a certain tolerance.

Note that, while (4.2) through (4.10) are valid for arbitrary material points $\boldsymbol{x}$ and frequencies $\boldsymbol{k}$, the numerical method consists in evaluating these expressions in points and frequencies belonging to regular grids (of the same size) in Cartesian and Fourier spaces, respectively, in which case, the direct and inverse Fourier Transforms in (4.10) become discrete, and the FFT algorithm can be applied.

While the algorithm described above solves the problem for a fully imposed strain tensor, the actual boundary conditions (BCs) applied to the unit cell can be mixed, i.e. some components of macroscopic strain E_{ij} and some complementary components of the macroscopic stress Σ_{ij} may be imposed. In particular, in the case of tension along x_1 for the calculation of the in-plane Young's modulus, $E_{11} > 0$ and $\Sigma_{22} = \Sigma_{33} = 0$ are the imposed diagonal strain and stress components. In such mixed BC cases, the algorithm should include the following extra step, after $\sigma^{i+1}\left(\boldsymbol{x}\right)$ is determined by means of (4.9) and (4.2). If component Σ_{pq} is imposed, the corresponding $(i+1)$-guess for strain component E^{i+1}_{pq} is obtained as [45]

$$E^{i+1}_{pq} = E^i_{pq} + C^{0-1}_{pqkl} \alpha^{(kl)} \left(\Sigma_{kl} - \left\langle \sigma^{i+1}_{kl}(\boldsymbol{x}) \right\rangle\right),$$

where $\alpha^{(kl)} = 1$ if component Σ_{kl} is imposed, and zero otherwise.

4.6 Calculation of the In-Plane Young's Modulus

In this section, we examine how the in-plane Young's modulus $E_{in-plane}$, is affected by microstructure geometry. We study this effect by generating many microstructures of different geometries and use known texture and elastic crystal constants. The $E_{in-plane}$ is measured for each microstructure and then a numerical PDF is generated. The accuracy of the numerical PDF depends on a precise calculation of $E_{in-plane}$ per realization and on the total number of realizations.

The accuracy of each realization depends on the input parameters of the texture discretization algorithm and the FFT-based method. In the case of the texture discretization algorithm, the input parameters are the experimental ODF, number of grains, grain volume fraction of each grain, number of elementary volumes and the threshold disorientation angle. The output of the algorithm is a set of grain orientations or numerical texture. The measure of the accuracy of the algorithm is determined by the misfit. A low misfit, usually less than 15%, indicates that the numerical texture is close to the experimental texture.

We test the input parameters for the texture discretization algorithm using one of the experimental ODFs, ODF2. The input parameters that lead to low misfits are determined by applying the texture discretization algorithm to different numerical microstructures with different numbers of grains and grain sizes. With 20,000 elementary volumes and a 7° threshold disorientation angle misfits less than 15% are obtained. We also conclude that working with a 1000-grained microstructure is sufficient to get low misfits. These numbers are also suggested in [44].

The next step consists in determining the input parameters of the FFT method. In this case, the input parameters are the numerical microstructure geometry, numerical texture, crystal constants, the Fourier grid size, the error tolerance and the maximum number of iterations. The microstructure geometry and numerical texture are already known from the texture discretization algorithm. We use the same crystal constants of the last section, $C_{11} = 249$ GPa, $C_{12} = 155$ GPa, and $C_{44} = 114$ GPa, in order to compare with the results of that section. The error tolerance and the maximum number of iterations are previously determined. Because the input parameters of the texture discretization algorithm produce misfits less than 15% and the FFT method converges so that all reported digits of $E_{in-plane}$ are correct within the error tolerance, we conclude $E_{in-plane}$ is calculated accurately per realization.

Knowing $E_{in-plane}$ is calculated accurately, we next determine the total number of realizations of $E_{in-plane}$ required to capture the correct statistics. To answer this question, we generate a fixed 1000-grained microstructure and apply the texture discretization algorithm using ODF2 to the same microstructure 700 times obtaining as a result 700 different numerical textures. All misfits have values less than 12%. The $E_{in-plane}$ is calculated for each texture with the FFT method leading to the histogram shown in Fig. 4.3.

The mean and standard deviation of the PDF are 193.6 GPa and 0.32 GPa respectively. In [7], the Reuss, Voigt and Hill estimates (4.1) are calculated for the ten experimental ODFs, as listed in Table 4.1. The PDF values shown in Fig. 4.3 are consistent with the inequalities, $E^{R}_{in-plane} \leq E_{in-plane} \leq E^{V}_{in-plane}$. It is interesting to see that our improved mean $E_{in-plane}$ value, 193.6 GPa, is close to the Hill average. The numerical simulations have allowed us to greatly reduce the uncertainty in the predicted in-plane Young's modulus compared to the uniform distribution over the interval given by lower and upper bounds provided by the Reuss and Voigt averages.

To test the robustness of the computed PDF with respect to the number of realizations, we reduce the number of realizations. With 300 realizations, the PDF of $E_{in-plane}$ still has approximately the same shape, mean and standard deviation values of Fig. 4.3. This observation allows us conclude that 300 realizations of $E_{in-plane}$ are sufficient for the generation of an accurate PDF.

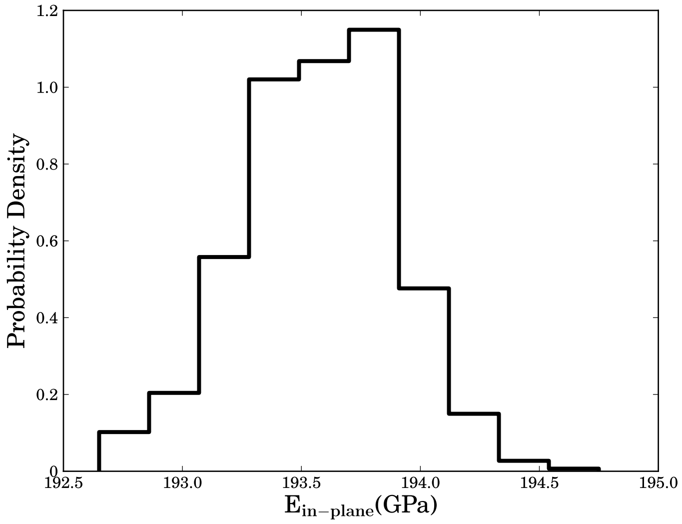

Figure 4.3: PDF of $E_{in-plane}$ based on 700 realizations of the texture distribution. The textures are generated to be statistically consistent with ODF2. The geometry and crystal properties are fixed.

In the next numerical experiment we study how the PDF of $E_{in-plane}$ is affected by uncertainties in microstructure geometry. We generate 300 different microstructures and assign texture to each one. The crystallographic texture for each geometry is chosen to be statistically the same as the experimental ODF2. The misfits for the generated texture are all less than 12%. The crystal elastic constants are fixed over all realizations with the mean values given in Table 4.2. The $E_{in-plane}$ is computed numerically for each microstructure and a PDF is generated. In Fig. 4.4a we compare the PDF of Fig. 4.3 based on one geometry with the PDF of $E_{in-plane}$ that includes geometric uncertainties. We see that both histograms essentially coincide. Indeed, the mean and standard deviation of the new PDF are 193.5 GPa and 0.33 GPa, respectively. All values are centered around the Hill average in both PDFs. Fig. 4.4b shows a plot of the PDFs in the Reuss-Voigt range. The sharpness of both PDFs makes us conclude that $E_{in-plane}$ is not sensitive to geometric uncertainties. Clearly, the Hill average provides a good prediction of $E_{in-plane}$.

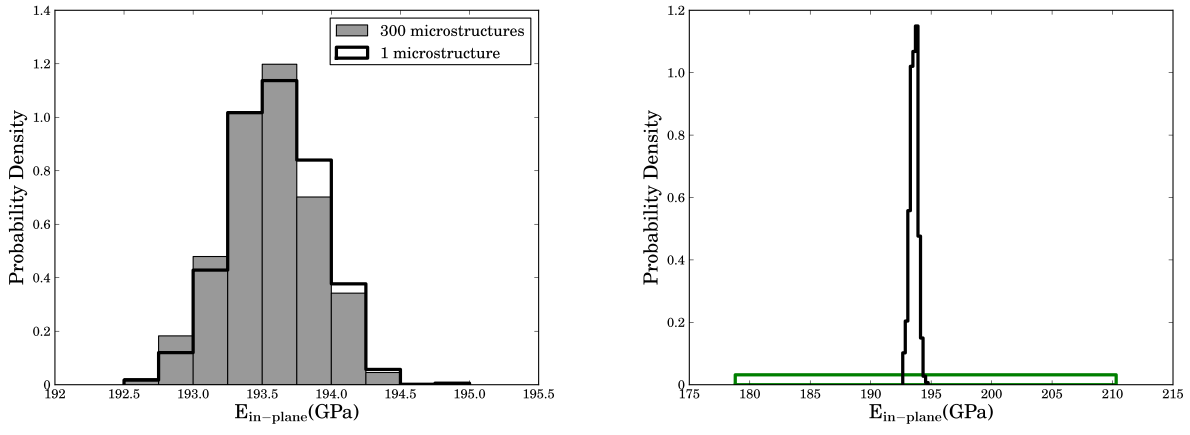

(a) (b)

Figure 4.4: (a) Comparison of PDF of in-plane Young's modulus based on one microstructure and 300 microstructures. (b) The same PDFs as in (a) plotted along with the uniform distribution from Fig. 4.1 for experimental texture.

4.7 Effect of Uncertainties in Crystallographic Texture

In this section, we examine how variations in texture affect the distribution of $E_{in-plane}$. The microstructure geometry and crystal elastic constants are fixed over all realizations. The elastic constants are the same as those used previously, and the microstructure is fixed at the 1000-grained microstructure used to generate Fig. 4.3. Crystallographic texture uncertainties are taken into account by computing $E_{in-plane}$ using the ten different experimental ODFs in batch #1 of MEMS devices [7]. For each experimental ODF we do 300 realizations of $E_{in-plane}$ values, resulting in 3000 numerical values of $E_{in-plane}$ for all ten experimental ODFs. The resulting PDF is shown in Fig. 4.5. The PDF is trimodal, this can be explained in terms of the ODF misfits, and the mean and the standard deviation of the $E_{in-plane}$ values for each of the 300 realizations per ODF.

The minimum and maximum misfit between the experimental ODF and the 300 numerically generated, discrete ODFs, the mean $E_{in-plane}$ and the standard deviation are summarized in Table 4.3 for each of the 10 experimental ODFs. From the table, we deduce that the two peaks located at the rightmost of Fig. 4.5 correspond to contributions of ODF4 and ODF8 since the mean values of each of the 300 $E_{in-plane}$ values for these two ODFs is larger (196-7 GPa) than the mean values of the 300 $E_{in-plane}$ values for the other ODFs (193-4 GPa).

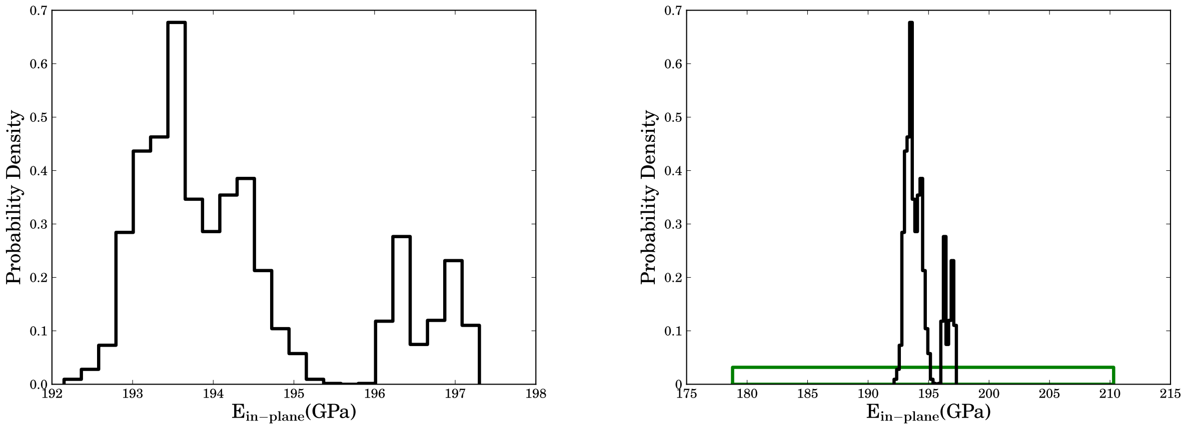

(a) (b)

Figure 4.5: (a) PDF of the in-plane Young's modulus computed using the 10 ODFs in batch #1 of MEMS devices [7], illustrating the effect of crystallographic texture on the PDF. (b) The same PDF as in (a) plotted along with the uniform distribution from Fig. 4.1 for the experimental texture.

In Table 4.4 we list the misfits between the ten experimental ODFs. The entries of Table 4.4, computed with MTEX, are percent misfit. Note that the maximum misfit per column, except for columns four and eight, occur at rows four and eight. Columns four and eight tend to have the largest misfits. The misfits of columns four and eight are smallest only at rows four and eight. This means ODF4 and ODF8 are almost the same but different from the rest of the experimental ODFs. This observation leads us to expect that the PDF of $E_{in-plane}$ generated by the ten ODFs

ODF	min-misfit(%)	max-misfit(%)	Mean $E_{in-plane}$	Std $E_{in-plane}$
1	9.8	11.2	193.0	0.31
2	9.7	11.0	193.5	0.32
3	9.7	11.0	193.6	0.31
4	13.8	14.2	197.0	0.13
5	10.0	11.5	194.3	0.33
6	9.9	11.5	194.5	0.34
7	11.7	12.2	193.5	0.13
8	13.1	13.5	196.3	0.12
9	12.1	12.5	193.1	0.13
10	10.1	11.4	194.2	0.33

Table 4.3: Crystallographic texture misfits, mean and standard deviation values of $E_{in-plane}$.

is trimodal. The rightmost two peaks correspond to contributions of ODF4 and ODF8 since both have similar mean $E_{in-plane}$ values and small standard deviations. The leftmost peak corresponds to the rest of the ODFs. The gap between the two peaks is pronounced because all standard deviations are small as we can see from Table 4.3.

Note that the $E_{in-plane}$ values shown in Fig. 4.5 are consistent with the theoretical estimate $E^R_{in-plane} \leq E_{in-plane} \leq E^V_{in-plane}$. Still, the numerically calculated PDF is substantially narrower than a uniform distribution over the Reuss-Voigt range, as can be seen in Fig. 4.5b.

The misfits of Table 4.3 are less than 15%, as expected from the numerical construction. The PDF has $E_{in-plane}$ values ranging from 192.2 GPa to 197.3 GPa with a mean of 194.3 GPa and standard deviation of 1.3 GPa. We conclude that the variability in the texture due the manufacturing process leads to a small change in the mean $E_{in-plane}$ values. Indeed, a change of approximately 5 GPa in $E_{in-plane}$ is observed when uncertainties in an experimental ODF are within 16.1%. As a consequence, MEMS devices coming from the same manufacturing process with fiber

ODF	1	2	3	4	5	6	7	8	9	10
1	0	4.4	4.6	15.3	6.3	7.1	4.3	12.2	5	5.9
2	4.4	0	0.8	14.6	3	4.3	3.6	12.8	6.4	4.2
3	4.6	0.8	0	14.4	3.4	4.7	3.4	12.7	6.6	4.8
4	15.3	14.6	14.4	0	14.9	16.1	13	6	14.7	15.8
5	6.3	3	3	14.9	0	2.2	4.2	12.3	6.2	2.1
6	7.1	4.3	4.7	16.1	2.2	0	6.2	13.6	7.5	2.3
7	4.3	3.6	3.4	13	4.2	6.2	0	9.8	4.5	5.6
8	12.2	12.8	12.7	6	12.3	13.6	9.8	0	10.7	12.8
9	5	6.4	6.6	14.7	6.2	7.5	4.5	10.7	0	5.8
10	5.9	4.2	4.8	15.8	2.1	2.3	5.6	12.8	5.8	0

Table 4.4: Misfits between experimentally measured ODFs.

crystallographic textures within uncertainty errors of about 16% will tend to have the same in-plane Young's moduli. This is true provided that the individual crystal constants are identical for all crystals and all devices.

4.8 Effect of Uncertainties in Single-Crystal Elastic Constants

So far, our simulations have assumed that the single-crystal elastic constants are known. In this section we study how $E_{in-plane}$ is affected by uncertainties in the single-crystal elastic moduli under various scenarios. A closer look at [36] reveals that the values given in Table 4.2 have variability arising from averaging experimental results over nine experiments using different experimental techniques on nominally pure nickel with varying amounts of impurities. If, as in the case of the PRISM MEMS devices, we do not have information about the impurites, then it is reasonable to assume the uncertainties in crystal properties are given by the range of values in Table 4.2. Thus, we start by considering nickel crystal constants ranging over all the experimental values

$$\begin{aligned} 245 \text{ GPa} &\leq C_{11} \leq 253 \text{ GPa}, \\ 148 \text{ GPa} &\leq C_{12} \leq 162 \text{ GPa}, \\ 102 \text{ GPa} &\leq C_{44} \leq 126 \text{ GPa}. \end{aligned} \tag{4.11}$$

We can see from (4.11) that experimental crystal constants deviate from 1.6% up to 10.5% with respect to their mean values. The biggest uncertainty range occurs in C_{44}. Since the PDFs of C_{11}, C_{12} and C_{44} are not known, an overestimate of uncertainty is obtained if these constants are independently distributed and each is uniformly random. We expect this assumption to give an overestimate because we believe that these elastic constants are correlated.

Simulations in this section fix the microstructure geometry and the crystallographic texture over all the realizations. The geometry is the same 1000-grained microstructure used previously and the texture is generated using ODF2 with a misfit less than 12%. For this microstructure, we generate realizations of the single-crystal constants to examine their effect on the prediction of $E_{in-plane}$. In order to sample and cover the whole range of constants described by (4.11), we apply latin hypercube sampling [43] with 350 samples.

In Fig. 4.6a we compare the resulting numerical PDF of $E_{in-plane}$ with the PDF shown in Fig. 4.3 which uses the same geometry. The wide PDF corresponds to uncertain crystal constants. The mean and standard deviation of the wide PDF are 192.8 GPa and 6.6 GPa, respectively. The wide spread indicates that the in-plane Young's modulus is sensitive to uncertainties in crystal elastic moduli. Note that the mean value 192.8 GPa is still close to the Hill average, 194.7 GPa, even with the spread in $E_{in-plane}$. The minimum and maximum $E_{in-plane}$ values of Fig. 4.6a for the wide distribution are 176.6 GPa and 207.0 GPa, respectively. Coincidentally, as shown in Fig. 4.6b, the wide distribution of these moduli falls approximately on the uniform distribution over the interval [178.8 GPa, 210.3 GPa] obtained using

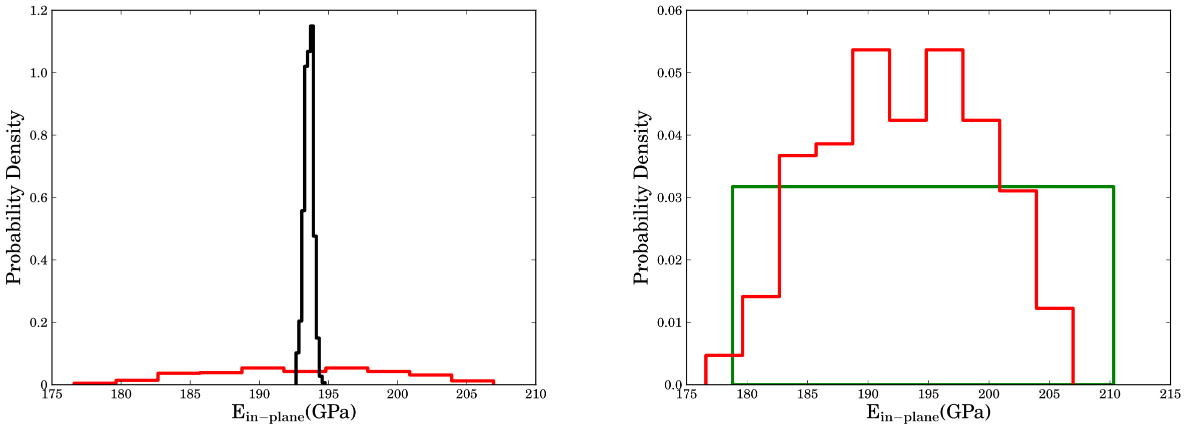

(a) (b)

Figure 4.6: (a) Comparison between the PDF of Fig. 4.3 and the PDF of in-plane Young's modulus when uncertainties in single-crystal elastic constants are taken into consideration. (b) The wide PDF of (a) plotted along with the uniform distribution from Fig. 4.1 for experimental texture.

the Hill average and the experimental texture as in Fig. 4.1. Note that some of the predicted $E_{in-plane}$ values are less than the Reuss average. This does not contradict the result $E^{R}_{in-plane} \leq E_{in-plane} \leq E^{V}_{in-plane}$ proved in Chapter 3, indeed, in this numerical experiment we are sampling uniformly over the range of crystal constant values (4.11), while the Reuss-Voigt range [178.8 GPa, 210.3 GPa] corresponds to the mean values $C_{11} = 249$ GPa, $C_{12} = 155$ GPa and $C_{44} = 114$ GPa.

Each choice of single-crystal constants in each realization that goes into computing the wide PDF in Fig. 4.6a, itself can be associated with a Reuss, Voigt or Hill average. Computing these averages for the experimental texture given by ODF2 using MTEX provides some insight into the result in Fig. 4.6. Figure 4.7 shows the distribution of Reuss, Voigt and Hill estimates for the same 350 crystal values used to generate Fig. 4.6. The PDF shown with a solid line at the center of Fig. 4.7 corresponds to $E^{H}_{in-plane}$ and is approximately the same wide PDF of Fig. 4.6a. The PDFs shown at the left in red and at the right in blue in Figure 4.7, correspond

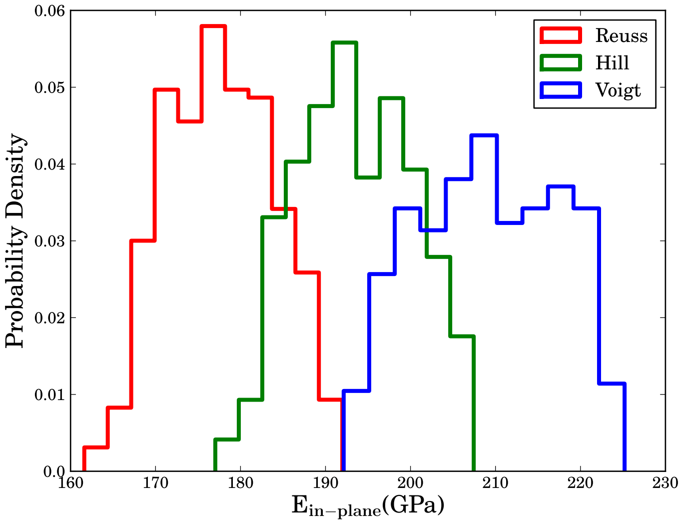

Figure 4.7: Numerical PDFs of Reuss, Hill and Voigt estimates based on 350 samples of crystal values from (4.11) and using the experimental texture given by ODF2.

to $E^R_{in-plane}$ and $E^V_{in-plane}$ respectively. All $E_{in-plane}$ values have as upper and lower bounds $E^V_{in-plane}$ and $E^R_{in-plane}$, consistent with theory.

The scenario assumed in this section is that we have no knowledge of the specific alloy, and thus base our uncertainty in the single-crystal elastic constants on the uncertainty across many experimental measurements of different alloys. The results can also be interpreted as the uncertainty due to experimental error in measurements of a single alloy. In such a case, we might not expect the range of values to be quite as large as (4.11), but we expect the same qualitative results. If the uncertainty in the range of constants is smaller, the uncertainty in the predicted PDF of $E_{in-plane}$ would be reduced.

4.9 Uncertainties using Correlated Single-Crystal Elastic Constants

In this section we compute the PDF of $E_{in-plane}$ based on more detailed experimental measurements of the elastic crystal constants. Again, we use the same microstructure and crystallographic texture of the previous section. However, in the previous section we assume that uncertainties in the single-crystal constants distributed uniformly randomly over their range of values. This assumption is not based on experimental evidence, but on a conservative assumption that probably gives larger uncertainty than in reality. Nevertheless, it is the best assumption possible if the correlation among the crystal constants is not known.

In [11] and [55], the elastic constants of nickel-copper alloys are measured. Both references report that the nickel elastic constants have a piecewise linear behavior when expressed as a function of nickel concentration. For nickel concentrations from 100% down to 70%, there is a linear relationship between crystal constants and concentration. A deviation occurs for nickel concentrations lower than 70%, but the breakdown of the linear behavior is considered small so that a linear least squares fit of the experimental data gives very good estimates of the nickel crystal constants. In Fig. 4.8 we show graphically the dependence of the nickel elastic constants on the amount of copper concentration in the nickel-copper alloy. The horizontal axis represents the percentage of copper in the alloy. The vertical axis is in GPa. From bottom to top, the lines represent C_{44}, C_{12} and C_{11}. All lines are least squares fits of the experimental data reported in [11]. Explicitly the linear relationships are

$$\begin{aligned} C_{11} &= -78.13\eta + 245.63, \\ C_{12} &= -34.13\eta + 155.59, \\ C_{44} &= -48.50\eta + 123.55, \end{aligned} \tag{4.12}$$

where $0 \leq \eta \leq 1$ is the copper concentration.

Now assume our device is composed of the nickel-copper alloy from [11] and that the copper concentration is at most of 30%, that is, $0 \leq \eta \leq 0.3$. Then from (4.12) we have

$$\begin{aligned} 222.19 \text{ GPa} \leq & C_{11} \leq 245.63 \text{ GPa}, \\ 145.35 \text{ GPa} \leq & C_{12} \leq 155.59 \text{ GPa}, \\ 109.00 \text{ GPa} \leq & C_{44} \leq 123.55 \text{ GPa}. \end{aligned} \tag{4.13}$$

There is a 3-6% variability in these single-crystal elastic constants over this range of copper concentration.

Next, we generate the PDF of the in-plane Young's modulus based on the uncertainties given by (4.12) and (4.13). The main difference between this scenario and the one of the previous section is that now C_{11}, C_{12} and C_{44} are correlated. Once the copper concentration η is known, then the crystal constants are also known from (4.12). Therefore, we only need to sample over η, $0 \leq \eta \leq 0.3$. We assume η has a uniformly random distribution in this range. To be consistent with the previous section we use 350 realizations, however this number is larger than needed to capture the statistics.

Figure 4.9 shows the computed PDF of $E_{in-plane}$ based on different realizations of η in $0 \leq \eta \leq 0.3$. The wide PDF of Fig. 4.9a corresponds to this case. For comparison we also show the PDF of Fig. 4.3 which uses the same microstructure, the mean single-crystal elastic constants from Table 4.2, and varies the texture consistent with experimental ODF2. The wide distribution in Fig. 4.9 has minimum and maximum $E_{in-plane}$ values of 169.95 GPa and 196.8 GPa. Many of these $E_{in-plane}$ values are outside the Reuss-Voigt range [178.8 GPa, 210.3 GPa] because we are sampling over a subset of (4.13), while the Reuss-Voigt range [178.8 GPa, 210.3 GPa] corresponds to $C_{11} = 249$ GPa, $C_{12} = 155$ GPa and $C_{44} = 114$ GPa. The mean and standard deviation of the $E_{in-plane}$ values are 184.04 GPa and 7.11 GPa, respectively. The mean value, 184.04 GPa, is smaller than that of Fig. 4.6 because the crystal constants

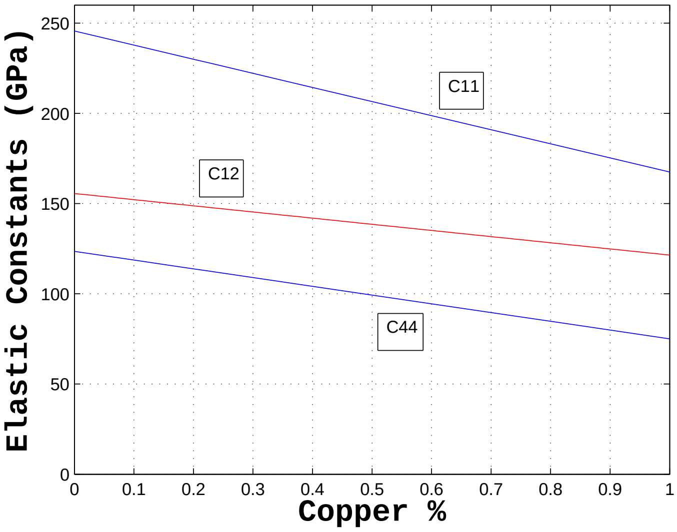

Figure 4.8: Elastic constants of nickel-copper alloys. The horizontal axis represents copper concentration.

C_{11} and C_{12} of (4.13) tend to be smaller than the ones listed in Table 4.2 and (4.11). The values of C_{44} shown in (4.13) and (4.11) are similar. However, the range of values, *i.e.*, the width of the distribution is similar. Surprisingly, the fact that the constants are correlated reduces the width of the PDF only slightly. This is better appreciated from Figure 4.9b, where the wide PDF of Fig. 4.9a is plotted along with the uniform distribution from Fig. 4.1 for experimental texture. Based on Fig. 4.9 we again conclude that $E_{in-plane}$ is sensitive to uncertainties in single-crystal elastic properties, even when these constants are correlated.

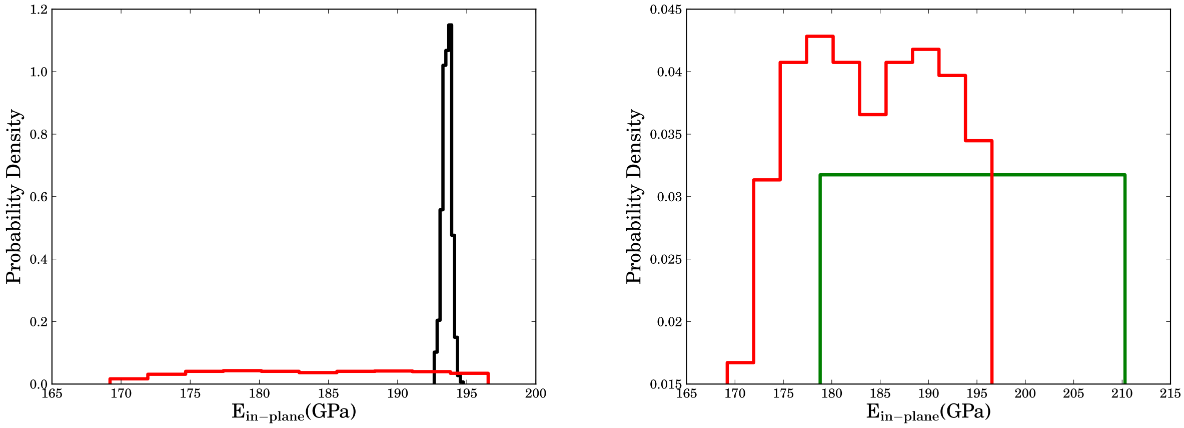

(a) (b)

Figure 4.9: (a) Comparison between the PDF of Fig. 4.3 and the PDF of in-plane Young's modulus when uncertainties in single-crystal elastic constants are correlated by (4.12). (b) The wide PDF of (a) plotted along with the uniform distribution from Fig. 4.1 for experimental texture.

Chapter 5

Microstructure Modeling

In this chapter we propose a more accurate microstructure model of the polycrystalline thin Ni film shown in Fig. 1.1. It is known from experiments that the geometry of the Ni crystals depends of the film thickness. Grains located at the bottom of the film are equiaxed and grains at the top of the film tend to be V-shaped columnar. As a consequence, the average in-plane grain size also changes as a function of film thickness. Average in-plane grain sizes are smaller at the bottom of the membrane and bigger at the top.

A schematic representation of the polycrystalline microstructure is shown in Fig. 5.1. The film thickness is represented from bottom to top and the film width or film length is represented from left to right. No information is known about the schematic representation of the transverse geometry of the grains except the size distribution. The V-shaped columnar grains represent the Ni layer of the membrane and its thickness ranges from $1\mu m$ to $3\mu m$. The horizontal black band represents a Ni layer characterized by having equiaxed grains with sizes of the order of the nanometers. Along the bottom is a titanium (Ti) layer approximately $250\AA$ thick, that we ignore because it represents $0.83\% - 2.5\%$ of the Ni layer.

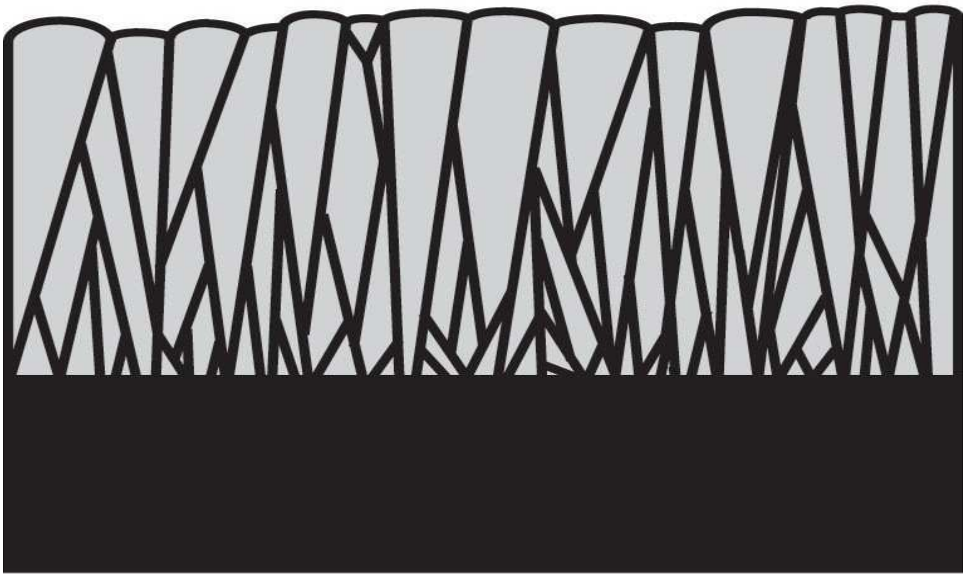

Figure 5.1: Sketch of a cross-section of the film microstructure showing representative grain geometry in a slice through the thickness of the Ni film.

Define a right-handed coordinate system with origin at the bottom left of Fig. 5.1 with positive x axis pointing to the right and positive z axis pointing upwards. If h represents the film thickness, L_x the film length and L_y the film width, then the polycrystalline membrane is contained in the the domain $\Omega = [0, L_x] \times [0, L_y] \times [0, h]$.

Based on the transmission electron microscopy (TEM) technique it has been observed that the average in-plane grain size of the microstructure as a function of the film thickness changes as follows (Patrick Cantwell, Lehigh University, personal communication):

- The average in-plane grain size d is an increasing function of z and it obeys the power law $d(z) = z^{0.58}$.
- For any fixed $0 \leq z \leq h$, the in-plane grain sizes distribute log-normally.

The measurements of the average in-plane grain sizes are summarized in Table 5.1.

Film thickness	Average in-plane grain size	Grain morphology
$0nm - 200nm$	$20 \pm 8nm$	equiaxed
$200nm - 600nm$	$28 \pm 17nm$	equiaxed
$600nm - 1\mu m$	$35 \pm 26nm$	V-shaped
$1\mu m - 1.6\mu m$	$61 \pm 47nm$	V-shaped
$1.6\mu m - 2.8\mu m$	$125 \pm 60nm$	V-shaped

Table 5.1: In-plane grain sizes as a function of film thickness.

The average in-plane grain sizes are expressed in the form $d \pm \sigma_d$, where σ_d is the standard deviation and d is the mean grain size. The log-normal in-plane grain size distributions as a function of z are shown in Fig. 5.2 (Patrick Cantwell, personal communication).

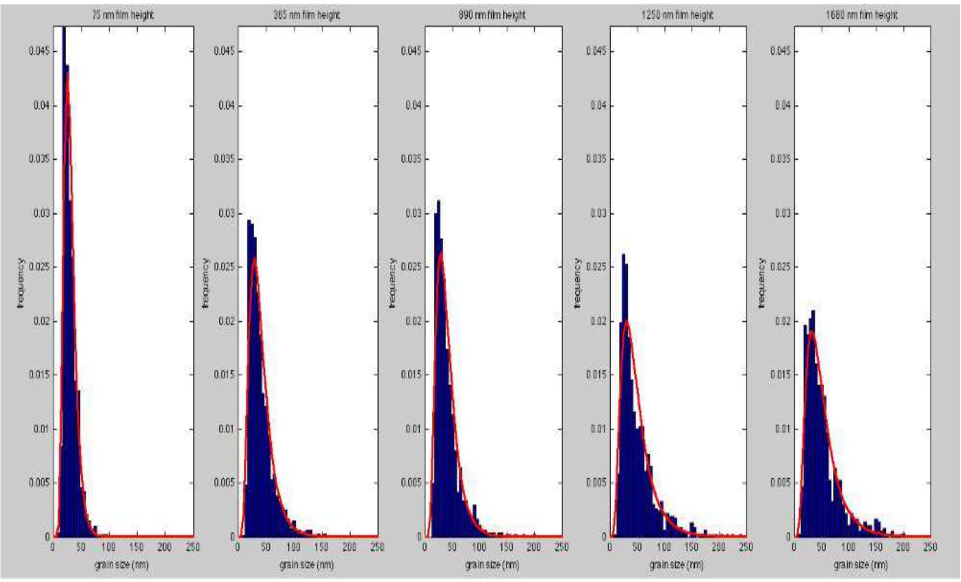

Figure 5.2: Log-normal in-plane grain size distributions as a function of z. From left to right, the values of z are: $75nm$, $365nm$, $890nm$, $1.25\mu m$ and $1.680\mu m$. The horizontal axis represents in-plane grain size and for all plots the range is $[0nm, 250nm]$. The vertical axis represents probability density (Patrick Cantwell, personal communication).

In this chapter we attempt to develop an algorithm that generates the microstructure geometry shown in Fig. 5.1. The algorithm is based on Voronoi diagram methods, additionally the algorithm captures the two experimental features mentioned above. The numerical in-plane grain sizes are tested with the experimental data shown in Fig. 5.2. This chapter is organized as follows: We start by generating simple geometries based on Voronoi diagram methods. Each simple geometry captures a feature of the schematic representation shown in Fig. 5.1. For example, we develop techniques that allow us to generate perfect columnar grains, perfect columnar grains with peaked bottoms and perfect columnar grains with in-plane grain sizes distributing log-normally. The perfect columnar grains describe the top part of the microstructure well and the peaks describe the bottom part of the columns of the microstructure. The perfect columnar grains with in-plane grain sizes distributing log-normally capture the two desired experimental features. Finally, the complete geometry sketched in Fig. 5.1 is described by combining systematically the techniques that generate simple geometries.

5.1 Some Voronoi Diagram Techniques

In this section we develop techniques that generate the following simple microstructure geometries:

- Perfect columnar microstructures.
- Almost V-shaped grains.
- A perfect columnar microstructure with in-plane grain sizes distributing log-normally.

These geometries can be generated by distributing Voronoi seeds systematically over the physical volume Ω. For simplicity, we illustrate the techniques in two dimensional rectangular domains. The extension to three dimensions follows naturally from the two dimensional case.

Perfect columnar grained microstructures

Consider the rectangular domain $\Omega = [0,1] \times [0,1]$. It is clear from the definition of Voronoi cell that if all seeds are of the form $\{(x_i, y)\}_{i=1}^{N}$, where N is the number of seeds and $0 \leq y \leq 1$ is fixed, then the Voronoi cells are N rectangles whose heights are unit length segments parallel to the y axis and the bases are limited by the perpendicular bisectors of the points $\{x_i\}_{i=1}^{N} \cup \{0,1\}$. A similar situation occurs if the seeds are of the form $\{(x, y_i)\}_{i=1}^{N}$, where N is the number of grains and $0 \leq x \leq 1$ is fixed. Fig. 5.3 illustrates these two cases for $N = 6$. **Note that the value of y or x is irrelevant, as long as all seeds lie along a line the Voronoi cells will be perfectly columnar**.

5.2 Almost V-shaped grains

V-shaped grains are generated by modifying the perfect columnar microstructure. First the seeds are distributed along a segment to generate perfectly columnar grains, then the seed that is closest to a grain boundary is displaced perpendicularly to the line of seeds. The displacement must be small enough so that the seed is still contained in Ω. Then the next closest seed is displaced perpendicularly out of the line but in an opposite direction to the previous displaced seed and so on until all seeds are displaced perpendicularly to the segment. The Voronoi diagram that results from this seed configuration is a set composed of almost V-shaped grains. For example,

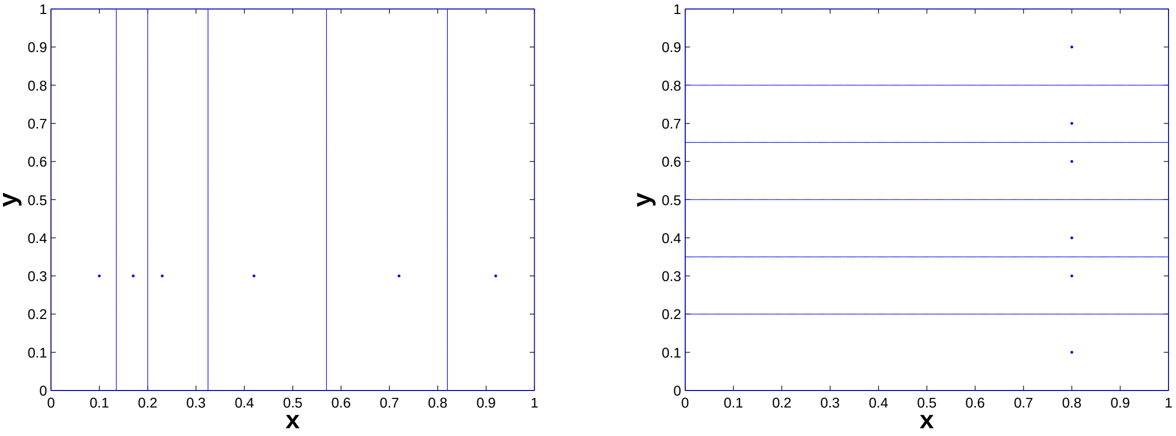

(a) (b)

Figure 5.3: (a) Voronoi diagram with seeds of the form (x_i, y) for $i = 1, \ldots, 6$ and $y = 0.3$. Here $x_i = 0.1, 0.17, 0.23, 0.42, 0.72, 0.92$. (b) Voronoi diagram with seeds of the form (x, y_i) for $i = 1, \ldots, 6$ and $x = 0.8$. Here $y_i = 0.1, 0.3, 0.4, 0.6, 0.7, 0.9$.

assume $\Omega = [0,1] \times [0,1]$ with seeds described by $(\frac{i}{10}, 0.3)$, where $i = 1, \ldots, 9$. This set of seeds forms perfectly vertical columnar grains. Now displace the leftmost seed downwards a distance of $\epsilon = 0.06$, the next seed is displaced upwardly by the same distance ϵ and so on. The resulting Voronoi diagram is shown in Fig. 5.4a. These grains have a perfectly columnar structure at the top and peaked structure at the bottom. To obtain V-shaped grains similar to the ones shown in Fig. 5.1, we add vertical displacements of different magnitudes over all seeds, but still, consecutive seeds must be displaced in opposite directions. For example, if we displace all seeds with random numbers of the form

$$(x_i, y_i) = (\frac{i}{10}, 0.3 + \text{rand}(i)\ (-1)^i\ \epsilon),$$

where $0 \leq \text{rand}(i) \leq 1$ is a random number that distributes uniformly, then Voronoi diagrams like the one shown in Fig. 5.4b are generated. These diagrams tend to be geometrically more consistent with the V-shaped grain morphology shown in Fig. 5.1.

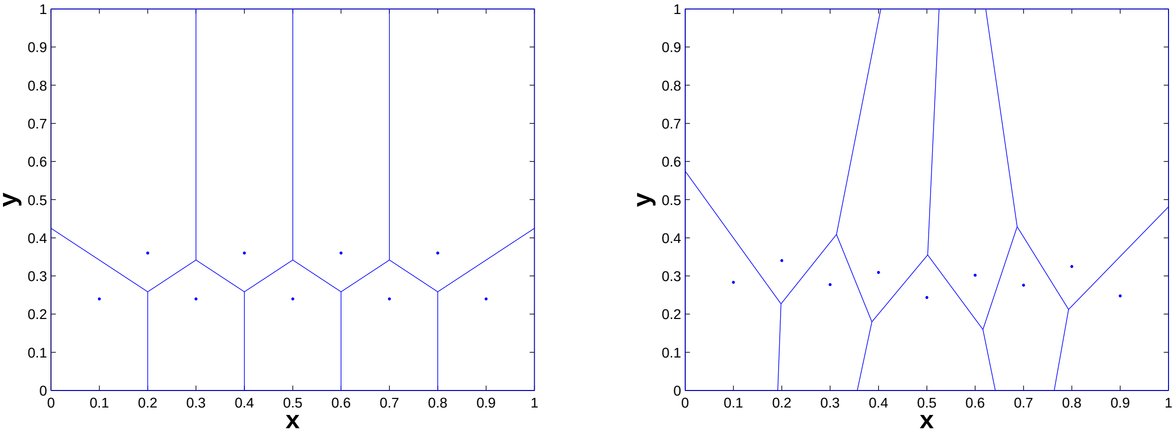

(a) (b)

Figure 5.4: (a) Voronoi diagram with seeds of the form $(\frac{i}{10}, 0.3 + \epsilon(-1)^i)$, where $i = 1, \ldots, 9$. (b) Voronoi diagram with seeds of the form $(\frac{i}{10}, 0.3 + \text{rand}(i)\ \epsilon\ (-1)^i)$, where $i = 1, \ldots, 9$. Here $y_i = 0.1, 0.3, 0.4, 0.6, 0.7, 0.9$.

5.3 A perfectly columnar microstructure with in-plane grain sizes distributing log-normally

First we start with a brief description of a log-normal distribution and some of its properties. A log-normal distribution is defined as a continuous probability distribution function of a random variable whose logarithm is normally distributed. This means that if the random variable X distributes log-normally then $Z = \log X$ distributes normally. It follows that if Z is a random variable that distributes normally then $X = e^Z$ distributes log-normally.

The above definition of a log-normal distribution and its relationship with normal distributions implies that there is a one to one correspondence between normal and log-normal distributions. As a consequence, the mean and variance of a log-normal distribution are expressed in terms of the mean and variance of its associated normal distribution.

The statement: "*The random variable X distributes normally with mean μ and variance σ^2*" is usually represented symbolically as $X \sim N(\mu, \sigma^2)$. The symbol "$\sim$" means "*distributes like*" and N indicates the random variable X distributes normally.

It is known from the literature that if $X \sim N(\mu, \sigma^2)$, then $Z = e^X$ has mean $e^{\mu+\sigma^2/2}$ and variance $(e^{\sigma^2} - 1)e^{2\mu+\sigma^2}$. Despite the differences between the mean and variances of a normal and a log-normal distribution, generally a log-normal distribution is represented by

$$X \sim \text{Log-N}\left(\mu, \sigma^2\right),$$

instead of $X \sim \text{Log-N}\left(e^{\mu+\sigma^2/2}, (e^{\sigma^2} - 1)e^{2\mu+\sigma^2}\right)$. The PDF of a log-normal distribution is given by

$$f(x, \mu, \sigma) = \frac{1}{x\sqrt{2\pi\sigma^2}} e^{-\frac{(\log x - \mu)^2}{2\sigma^2}}, \quad x > 0,$$

where σ^2 and μ are the variance and mean of the associated normal distribution. The following properties of log-normal distributions are well known:

1. If $X_i \sim \text{Log-N}\,(\mu_i, \sigma_i^2)$, for $i = 1, \ldots, n$, are independent log-normally distributed variables then $Z = \prod_{i=1}^n X_i$ satisfies

$$Z \sim \text{Log-N}\left(\sum_{i=1}^n \mu_i, \sum_{i=1}^n \sigma_i^2\right). \tag{5.1}$$

2. Let $\alpha > 0$ and $X \sim \text{Log-N}\,(\mu, \sigma^2)$ then $Z = \alpha X$ satisfies

$$Z \sim \text{Log-N}\left(\mu + \log\alpha, \sigma^2\right). \tag{5.2}$$

3. Let $\alpha \neq 0$ and $X \sim \text{Log-N}\,(\mu, \sigma^2)$ then $Z = X^\alpha$ satisfies

$$Z \sim \text{Log-N}\left(\alpha\mu, \alpha^2\sigma^2\right). \tag{5.3}$$

4. If $X_i \sim \text{Log-N}\,(\mu_i, \sigma_i^2)$, for $i = 1, 2$ then $Z = X_1 + X_2$ **does not distribute log-normally in general**, but it can be approximated by another log-normal distribution $Z^{'}$ with mean μ and variance σ^2

$$\sigma^2 = \log\left[\frac{\sum(e^{\sigma_i^2} - 1)e^{2\mu_i + \sigma_i^2}}{\left(\sum e^{\mu_i + \sigma_i^2/2}\right)^2} + 1\right], \tag{5.4}$$

$$\mu = \log\left[\sum e^{\mu_i + \sigma_i^2/2}\right] - \frac{\sigma^2}{2}. \tag{5.5}$$

We are now ready to formulate an algorithm whose input is a mean μ, a variance σ^2 and a number of grains N_g. The output is a Voronoi microstructure of N_g perfect columnar grains with the property that its in-plane grain sizes distribute log-normally with mean μ and variance σ^2.

In this work we measure the in-plane grain size of a crystal as the diameter of the circle whose area is identical to the total transverse area of the crystal. Mathematically, let A_g denote the total area of any transverse section of a crystal, then its in-plane grain size d is defined as $d = \sqrt{\frac{4A_g}{\pi}}$.

Since the output of the algorithm is a perfectly columnar microstructure with in-plane grain sizes distributing log-normally, the main idea for generating such a microstructure consists in distributing seeds along a plane in such a way that the Voronoi in-plane cells form perfect rectangles. The seeds contained in the plane are the result of the Cartesian product of two sets of seeds that distribute log-normally. Each set of seeds is contained in a segment.

Knowing that the seeds contained in the segments distribute log-normally, we can show the areas of the resulting rectangles distribute approximately log-normally. Consequently the in-plane grain sizes distribute approximately log-normally. The justification of this conclusion is based on the above properties of log-normal distributions.

Let $X_g = \{g_1^x, \ldots, g_N^x\}$ and $Y_g = \{g_1^y, \ldots, g_N^y\}$ be two sets of positive real numbers both distributing log-normally with mean μ_{1d}^0 and variance $\left(\sigma_{1d}^0\right)^2$. Distribute $N-1$ seeds along the interval $[0, (g_1^x + g_N^x)/2 + \sum_{j=2}^{N-1} g_j^x]$ contained in the x-axis so that the abscissas x_i, for $i = 1, \ldots, N-1$ satisfy:

$$\begin{aligned} x_1 &= \frac{g_1^x}{2}, \\ x_2 &= x_1 + g_2^x, \\ x_3 &= x_2 + g_3^x, \\ &\vdots \\ x_{N-1} &= x_{N-2} + g_{N-1}^x, \end{aligned} \tag{5.6}$$

Similarly distribute $N-1$ seeds along the interval $[0, (g_1^y+g_N^y)/2+\sum_{j=2}^{N-1} g_j^y]$ contained in the y-axis so that the ordinates y_i satisfy:

$$\begin{aligned} y_1 &= \frac{g_1^y}{2}, \\ y_2 &= y_1 + g_2^y, \\ y_3 &= y_2 + g_3^y, \\ &\vdots \\ y_{N-1} &= y_{N-2} + g_{N-1}^y. \end{aligned} \tag{5.7}$$

The Cartesian product of both set of seeds is a non regular Cartesian grid contained in the rectangle $[0, (g_1^x+g_N^x)/2+\sum_{j=2}^{N-1} g_j^x] \times [0, (g_1^y+g_N^y)/2+\sum_{j=2}^{N-1} g_j^y]$. The Voronoi diagram of the resulting Cartesian grid is a set of $(N-1)^2$ rectangles of bases $\frac{g_i^x+g_{i+1}^x}{2}$ and heights $\frac{g_j^y+g_{j+1}^y}{2}$, where $i, j = 1, \ldots, N-1$. Fig. 5.5 shows an example with $\mu_{1d}^0 = 3.59$, $\sigma_{1d}^0 = 0.48$ and $N = 7$.

The areas of these rectangles distribute approximately log-normally. By hypothesis the data $\{g_i^x\}$ and $\{g_j^y\}$ are independent and come from a log-normal distribution with mean μ_{1d}^0 and variance $\left(\sigma_{1d}^0\right)^2$. Then, by (5.2) we have that the data $\{g_i^x/2\}$ and

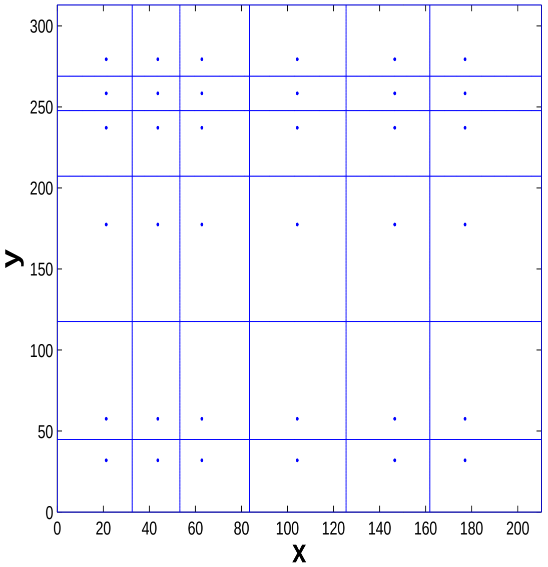

Figure 5.5: Cross section of perfect columnar grains with in-plane grain sizes distributing log-normally. This case has $\mu_{1d}^0 = 3.59$, $\sigma_{1d}^0 = 0.48$ and $N = 7$. There is a total of 36 grains.

$\{g_j^y/2\}$ are independent, log-normal with mean and variance

$$\begin{aligned} \mu_{1d} &= \mu_{1d}^0 - \log 2, \\ \sigma_{1d}^2 &= \left(\sigma_{1d}^0\right)^2. \end{aligned}$$

The bases $b_i = \frac{g_i^x + g_{i+1}^x}{2}$ and heights $h_j = \frac{g_j^y + g_{j+1}^y}{2}$ do not distribute log-normally and even worse, the data $\{b_i\}$ and $\{h_j\}$ are not independent anymore. We can still approximate the mean μ_{sum} and variance σ_{sum}^2 of a log-normal distribution that generates the data $\{b_i\}$ and $\{h_j\}$, indeed, we can apply equations (5.4) and (5.5).

The resultant approximate mean μ_{sum} and variance σ_{sum}^2 are:

$$\begin{aligned} \sigma_{sum}^2 &= \log\left(\frac{e^{\sigma_{1d}^2} + 1}{2}\right), \\ \mu_{sum} &= \mu_{1d} + \frac{\sigma_{1d}^2 - \sigma_{sum}^2}{2}. \end{aligned}$$

Then because of (5.1), the areas $A_{ij} = b_i h_j$ distribute approximately log-normally with mean μ_{prod} and variance σ^2_{prod}

$$\begin{aligned} \mu_{prod} &= 2\mu_{sum}, \\ \sigma^2_{prod} &= 2\sigma_{sum}. \end{aligned}$$

The in-plane grain sizes D_{ij} satisfy $D^2_{ij} = \frac{4}{\pi} A_{ij}$ and the areas $\{A_{ij}\}$ distribute approximately log-normally, so from (5.2) we have that D^2_{ij} distributes approximately log-normally with mean μ_{d^2} and variance $\sigma^2_{d^2}$

$$\begin{aligned} \mu_{d^2} &= \mu_{prod} + \log\left(\frac{4}{\pi}\right), \\ \sigma^2_{d^2} &= \sigma^2_{prod}. \end{aligned}$$

Finally because of (5.3) we have that the in-plane grain sizes distribute approximately log-normally with mean μ_{2d} and variance σ^2_{2d}

$$\begin{aligned} \mu_{2d} &= \frac{1}{2}\mu_{d^2}, \\ \sigma^2_{2d} &= \frac{1}{4}\sigma^2_{d^2}. \end{aligned}$$

The above construction of the distribution of in-plane grain sizes assumes the inputs μ^0_{1d} and $\left(\sigma^0_{1d}\right)^2$ are known. The goal is to generate an output of in-plane grain sizes distributing log-normally with prescribed mean μ_{2d} and variance σ^2_{2d} coming from experimental data.

Fortunately given μ_{2d} and σ^2_{2d} we can determine analytically an expression for μ^0_{1d} and $\left(\sigma^0_{1d}\right)^2$ in terms of μ_{2d} and σ^2_{2d}, indeed, if we solve the above equations from bottom to top we obtain

$$\begin{aligned} \left(\sigma^0_{1d}\right)^2 &= \log\left(2e^{2\sigma^2_{2d}} - 1\right), && (5.8) \\ \mu^0_{1d} &= \mu_{2d} - \frac{1}{2}\log\left(\frac{4}{\pi}\right) + \sigma^2_{2d} - \frac{1}{2}\left(\sigma^0_{1d}\right)^2 + \log 2. && (5.9) \end{aligned}$$

The above discussion is summarized in the following algorithm:

***Input*:**

- *The mean μ_{2d} and variance σ_{2d}^2 of the in-plane grain size distribution of the microstructure. It is assumed that the in-plane grain size distributes log-normally.*
- *The number of seeds $N_x - 1$ along the x-axis and the number of seeds $N_y - 1$ along the y-axis. This determines the total number of grains $N_g = (N_x - 1)(N_y - 1)$.*
- *The film thickness $h > 0$. In our case the thickness h is taken to be much smaller than the length and width. The length and width are determined below.*

***Output*:**

- *A perfect columnar microstructure with in-plane grain sizes that distribute log-normally.*

***Steps*:**

1. *Compute the mean μ_{1d}^0 and variance $\left(\sigma_{1d}^0\right)^2$ using equations (5.9) and (5.8) respectively.*
2. Generate two sets of real numbers $X_g = \{g_1^x, \ldots, g_{N_x}^x\}$ and $Y_g = \{g_1^y, \ldots, g_{N_y}^y\}$, where $g_i^x > 0$ and $g_j^y > 0$ for $i = 1, \ldots, N_x$ and $j = 1, \ldots, N_y$. Each set comes from a log-normal distribution of mean μ_{1d}^0 and variance $\left(\sigma_{1d}^0\right)^2$.

3. Set the dimensions of the microstructure as

$$\begin{aligned} L &= \frac{g_1^x + g_{N_x}^x}{2} + \sum_{i=1}^{N_x-1} g_i^x, \\ W &= \frac{g_1^y + g_{N_y}^y}{2} + \sum_{j=1}^{N_y-1} g_j^y, \\ H &= h, \end{aligned}$$

   where L, W and H are the length along the x-axis, width along the y-axis and heigth along the z-axis respectively.

4. Generate $(N_x-1)(N_y-1)$ seeds with coordinates (x_i, y_j, z_0), where the x_i satisfy the formula (5.6) and the y_j satisfy (5.7). This time we let $1 \leq i \leq N_x - 1$ and $1 \leq j \leq N_y - 1$ instead of ranging i and j in the same set of subindices, say $\{1, \ldots, N-1\}$. The applicate z_0 is constant and is chosen to satisfy $0 < z_0 < h$.

5. Apply the Voronoi tessellation algorithm to the domain

$$\Omega = [0, L] \times [0, W] \times [0, H],$$

   which contains the seeds (x_i, y_j, z_0) described in the previous step. By construction the result will be the desired perfect columnar microstructure with in-plane grain sizes that distribute log-normally with mean μ_{2d} and variance σ_{2d}^2.

The microstructure generated by the above algorithm has the property that the log-normal in-plane grain size distribution is independent of the film height $0 < z < h$. The real microstructure has an in-plane grain size distribution that depends on the film thickness z. One way to capture this additional feature is by applying the above algorithm to the microstructure at different height levels z. For example, we know from Fig. 5.2 that at $z_1 = 75nm$ and $z_2 = 365nm$ the log-normal distributions have means $\mu_1 = 3.35$, $\mu_2 = 3.59$ and variances $\sigma_1 = 0.34$, $\sigma_2 = 0.48$ respectively. With no difficulty we can apply the algorithm at $z = z_1$ and $z = z_2$. The resulting configuration will have perfect columnar grains with in-plane grain sizes distributing as in Fig. 5.2. The first two film heights, $z = z_1$ and $z = z_2$, can be modeled with perfect columnar grains because from Table 5.1 we have that grains are equiaxed. At the height $z_5 = 1680nm$ the grain morphology is also almost columnar, see Fig. 5.1. Therefore we can still model the film thickness at $z = z_5$ with perfectly columnar grains.

The main challenge is to model the remaining V-shaped grains at $z_3 = 890nm$ and $z_4 = 1250nm$. We know from Fig. 5.2 that the log-normal distributions have means $\mu_3 = 3.57$, $\mu_4 = 3.73$ and variances $\sigma_1 = 0.47$, $\sigma_2 = 0.56$ respectively. We apply the algorithm like we did with the other layers and the log-normal distributions are generated. Now the problem is how to capture the V-shaped grain morphology without destroying the log-normal distributions. In section 5.2 it is shown that almost V-shaped columnar microstructures can be obtained from perfect columnar grained microstructures by adding an out of plane perturbation[1] to the seeds living in perfect columnar grains. In our case the perturbed seeds at layers $z = z_3$ and z_4 change only in their third compoment like

$$\begin{aligned} z_3^* &= z_3 + \mathrm{rand}(i,j)\ \epsilon, \\ z_3^* &= z_3 + \mathrm{rand}(i,j)\ \epsilon, \end{aligned}$$

where $\epsilon > 0$ is the perturbation amplitude, $\mathrm{rand}(i,j)$ is a real number that distributes uniformly in $[-1,1]$ and i, j are the indices of the x and y components of the seeds belonging to layer $z = z_3$ or $z = z_4$. If we make $\epsilon = 0.2$, $N_x = N_y = 35$ then

---

[1] Also an in-plane perturbation is added with the purpose of destroying the perfect rectangular in-plane grain shapes. This is done by perturbing the Voronoi seeds of each rectangle of dimensions b_i, h_j. We decided to perturb each seed along two independent directions. Along x by 10% of the base b_i and along y by 10% of the height h_j uniformly randomly. The 10% is an empirical factor, we noticed that higher perturbations destroyed the grain-size log-normal distribution.

we obtain a microstructure of dimensions $L = 1153.72nm$, $W = 1790.46nm$. The log-normal distributions at $z = z_3$ and $z = z_4$ are shown in Fig. 5.6a and Fig. 5.6b respectively. We can see that both distributions look identical to the ones shown in Fig. 5.2.

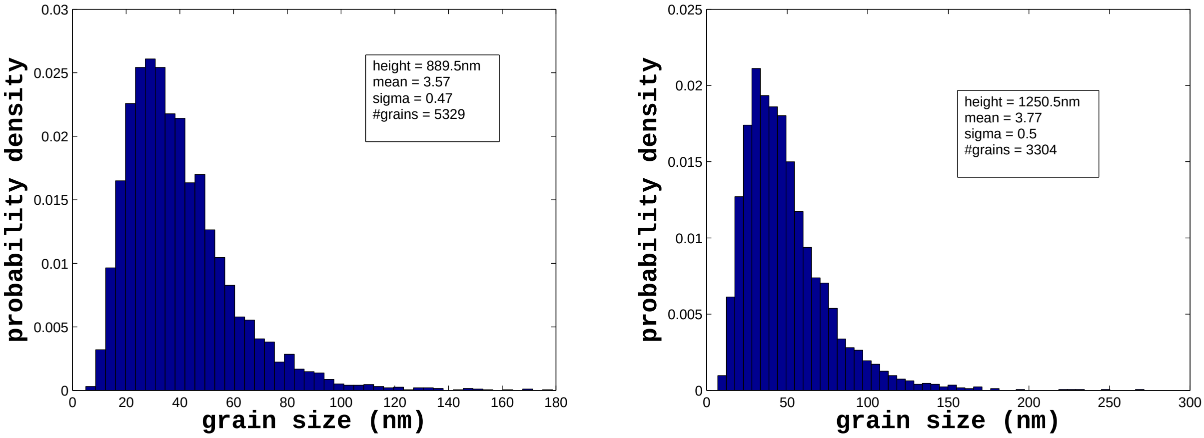

(a) (b)

Figure 5.6: (a) Log-normal grain size distribution at $z = z_3$. (b) Log-normal grain size distribution at $z = z_4$.

The transverse grain morphology is shown in Fig. 5.7. The main disadvantage of this method is that the Voronoi microstructures, like the one shown in Fig. 5.7, do not correspond to real microstructures.

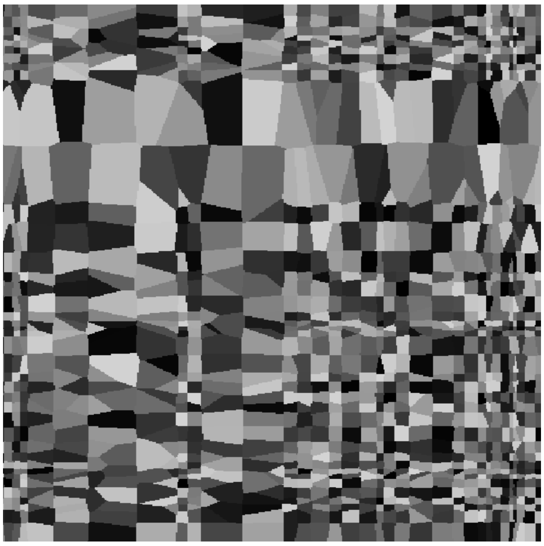

Figure 5.7: Microstructure geometry at $z = z_3$.

Chapter 6

Crystal Plasticity Constitutive Modeling

6.1 Description of the Problem

In Section 2.4 it was mentioned that the conservation laws of angular and linear momentum are not sufficient to describe the mechanical behaviour of a solid body, unless the stress $\boldsymbol{\sigma}$ is known, but usually this is not the case. Thus, a complementary set of equations is required in order to complete the governing set of equations. This complementary set of equations is known as constitutive equations and they can be derived from physical principles or from purely mathematical relations that try to fit experimental data. In this thesis we study exclusively the latter phenomenological models.

In Section 2.5 it was mentioned that most metals, in particular Ni, exhibit the stress-strain relationship shown in Fig. 2.13. The linear elastic zone is modeled with Hooke's law (2.5) but the plasticity region is more complicated to deal with. The main reason is because the physical mechanisms that cause plastic deformation can vary widely, consequently the mathematical models are many. In this chapter we are interested in modeling the plasticity of polycrystalline materials. It has been observed experimentally that plasticity in polycrystalline metals is produced from crystal dislocations.

6.2 Crystal Plasticity Theory

In Section 2.1 we defined a crystal as a three dimensional periodic arrangement of atoms, ions or molecules. The atoms or molecules are located at points of a regular lattice. There are fourteen types of lattices known as Bravais lattices. From all lattice types we are interested only in the FCC structure because Ni is of this type. Figure 2.7a shows the crystal structure of Ni, where a single Ni atom is located at each lattice point.

The concept of a perfect crystal is an idealization. In nature these tend to have some "defects" [22]; that is, the lattice is not regular anymore. The most common type of defects are the point, line, surface and volume defect. We are interested only in line defects. These are known as dislocations and are important in the study of plasticity of crystals.

Dislocations are classified into edge dislocations, screw dislocations or a combination of both [21]. Figure 6.1 shows an example of an edge dislocation. The perfect lattice, which consists of blue points, has an extra layer of atoms or molecules (shown in red) of the same type.

Dislocations in a crystal lattice can be created permanently by applying external forces which exceed a critical value known as the critical resolved shear stress. This process is illustrated in Figure 6.2. Assume a crystal lattice is exposed under the action of a set of increasing external forces like in Figure 6.2a. A dislocation is

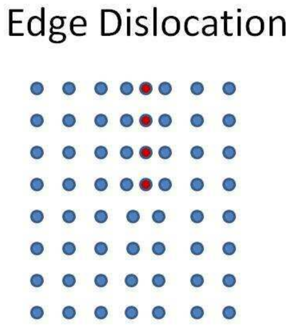

Figure 6.1: The extra layer of red atoms is an example of an edge dislocation.

created once the external forces deform the lattice like in Figure 6.2b. Here the crystal remains elastic, this means that if the external forces are removed then the dislocation moves to the left leaving the lattice like in Figure 6.2a. If the external forces keep increasing in magnitude, but still smaller than the critical value, then a configuration like Figure 6.2c is achieved. Note how the dislocation is moving to the right boundary of the crystal, but again, once the external forces are removed this dislocation moves to the left until it leaves the lattice like in Figure 6.2a. Finally, once the external forces reach the critical resolved shear stress then the dislocation must have moved to the right boundary of the crystal, leaving a permanent deformation. This means that if the external forces are removed, then the dislocation does not move to the left anymore. The distance between this dislocation and the perfect lattice is known as the magnitude of Burger's vector. Usually this number is of the order of angstroms. We do not define Burger's vector in this thesis because only its magnitude is relevant to us. For more details on Burger's vector and dislocations see

[21].

(a) (b) (c) (d)

Figure 6.2: (a) Perfect cystal lattice. (b) Crystal lattice deformed under the action of external forces. An edge dislocation has been created at the left side of the lattice, but the crystal remains elastic. (c) The previous configuration under the action of higher external forces. Note how the edge dislocation is moving to the right as the external forces increase, but still the crystal remains elastic. (d) Plastic deformation of the crystal. Now the dislocation is at the boundary of the crystal lattice at a distance of Burger's vector length.

Experimentation has shown that plastic deformation of crystals[1] is a result of relative motion (or slip) on specific crystallographic planes in response to shear stress along the planes. It has been observed that slip planes correspond to planes of closest packing. The main reason for this is that parallel planes of closest packing have the greatest separation and therefore the slip between them is easiest, indeed, interatomic forces decrease rapidly with interatomic distance [37].

Slip occurs in a preferred set of directions for a given slip plane, these directions are called slip directions. A slip plane and a slip direction together form what is called a slip system. Figure 6.3 illustrates 3 slip systems of a FCC crystal, say, $(\boldsymbol{n}_i, \boldsymbol{s}_j)$, where $j = 1, 2, 3$. Note that the plane shown in Figure 6.3 is crystallographically equivalent to three more crystallographic planes. Therefore all FCC crystals have 12 different slip systems [37].

---

[1] The movement of dislocations to crystal boundaries.

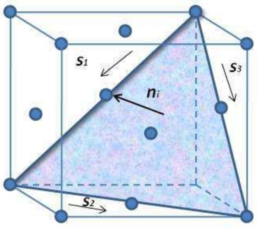

Figure 6.3: Three slip systems in a FCC crystal.

Multisurface Plasticity

In this section we give an introduction to the set of constitutive equations that arise in single crystal plasticity. The exposition of the constitutive equations is based on [56].

We assume the total strain $\boldsymbol{\varepsilon}$ at every point of the crystal admits the additive decomposition

$$\boldsymbol{\varepsilon} = \boldsymbol{\varepsilon}^e + \boldsymbol{\varepsilon}^p, \tag{6.1}$$

where $\boldsymbol{\varepsilon}^e$ is the elastic strain and $\boldsymbol{\varepsilon}^p$ is the plastic strain. The elastic strain is governed by Hooke's law (2.5),

$$\boldsymbol{\sigma} = \mathbb{C} : (\boldsymbol{\varepsilon} - \boldsymbol{\varepsilon}^p)\,.$$

The interpretation of $\boldsymbol{\varepsilon}^p$ is that when the total stress $\boldsymbol{\sigma}$ is reduced to zero, then a permanent deformation $\boldsymbol{\varepsilon}^p$ is left at every point of the crystal[2]. It is important to

---

[2] This follows from Hooke's law, indeed, given that the elastic strain $\boldsymbol{\varepsilon}^e = \boldsymbol{\varepsilon} - \boldsymbol{\varepsilon}^p$ satisfies

mention that the additive decomposition (6.1) is valid only for small deformations [56].

The new variable $\boldsymbol{\varepsilon}^p$, which is associated to plastic deformation, requires a constitutive equation. Also a limit must be imposed on the elastic region of the crystal because we are assuming the existence of a critical stress that leads to plastic deformation $\boldsymbol{\varepsilon}^p$. Therefore, following [56], we assume the elastic domain $\mathbb{E}_\sigma$ of the crystal to be described mathematically as follows:

$$\mathbb{E}_\sigma = \{(\boldsymbol{\sigma}, \boldsymbol{q}) \in \mathbb{SYM} \times \mathbb{R}^m | f_i(\boldsymbol{\sigma}, \boldsymbol{q}) \leq 0,\ i = 1, 2, \ldots, N\},$$

where f_i are $N \geq 1$ functions that intersect possibly nonsmoothly, $\boldsymbol{q}$ is a set of hardening parameters and $\mathbb{SYM}$ denotes the set of all symmetric second order tensors. The functions f_i are known as yield functions and each f_i corresponds to a slip system. In the next section we give explicit forms of these functions. The boundary and the interior of $\mathbb{E}_\sigma$ are denoted as $\partial\mathbb{E}_\sigma$ and $\mathring{\mathbb{E}}_\sigma$ respectively, and are defined in the topological sense. The boundary $\partial\mathbb{E}_\sigma$ is known as the yield surface of the crystal and it is piecewise smooth.

We assume the plastic strain evolves with time as follows

$$\dot{\boldsymbol{\varepsilon}}^p = \sum_{i=1}^{N} \dot{\gamma}_i \frac{\partial f_i(\boldsymbol{\sigma}, \boldsymbol{q})}{\partial \boldsymbol{\sigma}}, \tag{6.2}$$

where $\dot{\gamma}_i \geq 0$ are consistency parameters that satisfy the Kuhn-Tucker complementarity conditions

$$\dot{\gamma}_i \geq 0,\ f_i(\boldsymbol{\sigma}, \boldsymbol{q}) \leq 0, \quad \text{and } \dot{\gamma}_i f_i(\boldsymbol{\sigma}, \boldsymbol{q}) = 0.$$

Also the following consistency conditions are satisfied

$$\dot{\gamma}_i \dot{f}_i(\boldsymbol{\sigma}, \boldsymbol{q}) = 0.$$

$\boldsymbol{\sigma} = \mathbb{C} : (\boldsymbol{\varepsilon} - \boldsymbol{\varepsilon}^p)$, then $\boldsymbol{\sigma} = \mathbf{0}$ and the invertibility of $\mathbb{C}$ imply $\boldsymbol{\varepsilon} = \boldsymbol{\varepsilon}^p$.

Finally a set of internal variables $\boldsymbol{\alpha}$ satisty the following evolution equations [56]

$$\dot{\boldsymbol{\alpha}} = \sum_{i=1}^{N} \dot{\gamma}_i \frac{\partial f_i(\boldsymbol{\sigma}, \boldsymbol{q})}{\partial \boldsymbol{q}}. \tag{6.3}$$

Note that the plastic strain (6.2) and the internal variables (6.3) are obtained directly from the yield functions $\{f_i\}_{i=1}^{N}$ by taking the partial derivatives with respect to $\boldsymbol{\sigma}$ and $\boldsymbol{q}$, respectively. Models of this type are known as associative and have the mathematical advantage that once the yield functions $\{f_i\}_{i=1}^{N}$ are known, the evolution equations of the plastic strain and the internal variables are automatically derived. Also, associative constitutive models automatically satisfy the second law of thermodynamics.

6.3 A Crystal Plasticity Model

Here we consider the elastic-plastic response of a single crystal submitted to a general three dimensional loading. We present the model described in [63] and point out that the model is a particular case of the general model given in the previous section. Next, a numerical algorithm is presented followed by some numerical results.

In Section 6.2 it was mentioned that plasticity of a single crystal occurs by the slip of crystallographic planes on a set of preferred slip directions. This phenomena is described in terms of a set of yield functions f_i, $i = 1, \ldots, N$, where N is the number of slip systems and in terms of a set of consistency parameters γ_i.

Let $\boldsymbol{n}_i$ be the unit normal to the *ith* slip plane and $\boldsymbol{s}_i$ be a unit vector along the slip direction (see figure 6.3). Then the plastic strain rate in the crystal is defined to be

$$\dot{\boldsymbol{\varepsilon}}^p = \sum_{i=1}^{N} \dot{\gamma}_i \; sgn(\tau_i) \; \boldsymbol{m}_i,$$

where $\dot{\gamma}_i \geq 0$ is the plastic slip on the ith slip system. The tensor $\boldsymbol{m}_i$,

$$\boldsymbol{m}_i \;\; = \;\; \frac{1}{2}(\boldsymbol{n}_i \otimes \boldsymbol{s}_i + \boldsymbol{s}_i \otimes \boldsymbol{n}_i)$$

is the Schmidt tensor and $\tau_i = \boldsymbol{\sigma} : \boldsymbol{m}_i$ is the resolved shear stress on slip system i. The yield condition in slip system i is given by Schmid's law:

$$f_i(\boldsymbol{\sigma}, \boldsymbol{\gamma}) = |\tau_i| - \tau_i^c(\boldsymbol{\gamma}) = 0, \tag{6.4}$$

where $\boldsymbol{\gamma} = (\gamma_1, \ldots, \gamma_N)$ and $\tau_i^c(\boldsymbol{\gamma})$ is the critical resolved shear stress (CRSS) in slip system i, the CRSS evolves in time in the following way

$$\dot{\tau_i}^c = \sum_{j=1}^{N} h_{ij} \; \dot{\gamma}_j. \tag{6.5}$$

The initial condition $\tau_i(0) = \tau_{c0}$ is assumed to be known and is assumed identical in all slip systems (τ_{c0} is a material constant). The hardening rates h_{ij} are assumed to satisfy

$$h_{ij} = q_{ij} h_j, \tag{6.6}$$

where q_{ij} is one if the slip systems i and j are coplanar and $q_{ij} > 1$ otherwise. An example of the hardening rate h_j is

$$h_j(\tau_j^c) = h_0\{1 - \frac{\tau_j^c}{\tau_s^c}\}^a,$$

where h_0, τ_s^c and a are hardening parameters of the crystal taken to be identical for all slip systems. It can be shown that the model described is associative; indeed,

$$\dot{\boldsymbol{\varepsilon}}^p = \sum_{i=1}^{N} \dot{\gamma}_i \, \frac{\partial f_i(\boldsymbol{\sigma}, \gamma)}{\partial \boldsymbol{\sigma}}.$$

Now we present an algorithm that solves the above model numerically:

1. Let $\dot{\boldsymbol{\varepsilon}}$ be a given loading. Assume at time $t = t_n$ we know $\gamma_i(t_n)$, $\boldsymbol{\varepsilon}_n^p$ and $\tau_i^c(t_n)$ for $i = 1, \ldots, N$. Let Δt_n be a time increment, then the total strain increment is $\Delta\boldsymbol{\varepsilon}_n = \dot{\boldsymbol{\varepsilon}}\Delta t_n$. At time $t_{n+1} = t_n + \Delta t_n$ the total strain is $\boldsymbol{\varepsilon}_{n+1} = \boldsymbol{\varepsilon}_n + \Delta\boldsymbol{\varepsilon}_n$. For the given total strain $\boldsymbol{\varepsilon}_{n+1}$ it's assumed the material remains elastic[3].

2. Elastic behaviour implies

$$\boldsymbol{\varepsilon}_{n+1}^p = \boldsymbol{\varepsilon}_n^p, \ \gamma_i(t_{n+1}) = \gamma_i(t_n) \text{ and } \tau_i^c(t_{n+1}) = \tau_i^c(t_n),$$

   for $i = 1, \ldots, N$. Let $\boldsymbol{\varepsilon}_{n+1}^{e(\text{trial})} = \boldsymbol{\varepsilon}_{n+1} - \boldsymbol{\varepsilon}_{n+1}^p$ be a trial elastic strain, then the corresponding trial stress at time $t = t_{n+1}$ is computed with Hooke's law $\boldsymbol{\sigma}^{\text{trial}}(t_{n+1}) = \mathbb{C} : \boldsymbol{\varepsilon}_{n+1}^{e(\text{trial})}$.

3. The set of yield functions $\left\{f_i(\boldsymbol{\sigma}_{n+1}^{\text{trial}}, \boldsymbol{\gamma}(t_{n+1}))\right\}_{i=1}^{N}$ is evaluated, if $f_i < 0$ for all i then we are done. The assumption of having an elastic state is correct. Go back to step 1 and take another time increment Δt_{n+1}.

---

[3] This assumption is part of the numerical algorithm. Further tests will determine the correct state of the material.

4. If there exists i such that $f_i(\boldsymbol{\sigma}^{\text{trial}}(t_{n+1}), \boldsymbol{\gamma}(t_{n+1})) > 0$ then plasticity has been reached and the assumption of having elasticity is incorrect. A correction to $\gamma_i(t_{n+1})$ and $\tau_i^c(t_{n+1})$ must be done.

5. Let I be any index such that

$$f_I(\boldsymbol{\sigma}^{\text{trial}}(t_{n+1}), \boldsymbol{\gamma}(t_{n+1})) = \max_{1 \leq i \leq N} \{f_i(\boldsymbol{\sigma}^{\text{trial}}(t_{n+1}), \boldsymbol{\gamma}(t_{n+1})) > 0\}.$$

Assume for the moment plasticity occurs only in system I; that is,

$$\begin{aligned} \gamma_i(t_{n+1}) &= \gamma_i(t_n), \\ \tau_i^c(t_{n+1}) &= \tau_i^c(t_n), \end{aligned}$$

for $i \neq I$. The goal is to make $f_I(\boldsymbol{\sigma}^{\text{trial}}(t_{n+1}), \boldsymbol{\gamma}(t_{n+1})) < tol$, for some tolerance $tol > 0$.

One way to do this is with the secant method:

Define

$$g(\boldsymbol{\sigma}, x) = f_I(\boldsymbol{\sigma}, \gamma_1(t_n), \ldots, \gamma_{I-1}(t_n), x, \gamma_{I+1}(t_n), \ldots, \gamma_N(t_n)),$$

we want to compute x so that $g(\boldsymbol{\sigma}, x) = 0$[4]. Let

$$\{\gamma_{I,k}(t_{n+1})\}_{k=0}^{N_{max}},$$

be a sequence of real numbers that approaches to the state $\gamma_I(t_{n+1})$. Later an explicit form of $\{\gamma_{I,k}(t_{n+1})\}_{k=0}^{N_{max}}$ is shown. The positive integer N_{max} represents the maximum number of secant iterations.

Define $\gamma_{I,0}(t_{n+1}) = \gamma_I(t_n)$, $\boldsymbol{\sigma}_1^{\text{trial}}(t_{n+1}) = \boldsymbol{\sigma}^{\text{trial}}(t_{n+1})$ and

$$\delta\gamma_{I,k}(t_n) = \gamma_{I,k}(t_{n+1}) - \gamma_{I,k-1}(t_{n+1}).$$

---

[4] Note that $\boldsymbol{\sigma}$ depends on x; that is, the stress depends on the plastic slip. Strictly speaking g depends only on x.

Let $\Delta\gamma_{I,1}(t_n) = \delta\gamma_{I,1}(t_n)$ be a positive "small" real number, 10^{-6} or less for example. We update $\gamma_{I,k}(t_{n+1})$ by decreasing g to zero with the following secant iterations:

$$\begin{aligned}
\Delta_k g &= g(\boldsymbol{\sigma}_k^{\text{trial}}(t_{n+1}), \gamma_{I,k}(t_{n+1})) - g(\boldsymbol{\sigma}_k^{\text{trial}}(t_{n+1}), \gamma_{I,k-1}(t_{n+1})), \\
\delta\gamma_{I,k+1}(t_n) &= -\frac{g(\boldsymbol{\sigma}_k^{\text{trial}}(t_{n+1})), \gamma_{I,k}(t_{n+1}))}{\Delta_k g}\delta\gamma_{I,k}(t_n), \qquad (6.7) \\
\Delta\gamma_{I,k+1}(t_n) &= \Delta\gamma_{I,k}(t_n) + \delta\gamma_{I,k+1}(t_n), \\
\gamma_{I,k+1}(t_{n+1}) &= \gamma_{I,0}(t_{n+1}) + \Delta\gamma_{I,k+1}(t_n).
\end{aligned}$$

After computing $\Delta\gamma_{I,k+1}(t_n)$ the plastic strain suffers the following increment

$$\Delta\boldsymbol{\varepsilon}^p_{n,k} = \Delta\gamma_{I,k+1}(t_n)\ sgn(\tau_I(t_n))\boldsymbol{m}_I, \qquad (6.8)$$

$$\boldsymbol{\varepsilon}^p_{n+1,k} = \boldsymbol{\varepsilon}^p_n + \Delta\boldsymbol{\varepsilon}^p_{n,k}. \qquad (6.9)$$

The new trial stress is computed in the following way

$$\begin{aligned}
\Delta\boldsymbol{\sigma}_{n,k} &= \mathbb{C} : (\Delta\boldsymbol{\varepsilon}_n - \Delta\boldsymbol{\varepsilon}^p_{n,k}), \\
\boldsymbol{\sigma}^{trial}_{k+1}(t_{n+1}) &= \boldsymbol{\sigma}(t_n) + \Delta\boldsymbol{\sigma}_{n,k}.
\end{aligned}$$

Now $\boldsymbol{\tau}^c(t_n)$ is updated. Since we are assuming only slip system I is active, a backward Euler method applied to (6.5) implies

$$\Delta\tau^c_{I,k}(t_n) = h_0\Delta\gamma_{I,k}(t_n)\left(1 - \frac{\tau^c_I(t_n) + \Delta\tau^c_{I,k}(t_n)}{\tau^c_s}\right)^a, \qquad (6.10)$$

the previous equation can be solved for $\Delta\tau^c_{I,k}(t_n)$ with Newton's Method. After $\Delta\tau^c_{I,k}(t_n)$ is computed then make the update

$$\tau^c_I(t_{n+1}) = \tau^c_I(t_n) + \Delta\tau^c_{I,k}(t_n).$$

The yield function at slip system I is reevaluated,

$$f_I \equiv |\boldsymbol{\sigma}^{trial}_{k+1}(t_{n+1}) : \boldsymbol{m}_I| - \tau^c_I(t_{n+1}), \qquad (6.11)$$

> if $f_I \geq tol$ then go back to the set of equations (6.7) of secant's method until (6.11) satisfies $f_I < tol$. If (6.11) satisfies $f_I < tol$ then we are done with slip system I. Make the updates
>
> $$\begin{aligned} \Delta\tau^c_{i,k}(t_n) &= q_{iI} h_0 \left(1 - \frac{\tau^c_I(t_{n+1})}{\tau^c_s}\right)^a \Delta\gamma_{I,k}(t_n), \\ \tau^c_i(t_{n+1}) &= \tau^c_i(t_n) + \Delta\tau^c_{i,k}(t_n), \end{aligned}$$
>
> and go back to the beginning of step 5 until all slip systems satisfy the condition $f_i < tol$, for $i = 1, \ldots, N$.

In [63] the responses of an FCC copper crystal under shear loading and uniaxial strain loading are studied. We apply the above algorithm to these two cases in the next two sections. The algorithm we propose is different from the algorithm used in [63], but the numerical results obtained with both algorithms are in good agreement.

6.4 Numerical Example for Shear Loading

Consider a copper sample under a cyclic shear loading in the $\boldsymbol{e}_1 - \boldsymbol{e}_2$ plane given by

$$\dot{\boldsymbol{\varepsilon}} = \dot{\varepsilon_{12}} \left(\boldsymbol{e}_1 \otimes \boldsymbol{e}_2 + \boldsymbol{e}_2 \otimes \boldsymbol{e}_1\right).$$

First the strain rate $\dot{\varepsilon_{12}} = 0.1s^{-1}$ is applied until $\varepsilon_{12} = 0.01$, then the strain rate is reversed to $\dot{\varepsilon_{12}} = -0.1s^{-1}$ until $\varepsilon_{12} = 0$. Finally the strain rate is reversed to $\dot{\varepsilon_{12}} = 0.1s^{-1}$ until $\varepsilon_{12} = 0.01$.

The material constants of copper are:

Poisson's Ratio	ν	$\frac{1}{3}$
Young's Modulus	E	$124GPa$
Initial Critical Resolved Shear Stress	τ_{c0}	$16MPa$
Saturated Critical Resolved Shear Stress	τ_s^c	$148MPa$
Hardening Exponent	a	2.25
Hardening Coefficient	h_0	$180MPa$

Finally $q_{ij} = 1$ if slip systems i and j are coplanar and $q_{ij} = 1.4$ otherwise. The Schmidt tensors were computed with the formula $\boldsymbol{m}_i = \frac{1}{2}(\boldsymbol{n}_i \otimes \boldsymbol{s}_i + \boldsymbol{s}_i \otimes \boldsymbol{n}_i)$. The normal vectors and slip directions for copper are given by [63]:

- For $i = 1, 2, 3$:

$$\begin{aligned}\boldsymbol{n}_i &= \frac{1}{\sqrt{3}}\left(\boldsymbol{e}_1 + \boldsymbol{e}_2 + \boldsymbol{e}_3\right),\\ \boldsymbol{s}_1 &= \frac{1}{\sqrt{2}}(\boldsymbol{e}_2 - \boldsymbol{e}_3), \boldsymbol{s}_2 = \frac{1}{\sqrt{2}}(-\boldsymbol{e}_1 + \boldsymbol{e}_2), \boldsymbol{s}_3 = \frac{1}{\sqrt{2}}(-\boldsymbol{e}_1 + \boldsymbol{e}_3).\end{aligned}$$

- For $i = 4, 5, 6$:

$$\begin{aligned}\boldsymbol{n}_i &= \frac{1}{\sqrt{3}}\left(\boldsymbol{e}_1 - \boldsymbol{e}_2 + \boldsymbol{e}_3\right),\\ \boldsymbol{s}_4 &= \frac{1}{\sqrt{2}}(-\boldsymbol{e}_2 - \boldsymbol{e}_3), \boldsymbol{s}_5 = \frac{1}{\sqrt{2}}(\boldsymbol{e}_1 - \boldsymbol{e}_3), \boldsymbol{s}_6 = \frac{1}{\sqrt{2}}(\boldsymbol{e}_1 + \boldsymbol{e}_2).\end{aligned}$$

- For $i = 7, 8, 9$:

$$\begin{aligned}\boldsymbol{n}_i &= \frac{1}{\sqrt{3}}\left(-\boldsymbol{e}_1 + \boldsymbol{e}_2 + \boldsymbol{e}_3\right),\\ \boldsymbol{s}_7 &= \frac{1}{\sqrt{2}}(-\boldsymbol{e}_2 + \boldsymbol{e}_3), \boldsymbol{s}_8 = \frac{1}{\sqrt{2}}(-\boldsymbol{e}_1 - \boldsymbol{e}_3), \boldsymbol{s}_9 = \frac{1}{\sqrt{2}}(-\boldsymbol{e}_1 - \boldsymbol{e}_2).\end{aligned}$$

- For $i = 10, 11, 12$:

$$\begin{aligned}\boldsymbol{n}_i &= \frac{1}{\sqrt{3}}\left(-\boldsymbol{e}_1 - \boldsymbol{e}_2 + \boldsymbol{e}_3\right),\\ \boldsymbol{s}_{10} &= \frac{1}{\sqrt{2}}(\boldsymbol{e}_2 + \boldsymbol{e}_3), \boldsymbol{s}_{11} = \frac{1}{\sqrt{2}}(-\boldsymbol{e}_1 - \boldsymbol{e}_3), \boldsymbol{s}_{12} = \frac{1}{\sqrt{2}}(-\boldsymbol{e}_1 + \boldsymbol{e}_2).\end{aligned}$$

A direct calculation shows

$$\begin{aligned} |\tau_i| &= |\boldsymbol{\sigma} : \boldsymbol{m}_i| = \frac{1}{\sqrt{6}}|\sigma_{12}|, \quad i = 1,3,4,5,7,8,10,11, \\ |\tau_i| &= 0, \quad \text{otherwise.} \end{aligned} \tag{6.12}$$

This means eight slip systems activate initially when $\sigma_{12} = \sqrt{6}\tau_{c0}$.

The numerical algorithm of the previous section was applied with a constant time step of $\Delta t = 2 \times 10^{-3}s$. The initial conditions at time $t = 0$ are $\boldsymbol{\varepsilon}^p(0) = \mathbf{0}$, $\gamma_i(0) = 0$ and $\tau_i^c(0) =$, for $i = 1, ..., 12$. The choice of the index in step 5

$$f_I = \max_{1 \leq i \leq N} \left\{ f_i(\boldsymbol{\sigma}^{\text{trial}}(t_{n+1}), \boldsymbol{\gamma}(t_{n+1})) \right\},$$

was taken to be the minimum of all indices that correspond to maximum positive values of f_i. It's clear that many choices are possible, taking the greatest index is an example. Different index choices lead to different numerical values of $\boldsymbol{\gamma}(t)$. This means $\boldsymbol{\gamma}$ is not unique. Analytical solutions where $\boldsymbol{\gamma}$ is not unique are also available.

Figure 6.4 shows a normalized shear stress-shear strain response. The normalized shear stress $\bar{\sigma}_{12}$ is defined by $\bar{\sigma}_{12} = \frac{1}{\tau_{c0}}\sigma_{12}$. It's clear from Fig. 6.4 that yielding occurs at the expected value $\bar{\sigma}_{12} = \sqrt{6}$. Figure 6.5 shows the relationship between the plastic slips γ_i and the shear strain ε_{12}, for $i = 1, 4$. This is an expected result from (6.12). The horizontal trajectories correspond to elastic behaviour, this is consistent with the theory and Fig. 6.4. Numerically the plastic slips $\{\gamma_2, \gamma_6, \gamma_9, \gamma_{12}\}$ remain zero. This is consistent with (6.12). Also the plastic slips $\{\gamma_3, \gamma_5, \gamma_7, \gamma_8, \gamma_{10}, \gamma_{11}\}$ remain zero in this case, but other choices of I in (6.13) may activate some of these.

Figure 6.6 illustrates the relationship between ε_{12}^p and ε_{12}. The horizontal segments indicate elastic behaviour, consistent with Fig. 6.4. Apparently non-uniqueness occurs only in the plastic slips γ_i.

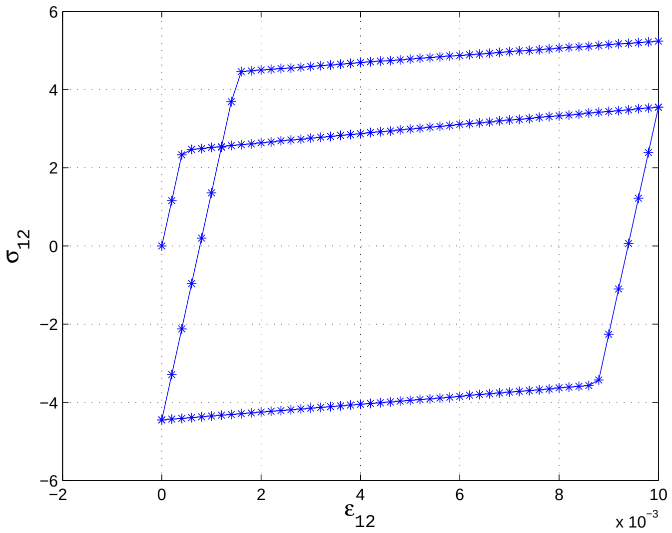

Figure 6.4: Normalized shear stress $\bar{\sigma}_{12}$ vs. shear strain ε_{12}.

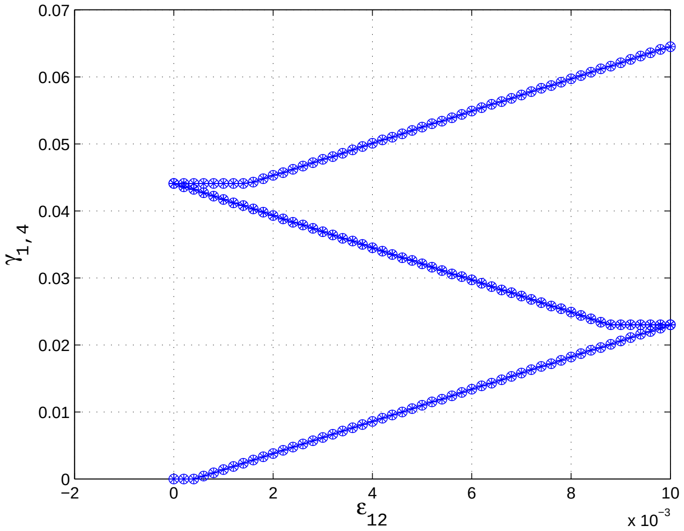

Figure 6.5: Plastic slips γ_1 and γ_4 vs shear strain ε_{12}.

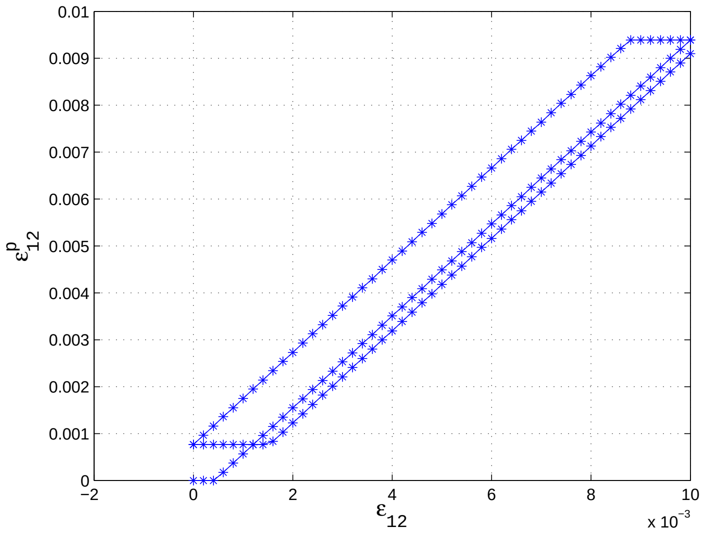

Figure 6.6: Shear plastic strain ε^p_{12} vs shear strain ε_{12}.

6.5 Numerical Example for Uniaxial Loading

Consider the same copper sample of the previous section[5] under the cyclic uniaxial strain loading described by

$$\dot{\boldsymbol{\varepsilon}} = \varepsilon_{11}\boldsymbol{e}_1 \otimes \boldsymbol{e}_1.$$

First the strain rate $\dot{\varepsilon}_{11} = 0.1s^{-1}$ is applied until $\varepsilon_{11} = 0.002$, then the strain rate is reversed to $\dot{\varepsilon}_{11} = -0.1s^{-1}$ until $\varepsilon_{11} = 0$. Finally the strain rate is reversed to $\dot{\varepsilon}_{11} = 0.1s^{-1}$ until $\varepsilon_{11} = 0.002$.

In this case the following holds:

$$\begin{aligned}
|\tau_i| &= |\boldsymbol{\sigma} : \boldsymbol{m}_i| = \frac{1}{\sqrt{6}}|\sigma_{11} - \sigma_{22}|, \quad i = 2, 3, 5, 6, 8, 9, 11, 12, \\
|\tau_i| &= 0, \quad \text{otherwise}.
\end{aligned}$$

---

[5] This means the number of slip systems, the Schmidt tensors and the material constants of the previous example are all the same.

This means eight slip systems will activate first when $\sigma_{11} - \sigma_{22} = \sqrt{6}\tau_{c0}$.

This problem was solved numerically with the same numerical algorithm and data of the previous experiment. The criteria for the choice of the index I corresponding to maximum values of f_i is also the same.

Figures 6.7a−c correspond to relationships between $\{\bar{\sigma}_{11},\ \bar{\sigma}_{22}\}$ vs ε_{11}, $\bar{\sigma}_{11} - \bar{\sigma}_{22}$ vs ε_{11} and $\{\varepsilon^p_{11},\ \varepsilon^p_{22}\}$ vs ε_{11} respectively. Their interpretation is similar to the shear loading experiment of the previous section. The results of the present section and Section 6.4 are in good agreement with [63].

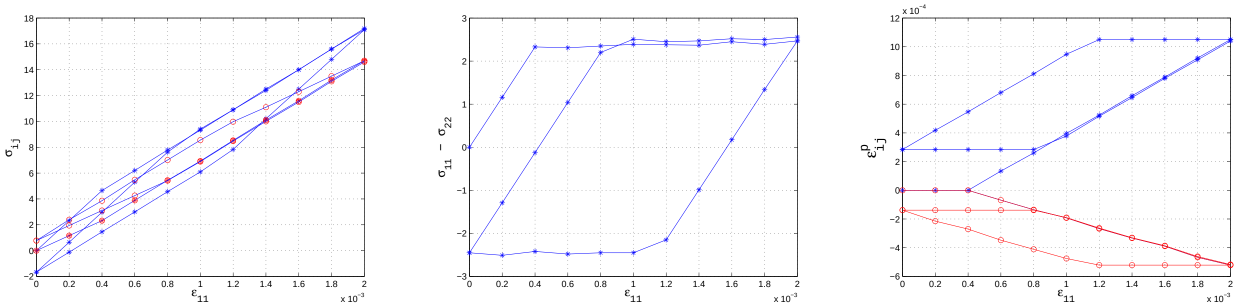

(a) (b) (c)

Figure 6.7: (a) $\{\bar{\sigma}_{11},\ \bar{\sigma}_{22}\}$ vs ε_{11}. (b) $\bar{\sigma}_{11} - \bar{\sigma}_{22}$ vs ε_{11}. (c) $\{\varepsilon^p_{11},\ \varepsilon^p_{22}\}$ vs ε_{11}.

Some Results on Crystal Plasticity at the Nanoscale

In this section the plastic response of thin films at the nanoscale is briefly discussed. Constitutive equations developed in [9] are shown. A closed expression of the dislocation densities in a thin Cu film is presented [23]. The hardening parameters together with the dislocation densities are adapted to the rate independent constitutive equations of single crystal plasticity exposed in previous sections. We end this section with numerical solutions of the stress strain response of a thin Cu film under shear loading. Different film thicknesses are considered in order to aprreciate size effects.

Experiments have shown that the plastic response of metallic thin films is size dependent at the micron or sub micron range. One example is the yield stress, that tends to increase as a characteristic size of the film decreases. This type of relation is known as the Hall-Petch effect. Experimentally it has been found that the yield stress σ_y^H of a film at sub micron levels satisfies

$$\sigma_y^H = \sigma_y + \alpha\mu\frac{b}{h^n},$$

where σ_y is the yield stress of the bulk material, μ the shear modulus, b is the magnitude of Burger's vector, h the film thickness, n is a constant and α a scaling parameter.

Recent experiments have shown there exists a significative difference between the proportional limit and the elastic limit at the sub micron level [27]. Also a strain recovery (not total) after unloading to zero stress has been noticed [51]. The constitutive models we develop in this thesis include the Hall-Petch effect.

6.6 A model for single crystal plasticity

In this section a model for single crystal plasticity is presented [23], [9]. The constitutive equations are applied to describe the shear response of a thin Cu film. It's assumed the film thickness is made of a single grain.

Assume the deformation gradient[6] $\boldsymbol{F}$ can be decomposed in the form[7]

$$\boldsymbol{F} = \boldsymbol{F}^e\boldsymbol{F}^p,$$

---

[6] The deformation gradient $\boldsymbol{F}$ is defined as $\boldsymbol{F} = \boldsymbol{I} + \mathrm{GRAD}\,(\boldsymbol{u})$, where $\boldsymbol{I}$ is the second order identity tensor, $\boldsymbol{u}$ is the displacement vector field and $\mathrm{GRAD}\,(\cdot)$ is the gradient operator respect to the material variable $\boldsymbol{X}$.

[7] This multiplicative decomposition holds for large deformations.

where $\boldsymbol{F}^e$ and $\boldsymbol{F}^p$ are called the elastic part and plastic part of the deformation gradient respectively. $\boldsymbol{F}^e$ is related to the lattice deformation of the crystal and $\boldsymbol{F}^p$ to the cummulative effect of the dislocation motion. The plastic part of the deformation gradient is assumed to satisfy [2], [23]

$$\boldsymbol{F}^p = \boldsymbol{I} + \sum_{\alpha=1}^{N} \gamma^\alpha \boldsymbol{s}^\alpha \otimes \boldsymbol{m}^\alpha,$$

where N is the number of slip systems and γ^α, $\boldsymbol{s}^\alpha$, $\boldsymbol{m}^\alpha$ are the plastic slip, slip direction and normal vector to the slip plane α respectively. The plastic slips are assumed to satisfy

$$\dot{\gamma}^\alpha = \begin{cases} \dot{\gamma}_0^\alpha \left(\tau^\alpha / \tau_y^\alpha\right)^{1/m} & , \text{ if } \tau^\alpha \geq \tau_y^\alpha \\ 0 & \text{otherwise,} \end{cases} \tag{6.13}$$

where $\dot{\gamma}_0^\alpha$ is a reference strain rate, τ^α is the resolved shear stress in slip plane alpha, τ_y^α is the flow stress in slip system α and m is a hardening exponent set to 0.01 in [23].

The flow stress satisfies

$$\dot{\tau}_y^\alpha = \sum_{\beta=1}^{N} h^{\alpha\beta} \dot{\gamma}^\beta, \tag{6.14}$$

where $h^{\alpha\beta}$ are hardening parameters. In [9], [23] it is assumed $h^{\alpha\beta}$ satisfies

$$h^{\alpha\beta} = \frac{a\mu n^\alpha}{\rho^\alpha} \left(\frac{\tau_y^\alpha}{\tau_0^\alpha}\right)^3 \left(\cosh\left(\frac{\tau_0^\alpha}{\tau_y^\alpha}\right)^2 - 1\right) \delta_{\alpha\beta},$$

where $\tau_0^\alpha = a\mu b\sqrt{n^\alpha}$ is a characteristic flow stress [8], a is a constant, n^α is the number of forest dislocations piercing the slip plane α. The number of forest dislocations is assumed to depend on the dislocation densities ρ^α in the following way:

$$n^\alpha = \sum_{\beta=1}^{N} a^{\alpha\beta} \rho^\beta$$

---

[8] This is called Taylor's hardening law.

where $a^{\alpha\beta}$ are constants. For Cu, the numerical values of $a^{\alpha\beta}$ were determined experimentally by Franciosi and Zaoui [12]. The row sum of the matrix $\left(a^{\alpha\beta}\right)$ is always constant, for Cu this sum is approximately 7.7×10^{-2}.

The dislocation density ρ^α satisfies an evolution equation, generally it depends on the initial dislocation density ρ_0, the saturation density ρ_{sat} and the plastic slip γ^α. The following form of the dislocation density was used [23]:

$$\rho^\alpha = \rho_{sat}\bar{\gamma}^\alpha \frac{b}{h}\sqrt{\frac{\left(1-\frac{2x_2}{h}\right)^2}{\left(\frac{x_2}{h}\right)\left(1-\frac{x_2}{h}\right)}} + \rho_0, \tag{6.15}$$

where h is the film thickness, $\bar{\gamma}^\alpha$ is an average plastic strain that depends of time and x_2 is the position along the film thickness. The coordinate system is centered at the bottom of the film. The coordinate axis are parallel to the crystal lattice.

The form of equation (6.15) follows from the phase-field theory of dislocations developed by Koslowski [30], [29], [24].

Now we adapt the above model to the single crystal plasticity model presented in Section 6.3. The following was assumed:

- Define the yield functions by $f^\beta \equiv |\tau^\beta| - \tau_y^\beta$, where

  $$\tau_y^\beta(0) = \tau_{c0} + \frac{b\mu}{h}, \tag{6.16}$$

  is the initial yield stress, τ_{c0} is the yield stress of the bulk material. Note that the yield stress is identical in all slip systems. Also the Hall-Petch effect is incorporated with $n = 1$, $\alpha = 1$.

- The hardening parameters appearing in the evolution equation of the critical resolved shear stress

  $$\dot{\tau}_y^\alpha = \sum_{\beta=1}^{N} h^{\alpha\beta}\dot{\gamma}^\beta,$$

are assumed to satisfy

$$h^{\alpha\beta} = \frac{a\mu n^{\alpha}}{\rho^{\alpha}} \left(\frac{\tau_y^{\alpha}}{\tau_0^{\alpha}}\right)^3 \left(\cosh\left(\frac{\tau_0^{\alpha}}{\tau_y^{\alpha}}\right)^2 - 1\right) \delta_{\alpha\beta}. \tag{6.17}$$

- We assume the dislocation density ρ^{α} satisfies

  $$\rho^{\alpha}(\boldsymbol{x}) = \rho_{sat}\bar{\gamma}^{\alpha}\frac{b}{h}\sqrt{\frac{\left(1-\frac{2x_2}{h}\right)^2}{\left(\frac{x_2}{h}\right)\left(1-\frac{x_2}{h}\right)}} + \rho_0, \tag{6.18}$$

  where $\bar{\gamma}^{\alpha} = 0.3$ is constant[9]. Therefore ρ^{α} is identical in all slip systems. The dislocation density ρ^{α} changes only along the film thickness and tends to increase near the boundaries.

Now we are ready to compute some numerical results.

6.7 Shear Loading of a Thin Crystalline Film

Consider a Cu thin film under shear loading in the $\boldsymbol{e}_1 - \boldsymbol{e}_2$ plane given by

$$\dot{\boldsymbol{\varepsilon}} = \dot{\varepsilon_{12}}\left(\boldsymbol{e}_1 \otimes \boldsymbol{e}_2 + \boldsymbol{e}_2 \otimes \boldsymbol{e}_1\right).$$

The strain rate $\dot{\varepsilon_{12}} = 0.1s^{-1}$ is applied until $\varepsilon_{12} = 0.01$. The following material parameters[10] where taken from [23], [12], [63] and [54]:

---

[9] This value was taken from [23], strictly $\bar{\gamma}^{\alpha}$ changes with time.

[10] Remember Cu has $N = 12$ slip systems.

Poisson's Ratio	ν	$\frac{1}{3}$
Young's Modulus	E	$124GPa$
Magnitude of Burger's vector	b	$0.256nm$
Initial Critical Resolved Shear Stress	τ_{c0}	$16MPa$
	a	0.3
Initial dislocation Density	ρ_0	$10^{11}m^{-2}$
Saturated Dislocation Density	ρ_{sat}	$\frac{8}{\pi b^2}$
	$\sum_{\beta=1}^{12} a^{\alpha\beta}$	7.7×10^{-2}

The numerical algorithm for single crystal plasticity is applied with a constant time step of $\Delta t = 2 \times 10^{-3}s$. The initial conditions at time $t = 0$ are $\boldsymbol{\varepsilon}^p(0) = \mathbf{0}$, $\gamma^\alpha(0) = 0$ and $\tau_y^\alpha(0) = \tau_{c0} + \frac{b\mu}{h}$, for $\alpha = 1, ..., 12$.

The new hardening parameters $h^{\alpha\beta}$ require a modification of (6.10), indeed, the critical resolved shear stress is now updated by solving for $\Delta\tau_y^I$:

$$\frac{\tau_y^I + \Delta\tau_y^I}{\tau_0^I} = \frac{\tau_y^I}{\tau_0^I} + \frac{\Delta\gamma^I a\mu n^I}{\rho^I \tau_0^I} \left(\frac{\tau_y^I + \Delta\tau_y^I}{\tau_0^I} \right)^3 \left(\cosh\left(\frac{\tau_0^I}{\tau_y^I + \Delta\tau_y^I} \right)^2 - 1 \right).$$

Newton's method can be applied. It's convenient to make the change of variable

$$x = \frac{\tau_y^I + \Delta\tau_y^I}{\tau_0^I}, \tag{6.19}$$

then approximate with Newton's method the unique positive zero of $f(x) = 0$, where

$$f(x) = x - \frac{\Delta\gamma^I a\mu n^I}{\rho^I \tau_0^I} x^3 \left(\cosh\left(\frac{1}{x}\right)^2 - 1 \right) - \frac{\tau_y^I}{\tau_0^I}.$$

Initial conditions like $x_0 = \frac{\tau_y^I}{\tau_0^I} + \delta$, where $\delta > 0$ "**sufficiently small**", make Newton's method converge. After knowing the approximate value of x then $\Delta\tau_y^I$ can be approximated using (6.19).

Figure 6.8 shows the relationship between the normalized shear stress

$$\bar{\sigma}_{12} = \frac{\sigma_{12}}{\tau_{c0}},$$

and the shear strain ε_{12} at different levels of a Cu film of thickness $h = 2\mu m$. The horizontal line between 2 and 3 describes the normalized yield stress of the bulk material. Previously it was shown this value is $\sqrt{6}$. The Hall-Petch effect is clear, the yield stress of the Cu film is higher than the yield stress of the bulk material.

From bottom (curve with squares) to top (curve with stars), the normalized shear stress-shear strain responses correspond to $\frac{x_2}{h} = 0.5, 0.6, 0.7, 0.8, 0.9$. Since ρ^α is symmetric respecto to $\frac{x_2}{h} = 0.5$, the responses are identical for $\frac{x_2}{h} = 0.5, 0.4, 0.3, 0.2, 0.1$ respectively. We can appreciate hardening is higher at the boundaries of the film while at the midplane practically we have perfect plasticity. This is an expected result, indeed, from (6.18) we have ρ^α is minimum at the midplane and unbounded near the film boundaries.

Figure 6.9 illustrates the same case of figure 6.8 but for a film thickness of $h = 0.2\mu m$. Since the film thickness is at the submicron level, the size effects are clearly more pronounced. Figures 6.10 and 6.11 correspond to $h = 20\mu m$ and $h = 200\mu m$ respectively. We can appreciate the Hall-Petch effect is reduced as the film thickness increases. When $h = 200\mu m$ the yield stress of the bulk material is practically the same as the yield stress of the film.

6.8 A J_2 model for polycrystals with size effects

The polycrystalline microstructure shown in Fig.5.1 is made up of many crystals with different sizes and orientations. Solving for the mechanical behaviour of the whole device depends on the responses of each individual crystal. This requires an

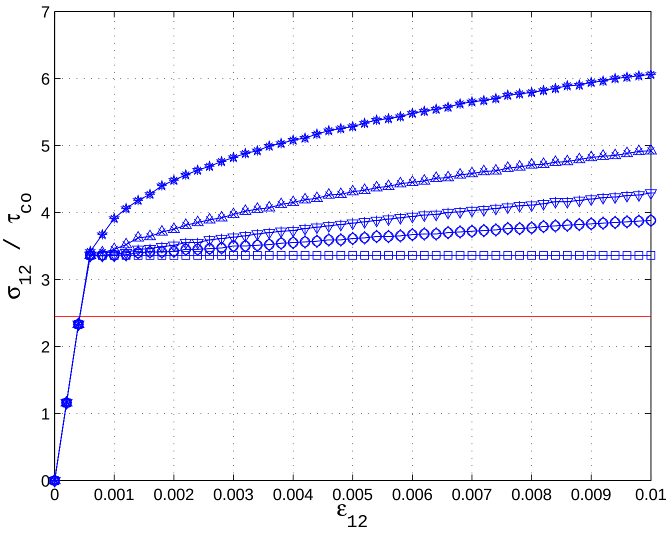

Figure 6.8: $\bar{\sigma}_{12} = \frac{\sigma_{12}}{\tau_{c0}}$ vs ε_{12} for $h = 2\mu m$.

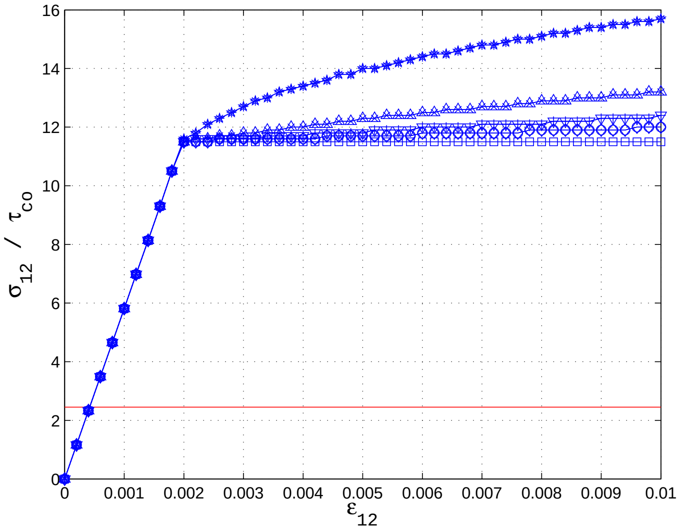

Figure 6.9: $\bar{\sigma}_{12} = \frac{\sigma_{12}}{\tau_{c0}}$ vs ε_{12} for $h = 0.2\mu m$.

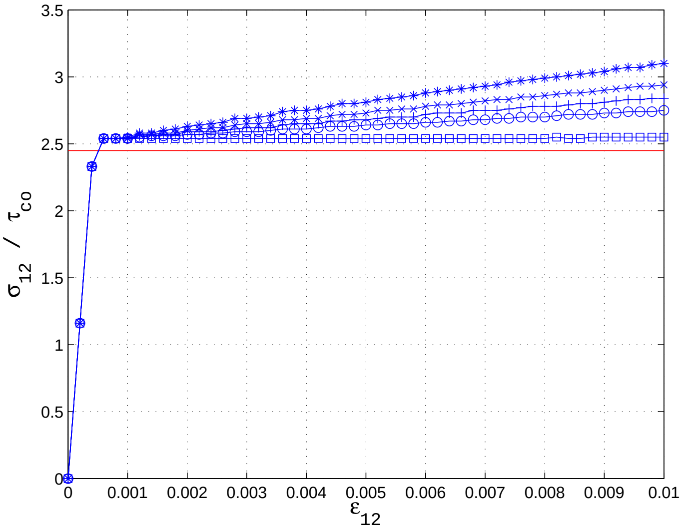

Figure 6.10: $\bar{\sigma}_{12} = \frac{\sigma_{12}}{\tau_{c0}}$ vs ε_{12} for $h = 20\mu m$.

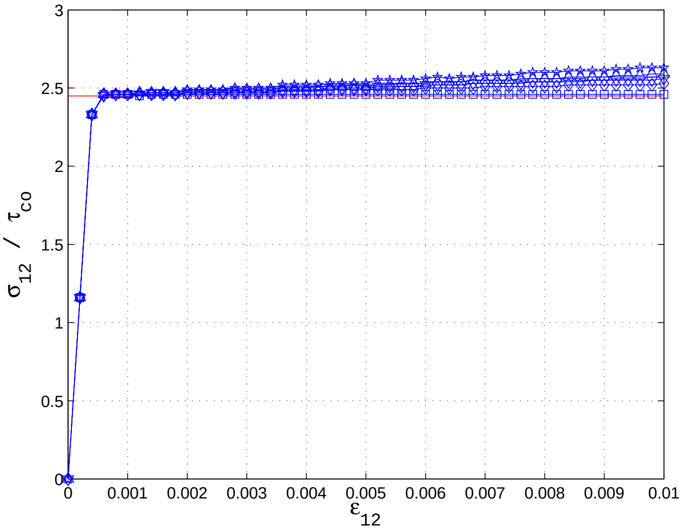

Figure 6.11: $\bar{\sigma}_{12} = \frac{\sigma_{12}}{\tau_{c0}}$ vs ε_{12} for $h = 200\mu m$.

enormous amount of computational effort. To start we assume the overall response of the device can be described with an homogenized theory; that is, there exists a single crystal medium (Effective Medium) that behaves like the polycrystalline medium in average sense.

The rest of this section presents a J_2 model for polycrystals incorporating size effects. The single crystal plasticity model with size effects of the previous section is used to develop a homogenized model by averaging material properties over all grains along the film thickness. The model was developed by Sulsky.

Assume the critical resolved shear stress, plastic slips and dislocation densities are the same in all slip systems (unrealistically), then the yield condition is postulated to satisfy

$$f(\boldsymbol{\sigma}, \tau^c) = (\frac{3}{2}\boldsymbol{\sigma}^d : \boldsymbol{\sigma}^d)^{\frac{1}{2}} - \tau^c(\gamma), \tag{6.20}$$

where the previous equation looks almost the same as the yielding condition (6.4), the main difference resides on the term $J_2 = (\frac{3}{2}\boldsymbol{\sigma}^d : \boldsymbol{\sigma}^d)^{\frac{1}{2}}$ which is the second invariant of the stress tensor, a quantity that remains constant under rotations [56]. This is the reason why we call this theory J_2. As a consequence the plastic behavior of the material is isotropic.

Assuming all plastic slips are identical and the model is associative then it can be shown the flow rule takes the form

$$\dot{\boldsymbol{\varepsilon}}^p = \dot{\gamma}\frac{\boldsymbol{\sigma}^d}{(\boldsymbol{\sigma}^d : \boldsymbol{\sigma}^d)^{\frac{1}{2}}}.$$

Equation (6.18) describes variations of the dislocation density with respect to the vertical position x_2 inside a single crystal. If we want to describe a response for all the polycrystalline aggregate then as a first try we average over the film thickness [11]

---

[11] Strictly it must be averaged over the whole film, but the dislocation density changes only along the film thickness.

and use the following estimate for the dislocation density

$$\begin{aligned}\rho &= \frac{1}{h}\int_0^h \rho^\alpha dx_2 \\ &= 2\rho_{sat}\gamma\frac{b}{h} + \rho_0,\end{aligned} \tag{6.21}$$

where $\overline{\gamma}^\alpha$ was replaced by γ. The replacement of $\overline{\gamma}^\alpha$ by γ was done in order for ρ to increase with time[12].

The assumption ρ is the same for all slip systems implies the number of forest dislocations is the same in all slip systems. The expression for the forest dislocations n simplifies to

$$\begin{aligned}n &= n^\alpha \\ &= A\rho,\end{aligned}$$

where $A = \sum_\beta a^{\alpha\beta}$ is the constant row sum. Also Taylor's law is identical in all slip systems,

$$\begin{aligned}\tau_0 &= \tau_0^\alpha \\ &= a\sqrt{A}\mu b\sqrt{\rho}.\end{aligned}$$

The hardening moduli $h^{\alpha\beta}$ can be approximated to

$$h^{\alpha\beta} = Aa\mu\left(\frac{\tau^c}{\tau_0}\right)^3\left(\cosh\left(\frac{\tau_0}{\tau^c}\right)^2 - 1\right)\delta_{\alpha\beta} \approx \frac{1}{2}Aa\mu\left(\frac{\tau_0}{\tau^c}\right)\delta_{\alpha\beta},$$

where the approximation $\cosh x \approx 1 + \frac{x^2}{2!}$ was used[13]. The critical resolved shear stress evolves in the following way

$$\dot{\tau}^c = \frac{1}{2}Aa\mu\left(\frac{\tau_0}{\tau^c}\right)\dot{\gamma}. \tag{6.22}$$

---

[12] This is a desired property because the dislocation density is an increasing function. In the experiments of the previous section we took $\overline{\gamma}^\alpha$ constant. Still (6.21) is not adequate because theoretically is expected $\rho \rightarrow \rho_{sat}$ as $\gamma \rightarrow \infty$.

[13] Provided $\frac{\tau_0}{\tau^c} \ll 1$. The experiments shown further satisfy this relation.

Finally we assume the initial critical resolved shear stress is identical in all slip systems. This completes the model.

6.9 Numerical examples

In this section we study the mechanical response of a thin Ni film under uniaxial tensile stress. The J_2 model of the previous section is used and solved numerically. Results are compared with real experimental data shown in [18] and [17]. The values of the parameters used in the experiments are shown in the following table

Poisson's Ratio	ν	0.2
Young's Modulus	E	$180GPa$
Magnitude of Burger's vector	b	$2.5 \times 10^{-10}m$
	a	0.3
Initial dislocation Density	ρ_0	$10^{11}m^{-2}$
Saturated Dislocation Density	ρ_{sat}	$4.07m^{-2}$
Row sum of matrix	A	7.6×10^{-2}

The parameters a and A were chosen to fit the data given in [18] and [17]. The initial dislocation density was taken from [23]. Young's modulus comes from [18]. Poisson's ratio and the magnitude of Burger's vector from [54].

Figure 6.12 shows experimental tensile stress-strain curves for as-deposited LIGA Ni and annealed Ni microsamples. The curve at the right corresponds to the annealed sample[14]. The Hall-Petch effect is clear. Grains in the as-deposited Ni sample are smaller than the annealed sample. The as-deposited grain size is $h = 4\mu m$ and the yield stress $\tau_{c0} = 410MPa$ [18]. The annealed yield stress is $120MPa$ and

---

[14] Is the same as-deposited LIGA Ni sample annealed for 1 hour at 800 $°C$.

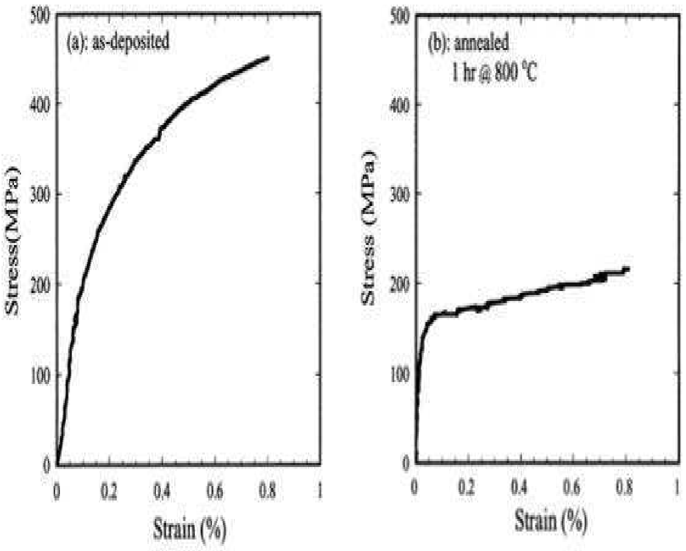

Figure 6.12: Experimental tensile stress-strain curves of an as-deposited LIGA Ni sample (left) and the corresponding annealed Ni microsample (right) [18].

the grain size was taken to be $4 \times 10^{-1} m$. The rate of loading is $\dot{\varepsilon}_{11} = 10^{-4} s^{-1}$. Figures 6.13a–b show the numerical results obtained with the J_2 model for the as-deposited and annealed microsamples respectively.

Figure 6.14 shows experimental tensile stress-strain curves of different as-deposited LIGA Ni microsamples [17]. Curves with higher yield stress correspond to microsamples with smaller grains. It's known from [17] that the curve at the bottom corresponds to grain sizes of $4 \mu m$ and the curve below the one at the top corresponds to grain sizes of $200 nm$. The curve of the bottom is the same as the one shown in Fig. 6.12. It has a yield stress of $410 MPa$.

The gain size and yield stress of the rest of the curves is not available. The values where estimated with "by eye" and linear interpolation. From bottom to top, the second curve was assigned a grain size of $2.48 \mu m$ and a yield stress of $790 MPa$. The third curve was assigned a grain size of $1.85 \mu m$ and yield stress of $930 MPa$. The

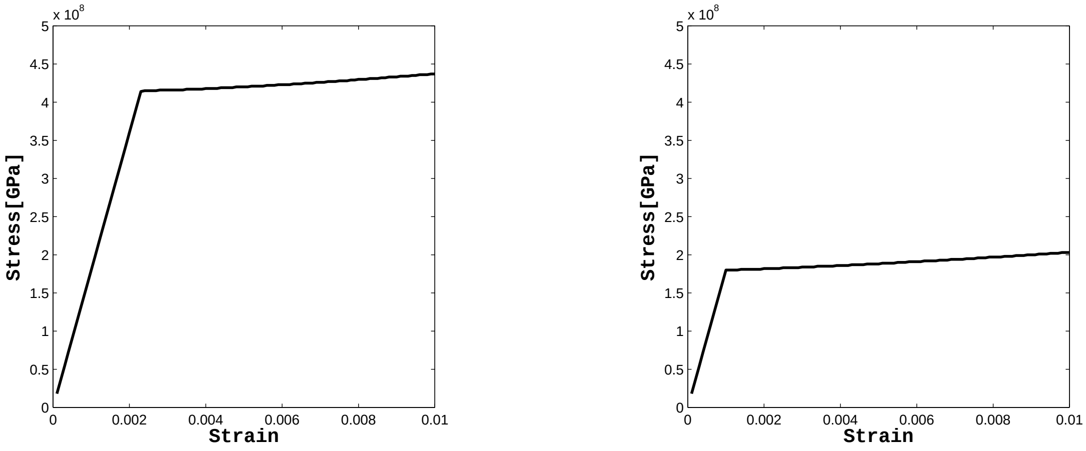

(a)

(b)

Figure 6.13: (a) Tensile stress-strain curve of the J_2 model for the as-deposited LIGA Ni sample. (b) Tensile stress-strain curve of the J_2 model for the annealed Ni microsample.

fourth curve was given a yield stress of $1180MPa$. The fifth curve was assigned a grain size of $160nm$ and a yield stress of $1280MPa$.

Figure 6.15 shows the numerical results obtained with the J_2 model. Note that the plastic behaviour shown in Fig. 6.15 has an upward concavity. Opposite to the downward concavity shown in the real experiments of Fig. 6.14.

Figure 6.16 shows some numerical results obtained by Koslowski [31]. The experiments consider tensile stress loading applied to different as-deposited LIGA Ni microsamples. The grain sizes were available. From bottom to top we have grain sizes of $16nm$, $8nm$ and $4nm$. The yield stress was not available, it was estimated “by eye”. From bottom to top the yield stresses were estimated to be $7.75GPa$, $8.7GPa$ and $9.3GPa$.

Figure 6.17 shows the numerical results obtained with the J_2 model. The grain sizes and yield stresses are the same as Figure 6.16. Note that the stress-strain curves of the J_2 model are close to Koslowski’s stress strain-curves, despite the simplifica-

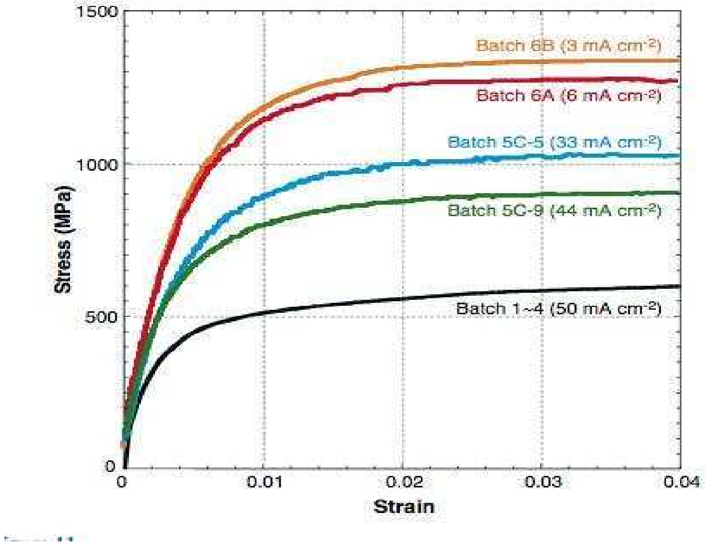

Figure 6.14: Experimental tensile stress-strain curves of different LIGA Ni microsamples [17].

tions done to derive the J_2 model.

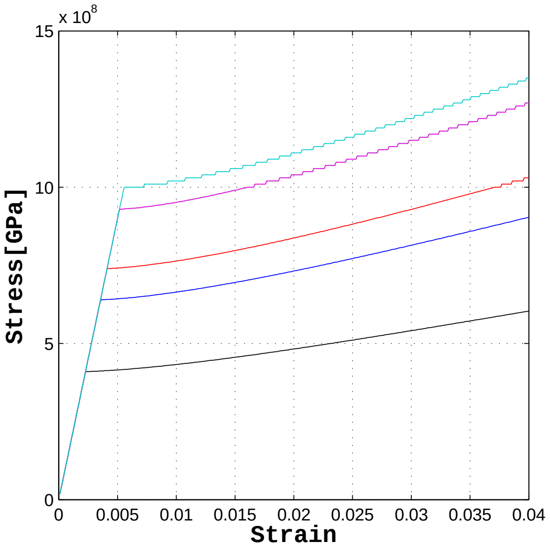

Figure 6.15: J_2 model stress-strain curves of the different as-deposited LIGA Ni microsamples shown in Fig. 6.14.

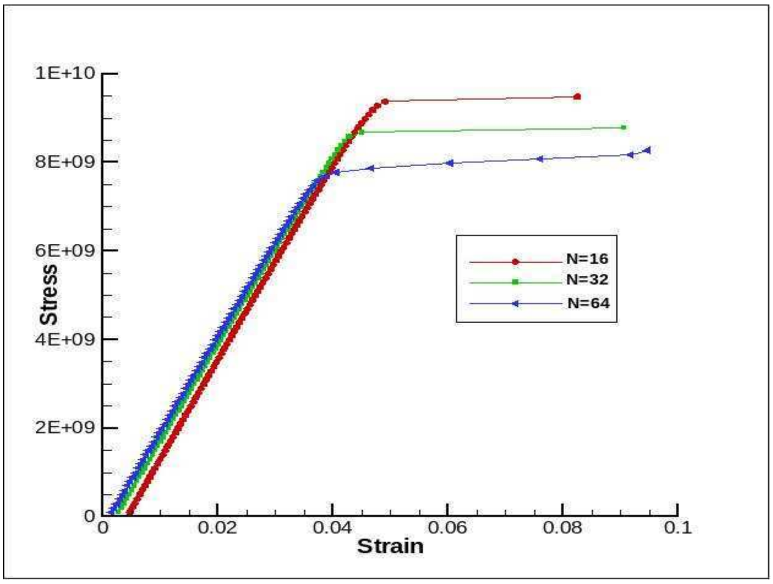

Figure 6.16: Koslowski's stress-strain curves of as-deposited LIGA Ni microsamples. From bottom to top, the considered grain sizes are $16nm$, $8nm$ and $4nm$ [31].

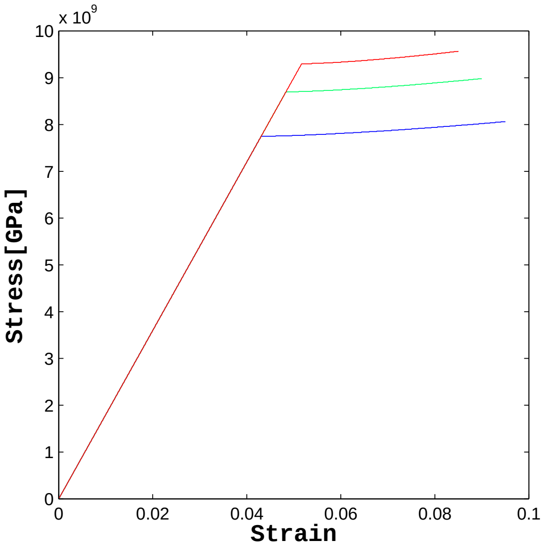

Figure 6.17: J_2 model stress-strain curves of as-deposited LIGA Ni microsamples. The considered grain-sizes are $16nm$, $8nm$ and $4nm$ (from bottom to top).

Chapter 7

Conclusions

In this thesis the mechanical response of the RF MEMS switch illustrated in Fig. 1.1 is studied. In particular, the in-plane Young's modulus and the elastic-plastic behaviour of the thin Ni membrane of the MEMS device are calculated. The methodology to compute the in-plane Young's modulus $E_{in-plane}$ is presented in Chapter 4 and consists in (i) creating a model representative volume element which consists of perfect columnar grains constructed with periodic Voronoi diagrams, (ii) numerically representing experimentally determined crystallographic texture and (iii) simulating uniaxial stress for the computation of $E_{in-plane}$. This methodology is applied to determine not only mean values, but also the full probability distribution of $E_{in-plane}$ by taking into account that the modulus itself depends on uncertainties due to fabrication conditions. In particular, we studied variability of the predicted value of $E_{in-plane}$ due to uncertainties in microstructure geometry, in crystallographic texture, and in single-crystal elastic constants.

In [7] the Reuss average $E^{R}_{in-plane}$, the Hill average $E^{H}_{in-plane}$ and the Voigt average $E^{V}_{in-plane}$ of PRISM MEMS devices are calculated with the MTEX software [19, 40]. The importance of taking into account accurate crystallographic texture is observed and recapitulated in Fig. 4.1. Both the mean value and the range of values are affected if either perfect fiber texture or uniform texture is assumed in place of the experimentally observed texture. In this thesis, we observe that the distribution of $E_{in-plane}$ is not sensitive to microstructure geometry generated by periodic Voronoi diagrams, as shown in Fig. 4.4. The calculated $E_{in-plane}$ moduli are between the Reuss and Voigt averages, an expected result that is proved analytically in Chapter 3. Moreover, the distribution is also not sensitive to the variations in experimentally measured crystallographic texture for the devices in batch #1 of [7], as seen in Table 4.3 and Fig. 4.5. The experimental crystallographic texture has uncertainties up to about 16% measured by misfit. We conclude that MEMS devices coming from the same manufacturing process with fiber crystallographic textures within uncertainty errors of about 16% misfit will tend to have the same in-plane Young's modulus, provided that single-crystal constants are identical for all devices. The PDFs of in-plane Young's modulus show sharply peaked distributions centered at the Hill average value of the modulus. The sharpness of these PDFs illustrates the advantage of using full field simulations to estimate $E_{in-plane}$ compared to using a uniform distribution over allowable values given by the Reuss and Voigt bounds.

We also find that knowledge of the single-crystal elastic moduli is crucial for determining the PDF of $E_{in-plane}$. This observation is demonstrated in Figs. 4.6 and 4.9. The results shown in Fig. 4.6 are based on the assumption that the single-crystal constants (4.11) distribute uniformly randomly within their range. This assumption is not based on experimental evidence, but is an assumption made due to the lack of information about how the values distribute. This PDF of $E_{in-plane}$ is representative of the uncertainty in the in-plane Young's modulus that arises due to imprecise characterization of the crystallites making up the device. The single-crystal constants (4.11) cover a range of values reported in the literature, measured with varying experimental techniques on nickel with different impurities. Similar uncertainty would arise in $E_{in-plane}$ if experimental measurements on actual devices had errors resulting in a range of possible values.

The results shown in Fig. 4.9 are based on more detailed experimental data. An explicit relation between C_{11}, C_{12}, C_{44} and the concentration of copper in the alloy [11], shown in (4.12), is used. Qualitatively, the results in Figs. 4.6 and 4.9 are similar. Uncertainty in single-crystal elastic moduli gives a broad distribution of possible values for $E_{in-plane}$, that is somewhat uniform over its range. Thus, surprisingly, taking into account the correlation between the single-crystal properties, does not substantially reduce the uncertainty in the in-plane Young's modulus.

Device-scale simulations cannot as yet resolve individual grains. So, these simulations require effective material properties to model the response of the device. Since the elastic properties play a role in lifetime and reliability predictions for MEMS devices, the effective properties need to be determined accurately. Furthermore, in order to quantify the uncertainty in lifetime and reliability predictions, the uncertainty in effective properties needs to be quantified as well. Chapter 4 presents a methodology to make predictions of $E_{in-plane}$ for electrodeposited thin films with fiber texture, and to quantify the uncertainty in those predictions.

Device-scale simulations may require a complete numerical geometry model of the complete polycrystalline microstructure. The perfect columnar Voronoi based microstructures of Chapter 4 are approximate small representative volume elements of the top part of the Ni membrane. A Voronoi based algorithm that captures some experimental geometric features of the complete microstructure geometry is proposed in Chapter 5. The experimental features are the grain-size dependence with respect to the film thickness and the log-normal distribution of the in-plane grain sizes. The log-normal in-plane grain-size distribution is generated by exploiting the properties (5.1)−(5.5) of log-normal distributions. An algorithm that generates microstructures with in-plane grain-sizes distributing log-normally is given in Section 5.3. The advantage of this algorithm is that the in-plane grain-sizes of the output microstructures distribute log-normally with mean and s.t.d. values with any degree of accuracy. Unfortunately the in-plane grain geometries are rectangles, an unrealistic cross-section of a microstructure. A typical output of this algorithm is shown in Fig. 5.5.

At the end of Section 5.3 an attempt to generate more realistic microstructure geometries is done in such a way that the log-normal in-plane grain-size distribution generated by the algorithm is still preserved. The idea consists in destroying the rectangular in-plane grain geometries by adding an in-plane perturbation with the expectation that the resulting microstructure cross-sections look similar to Fig. 4.2. Additionally, we destroy the perfect columnar grain structure with the out-of-plane perturbation described in Section 5.2 with the purpose of creating V-shaped grain geometries as indicated in Fig. 5.1. Based on Table 5.1, this idea is tested by generating one microstructure that represents the portion of the polycrystalline membrane that is between the height levels $z = 890nm$ and $z = 1250nm$. The resulting numerical in-plane grain-size distributions are shown in Fig. 5.6 and they match the experimental measurements of Fig. 5.2. Unfortunately the in-plane grain geometries are still unrealistic as shown in Fig. 5.7. Therefore a significant improvement has to be done in this direction.

The plastic behavior of polycrystalline materials is studied in Chapter 6. A J_2 plasticity model for polycrystals is developed in Section 6.8. The J_2 model attempts to describe the overall elastic-plastic behavior of the polycrystalline Ni film and it is derived as follows. The single crystal plasticity model [23, 9], based on the phase-field theory of dislocations of Koslowski, is used to develop a homogenized model by averaging material properties over all grains along the film thickness. The yield condition is assummed to be isotropic, this is mathematically expressed in (6.20). The plastic strain is assumed to be associative and the CRSS, which is assumed to be the only hardening parameter of the effective medium, evolves according to (6.22). The form proposed in (6.22) is a consequence of assuming a unique average dislocation density over the film thickness. This quantity is computed in (6.21). The average dislocation density of the sample leads to a macroscopic medium with identical forms of Taylor's law and identical forest dislocations per slip system. The simplified form of the macroscopic CRSS is obtained from (6.14). The J_2 model has the property that it includes the Hall-Petch size effect by assuming that the CRSS initiates like (6.16).

The J_2 model is numerically solved with the algorithm proposed in Section 6.3. The accuracy of the algorithm is first tested in Sections 6.4 and 6.5 by solving numerically the single crystal plasticity model of Section 6.3. The latter plasticity model has a more general mathematical structure than the J_2 model. In Section 6.4 a single crystal Cu sample under cyclic shear loading is studied. Figures 6.4, 6.5 and 6.6 are obtained with the algorithm of Section 6.3 and they are in good agreement with [63]. In Section 6.5 the same Cu sample is under cyclic uniaxial strain loading and the stress-strain relationships shown in Fig. 6.7 are also in good agreement with [63]. This shows the accuracy of the algorithm and it verifies its implementation.

The incorporation of the Hall-Petch effect in the initial CRSS of the J_2 model is tested on the single crystal plasticity model of Section 6.6. This model describes the plastic behavior of thin single crystal films and is an adaptation of the single crystal plasticity model of [23, 9] to the single crystal plasticity model given in Section 6.3. Section 6.7 considers thin Cu films of different thicknesses (or grain-sizes) under shear loading. Figures 6.8−6.11 illustrate the Hall-Petch size effect at different height levels. The thinner the film thickness, or the smaller the grain-sizes, the higher its yield stress.

After verifying the above, the J_2 model predictions are compared with Koslowski's phase-field simulations and with real tensile stress experiments performed on as-deposited and annealed Ni microsamples. Figure 6.12 shows the experimental tensile stress-strain curves for as-deposited and annealed Ni microsamples. The curve at the left corresponds to the as-deposited case because of the higher yield stress. The J_2 model prediction for the as-deposited Ni microsample is shown in Fig. 6.13a. The curve is obtained by choosing parameters in such a way that the experimental data is fitted the best possible. Parameters like Poisson's ratio, Young's modulus, the magnitude of Burger's vector, the initial dislocation density and the saturated dislocation density are obtained from the literature. Note that the predicted plastic behavior agrees qualitatively with the experiment in terms of energy dissipation and initial yield but not in detail in terms of the shape of the stress-strain response. The right curve of Figure 6.12 corresponds to the annealed case. The J_2 model predictions for the annealed case are shown in Fig. 6.13b. The J_2 model parameters in this case are the same as the ones chosen for the as-deposited case, except for the average grain-size which is bigger in this case. Note that the predicted plastic behavior agrees reasonably well with experiments. The simulated stress-strain curves have less hardening than the experimental stress-strain curves, provided the maximum strain is 0.8%.

Figure 6.14 shows experimental tensile stress-strain curves for different as-deposited Ni microsamples. Curves with higher yield stress correspond to microsamples with smaller grains. The J_2 model predictions are shown in Fig. 6.15. In this case the experimental stress-strain curves are measured up to a maximum strain of 4%, five times higher than the previous maximum strain. The predicted stress-strain curves have more hardening than the experimental curves, additionally the concavities are opposite. The discrepancies between predictions and experiments may be overcome by considering a different type of constitutive model known as a rate-dependent model. This was suggested by Koslowski.

Figure 6.16 shows different tensile stress-strain curves coming from Koslowski's phase-field simulations on as-deposited Ni microsamples. The phase-field model predicts the yield stresses based on dislocation information and grain-sizes. The J_2

model results are shown in Figure 6.17. The grain-sizes and yield stresses are are the same as Fig. 6.16. Note that the stress-strain curves of the J_2 model are in good agreement with the phase-field simulations, despite the simplifications done to derive it.

Appendices

Appendix A

The X-Ray Diffraction Method

X-rays are a form of electromagnetic radiation whose wavelengths range from $0.01nm$ to $10nm$. Usually crystals have lattice constants that are on the order of angstroms (tenths of nanometers). Since the crystal lattice parameters are almost of the same order of magnitude as X-ray wavelengths, X-rays diffract in all directions when they pass through a crystal lattice. The diffraction intensities provide information on the positions of the atoms that form the crystal. Once knowing the location of atoms in the crystal lattice, the crystal's orientation can be calculated. In this Appendix we give a brief explanation of how XRD intensities are useful for measuring crystal orientations.

For simplicity the diagrams shown below represent two dimensional crystals but the ideas illustrated in them apply to three dimensional crystals. Assume an X-ray source S emits X-rays with a wavelength λ onto a crystal. A schematic representation of this situation is shown in Fig. A.1. X-rays are electromagnetic waves that are composed of oscillating magnetic and electric fields of the same oscillation frequency. The oscillation frequency ν of the electromagnetic fields is known as the the X-ray frequency and it satisfies the relation $c = \lambda\nu$ where λ is the X-ray wavelength and

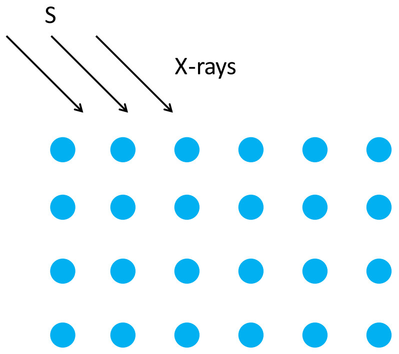

Figure A.1: X-rays incident on a crystal lattice.

c is the speed of light which depends on the properties of the medium where the electromagnetic waves are traveling.

Once the electromagnetic fields enter the crystal lattice they exert forces on the nuclei and electrons of all atoms. The forces oscillate with the same frequency as the electromagnetic waves and these forces mostly influence the electrons because they are much lighter than the nuclei. The vibrating electrons are behaving like small harmonic oscillators, where the electron vibration frequency is ν. As a consequence the vibrating electrons now behave like point sources emitting electromagnetic radiation in all directions. The electromagnetic waves emitted by the electrons interact with each other causing wave interference. At some points in space the interference is constructive and at other points it is destructive or a combination of both. It is difficult to give a mathematical description of this physical process (diffraction pattern) in detail. Fortunately in 1912, the physicist Sir William Lawrence Bragg (1890-1971) showed that the periodic arrangement of crystal atoms can be seen like

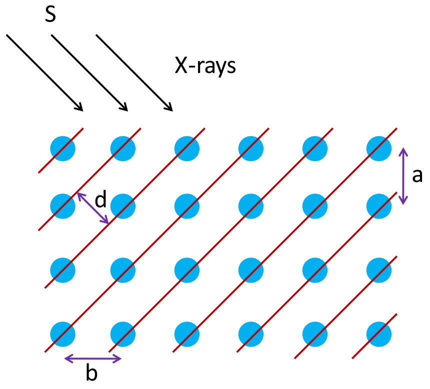

Figure A.2: Bragg's lattice plane interpretation.

an arrangement of lattice planes. This idea is illustrated in Fig. A.2. Lattice planes are always separated by the same distance d known as the interplanar spacing. These planes have the property of reflecting incident X-rays with the same angle of incidence. The choices of lattice planes is not unique. Bragg pointed out that reflection from all sets of lattice planes must be considered in the XRD analysis.

The crystal lattice planes reflect X-rays with different electromagnetic intensities. High electromagnetic intensities occur because of constructive interference and low electromagnetic intensities because of destructive interference. The intensity with which the lattice planes reflect depends of the X-ray incidence angle. Bragg discovered a physical law, now known as Bragg's Law, that relates the X-ray incidence angles and the lattice planes that reflect the highest electromagnetic intensities. Before formulating Bragg's law let's consider the following proposition:

Proposition 1. *Assume a source S emits X-rays onto a lattice plane with an incidence angle θ. If all rays emitted by S are in-phase then an observer O will detect*

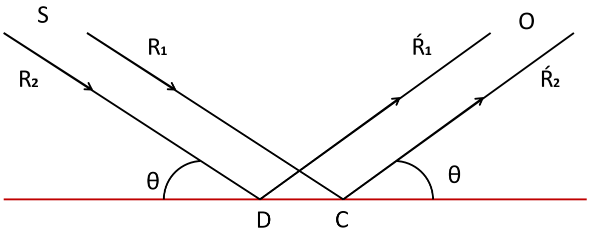

Figure A.3: In-phase X-rays incident on the same lattice plane.

only in-phase reflected rays.

The justification for this principle follows inmediately from Fig. A.3. Note that rays R_1 and R_2 are traveling at the speed of light; so they travel the same distances in the same amount of time. It follows that both rays are incident on the lattice plane at the same time at points C and D respectively. From Snell–Descartes law we have that R_1 and R_2 reflect at the same angle of reflection θ into the rays $R_1^{'}$ and $R_2^{'}$ respectively. Rays $R_1^{'}$ and $R_2^{'}$ have the speed of light and they travel the same distances in the same amount of time. Therefore the observer O detects rays $R_1^{'}$ and $R_2^{'}$ approaching at the same time, in other words, O will see in-phase reflected rays.

Proposition 2. *Assume a source S emits X-rays onto a family of parallel lattice planes P_1, $P_2, \ldots$ of interplanar spacing d at an incidence angle θ. Then an observer O will detect the reflected rays of maximum intensity if and only if $2d\sin\theta = m\lambda$, where m is an integer and λ is the X-ray wavelength.*

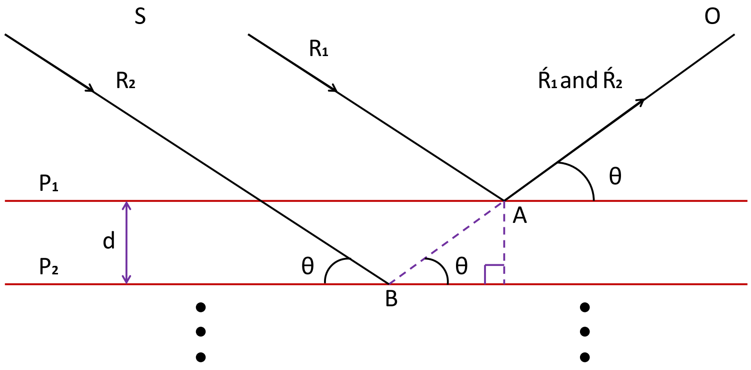

Figure A.4: In-phase X-rays incident on different lattice planes.

In Fig. A.4 we illustrate schematically the source S emitting X-rays at an incidence angle θ onto a family of lattice planes P_1, $P_2, \ldots$. It is important to mention that some of the incident rays can pass through P_1, P_1 and P_2 or any number of consecutive lattice planes. The reason is because the lattice planes do not form a continuum, in reality there is a periodic arrangement of atoms separated by the lattice parameters. The separations between atoms allow some of the X-rays to pass through the lattice planes.

Note from Fig. A.4 that ray R_1 reflects on plane P_1 at point A and ray R_2 reflects on plane P_2 at point B. The reflected rays are denoted by $R_1^{'}$ and $R_2^{'}$ respectively. Note that the reflected rays are now out of phase. This happens because ray $R_2^{'}$ travels a longer distance than ray $R_1^{'}$, meaning that the observer O will detect $R_2^{'}$ delayed with respect to $R_1^{'}$. We can see from the geometry of the figure that the extra distance traveled by $R_2^{'}$ is between the lattice planes P_1 and P_2 and is given by $2d \sin\theta$. This means that the rays $R_1^{'}$ and $R_2^{'}$ will be in-phase if and only if the

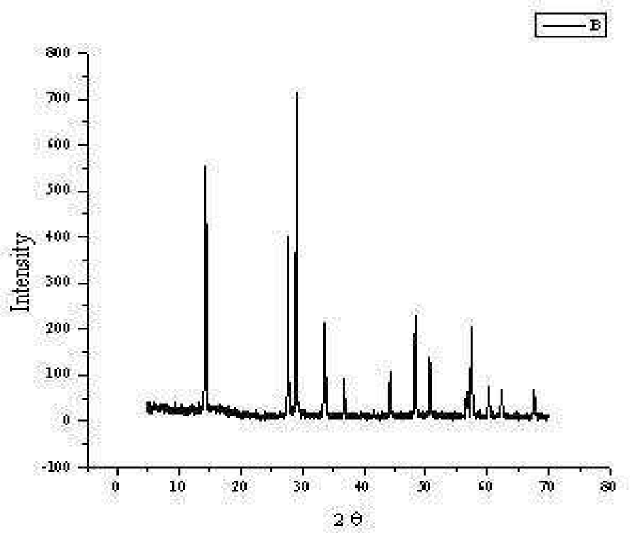

Figure A.5: Intensity peak plot.

distance $2d \sin \theta$ is a multiple of the X-ray wavelength λ. Therefore O will detect constructive interference if and only if $2d \sin \theta = m\lambda$, where m is an integer.

The relation

$$2d \sin \theta = m\lambda,$$

is known as Bragg's law. In practice the source S is an X-ray source, the observer O is a camera or device that measures electromagnetic intensity and the lattice planes correspond to a crystal living in a polycrystalline sample. According to Bragg's law, the intensities measured by O vary with the incident angle θ.

In an XRD experiment the camera O rotates at different angles θ and measures the electromagnetic intensities as a function of θ. The result is a plot like the one shown in Fig. A.5, known as the intensity peak plot. The vertical axis represents the intensity and the horizontal axis the angle 2θ. It has been observed that the intensity peaks always correspond to $m = 1$, higher modes ($m > 1$) are too weak to

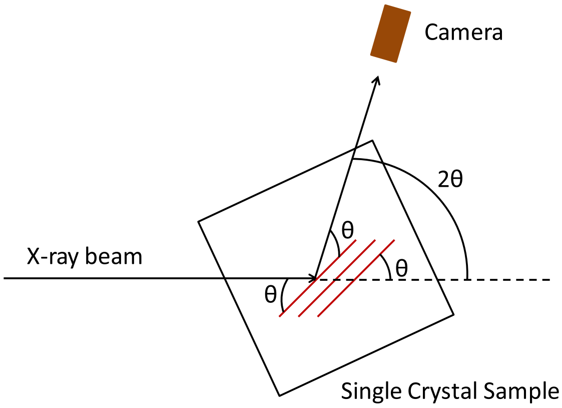

Figure A.6: Measurement of a crystal orientation with the XRD method.

be detected.

The reason why the horizontal axis of an intensity peak plot is 2θ and not θ can be understood from Fig. A.6. Note that X-rays are incident with an angle θ on the lattice planes of a crystal but there is an extra angle θ measured from the incident X-rays. Then the camera measures intensities at an angle 2θ measured from the incident rays.

The high peaks of the intensity plot correspond to constructive interference and therefore they satisfy Bragg's law. The high peaks appearing at different angles correspond to reflections from different lattice planes. We provide an example of how to estimate the lattice planes from the scatter plot for the case when the sample is a single crystal. For polycrystalline samples the process of measuring crystal orientations is more complicated but in principle follows the methodology we show in the next example.

Example A.0.1. *A single crystal Cu sample is studied with XRD. The wavelength of the X-ray beam is $\lambda = 0.154nm$ and the first high peak of the intensity peak plot occurs at $2\theta = 33.6°$. What is the lattice parameter of Cu? What are the Miller indices for this peak? Another peak occurs at $2\theta = 43.2°$, what are the Miller indices for this peak? The two peaks give an idea of the crystal orientation with respect to the sample, are these orientations consistent? Use the information that Cu is an FCC cubic crystal.*

Solution. We know that Bragg's law is satisfied at intensity peaks, then

$$2d_{hkl}\sin\theta = \lambda,$$

where d_{hkl} is the interplanar spacing of lattice planes (hkl). We need to determine the values of the integers h, k, l. We know from [4] that for cubic crystals

$$d_{hkl} = \frac{a}{\sqrt{h^2+k^2+l^2}},$$

where a is the lattice parameter. So we do not know the lattice parameter a of Cu and the Miller indices (hkl). In this case Bragg's law can be expressed in the following form

$$\sin\theta = \frac{\sqrt{h^2+k^2+l^2}}{2a}\lambda.$$

Note that θ is smallest when $\sqrt{h^2+k^2+l^2}$ has the smallest value. Since h, k, l are integers, the smallest possible value occurs when $h^2+k^2+l^2 = 1$, or when $h = k = 0$, $l = 1$ or any equivalent combination described by the family (001). If this is the case then

$$\begin{aligned} a &= \frac{\lambda}{2\sin\theta} \\ &= \frac{0.154nm}{2\sin\frac{33.6°}{2}} \\ &\approx 0.362nm. \end{aligned}$$

The lattice parameter $a \approx 0.362nm$ can be checked in any crystallography table, for example see the reference [26], pg. 296, Table 7.6 . Note that this information is sufficient to measure the crystal orientation, indeed, the incident X-rays form an angle of $90^\circ - 16.8^\circ$ with one of the (001) plane normals. Usually the first peak of the intensity peak plot is used to determine the lattice parameters.

Now we calculate the Miller indices corresponding to the peak located at the angle $2\theta = 43.2^\circ$. From Bragg's law we have

$$\begin{aligned}\sqrt{h^2+k^2+l^2} &= \frac{2a}{\lambda}\sin\theta \\ &= \frac{2\cdot 0.362nm}{0.154nm}\sin\frac{43.2^\circ}{2} \\ &\approx 1.73\end{aligned}$$

then $h^2+k^2+l^2 \approx 3$. The Diophantine equation (polynomial equation restricted to the set of integers)

$$h^2+k^2+l^2 = 3$$

has solution only when $h = k = l = 1$. Therefore the Miller indices for the peak located at $2\theta = 43.2^\circ$ are (111). If we draw a picture of the (001) lattice planes and the (111) planes with their respective angle of incidence θ, we can easily see that both orientations are consistent with each other. ◀

References

[1] Alina Alexeenko. Introduction to Uncertainty Quantification. Online Course, Aeronautics and Astronautics, Purdue University, Fall 2010.

[2] R. J. Asaro. *Micromechanics of Crystals and Polycrystals.* Academic Press Inc., Division of Engineering, Brown University, 1983.

[3] J. F. W. Bishop and R. Hill. A Theory of the Plastic Distortion of a Polycrystalline Aggregate Under Combined Stresses. *Philosophical Magazine*, 42:414–427, February 1951.

[4] Walter Borchardt-Ott. *Crystallography.* Springer, Berlin Heidelberg, 1995.

[5] R. Brenner, R. A. Lebensohn, and O. Castelnau. Elastic Anisotropy and Yield Surface Estimates of Polycrystals. *International Journal of Solids and Structures*, 46:3018–3026, August 2009.

[6] Hans Joachim Bunge. *Texture Analysis in Materials Science: Mathematical Methods.* Butterworth-Heinemann, 1983.

[7] Patrick R. Cantwell, Hojin Kim, Matthew M. Schneider, Hao-Han Hsu, Dimitrios Peroulis, Eric. A. Stach, and Alejandro Strachan. Estimating the In-Plane Young's Modulus of Polycrystalline Films in MEMS. *Journal of Microelectromechanical Systems*, 21:840–849, August 2012.

[8] Pavlo Y. Cholach and Douglas R. Schmitt. Intrinsic Elasticity of a Textured Transversely Isotropic Muscovite Aggregate: Comparisons to the Seismic Anisotropy of Schists and Shales. *Journal of Geophysical Research:Solid Earth*, 111:1–18, 2006.

[9] A. M. Cuitiño and M. Ortiz. Computational Modeling of Single Crystals. *Modelling and Simulation in Materials Science and Engineering*, 1:225–263, April 1993.

[10] Mohamed Gad el Hak. *MEMS: Applications.* CRC Press, Boca Raton, FL, 2006.

[11] S. G. Epstein and O. N. Carlson. The Elastic Constants of Nickel-Copper Alloy Single Crystals. *Acta Metallurgica*, 13:487–491, May 1965.

[12] P. Franciosi and A. Zaoui. Multislip in FCC Crystals a Theoretical Approach Compared with Experimental Data. *Acta Metallurgica*, 30:1627–1637, January 1982.

[13] I. M. Gelfand. *Lectures on Linear Algebra.* Dover Publications, New York, 1989.

[14] Yajuan Guo, Jianfeng Jia, Xiao-Hua Wang, Ying Ren, and Haishun Wu. Prediction of Thermodynamically Reversible Hydrogen Storage Reactions in the KBH4/M(M = Li, Na, Ca)(BH4)n(n = 1,2) System from First-Principles Calculation. *Chemical Physics*, 418:22–27, 2013.

[15] Z. Hashin and S. Shtrikman. On Some Variational Principles in Anisotropic and Nonhomogeneous Elasticity. *Journal of the Mechanics and Physics of Solids*, 10:335–342, October-December 1962.

[16] Z. Hashin and S. Shtrikman. A Variational Approach to the Theory of the Elastic Behaviour of Polycrystals. *Journal of the Mechanics and Physics of Solids*, 10:343–352, October-December 1962.

[17] K. J. Hemker and W. N. Sharpe, Jr. . Microscale Characterization of Mechanical Properties. *Annual Review of Materials Research*, 37:93–126, 2007.

[18] K. J. Hemker and H. Last. Microsample Tensile Testing of LIGA Nickel for MEMS Applications. *Materials Science and Engineering: A*, 319-321:882–886, December 2001.

[19] R. Hielscher and H. Schaeben. A Novel Pole Figure Inversion Method: Specification of the MTEX Algorithm. *Journal of Applied Crystallography*, 41:1024–1037, 2008.

[20] R. Hill. The Elastic Behaviour of a Crystalline Aggregate. *Proceedings of the Physical Society of London: Section A*, 65:349–355, 1952.

[21] John P. Hirth and Jens Lothe. *Theory of Dislocations*. John Wiley and Sons, 1982.

[22] D. Hull and D. J. Bacon. *Introduction to Dislocations*. Butterworth-Heinemann, 2001.

[23] Abigail Hunter, H. Kavuri, and Marisol Koslowski. A Continuum Plasticity Model that Accounts for Hardening and Size Effects in Thin Films. *Modelling and Simulation in Materials Science and Engineering*, 18:1–11, June 2010.

[24] Abigail Hunter and Marisol Koslowski. Direct Calculations of Material Parameters for Gradient Plasticity. *Journal of the Mechanics and Physics of Solids*, 56:3181–3190, November 2008.

[25] Gianluca Iaccarino. Introduction to Uncertainty Quantification. Mechanical Engineering and Institute for Computational Mathematical Engineering, Stanford University (course), April 15-16 2011.

[26] Maureen M. Julian. *Foundations of Crystallography with Computer Applications*. CRC Press, 2008.

[27] N. Karanjgaokar, K. Jonnalagadda, I. Chasiotis, J. Chee, A. Mahmood, and D. Peroulis. Mechanical Behavior of Nanocrystalline Au Films as a Function of Strain Rate and Film Thickness. *Conference: SEM XI International Congress and Exposition on Experimental and Applied Mechanics*, June 2-5 2008.

[28] U. F. Kocks, C. N. Tomé, and H.-R. Wenk. *Texture and Anisotropy: Preferred Orientations in Polycrystals and their Effect on Materials Properties.* Cambridge University Press, 1998.

[29] M. Koslowski. Scaling Laws in Plastic Deformation. *Philosophical Magazine*, 87:1175–1184, March 2007.

[30] M. Koslowski, A. Cuitiño, and M. Ortiz. A Phase-Field Theory of Dislocations Dynamics, Strain Hardening and Hysteresis in Ductile Single Crystals. *Journal of the Mechanics and Physics of Solids*, 50:2597–2635, December 2002.

[31] Marisol Koslowski. Micromechanics. TST Meeting presentation at the NNSA PRISM Center, Purdue University, U.S.A., May 13-14 2010.

[32] Jack B. Kuipers. *Quaternions and Rotation Sequences: A Primer with Applications to Orbits, Aerospace and Virtual Reality.* Princeton University Press, 1999.

[33] R. A. Lebensohn. N-Site Modelling of a 3D Viscoplastic Polycrystal Using Fast Fourier Transform. *Acta Materialia*, 49:2723–2737, August 2001.

[34] R. A. Lebensohn, Y. Liu, and P. Ponte Castañeda. Macroscopic Properties and Field Fluctuations in Model Power-Law Polycrystals: Full-Field Solutions Versus Self-Consistent Estimates. *Proceedings of the Royal Society A*, 460:1381–1405, 2004.

[35] Ricardo A. Lebensohn, Anand K. Kanjarla, and Philip Eisenlohr. An Elasto-Viscoplastic Formulation Based on Fast Fourier Transforms for the Prediction

of Micromechanical Fields in Polycrystalline Materials. *International Journal of Plasticity*, 32-33:59–69, May 2012.

[36] H. M. Ledbetter and R. P. Reed. Elastic Properties of Metals and Alloys, I. Iron, Nickel, and Iron-Nickel Alloys. *Journal of Physical and Chemical Reference Data*, 2:531–617, 1973.

[37] Jacob Lubliner. *Plasticity Theory.* Dover publications, 2008.

[38] L. Lutterotti, M. Bortolotti, G. Ischia, I. Lonardelli, and H.-R. Wenk. Rietveld Texture Analysis from Diffraction Images. *Zeitschrift Fur Kristallographie*, 26:125–130, 2007.

[39] Sergey Edward Lyshevski. *Nano- and Micro-Electromechanical Systems: Fundamentals of Nano- and Microengineering.* CRC Press, 2005.

[40] D. Mainprice, R. Hielscher, and H. Schaeben. Calculating Anisotropic Physical Properties from Texture Data Using the MTEX Open-Source Package. *Journal of the Geological Society*, 360:175–192, 2011.

[41] Nadim Maluf and Kirt Williams. *An Introduction to Microelectromechanical Systems Engineering.* Artech House, 1999.

[42] Jerrold E. Marsden and Thomas J. R. Hughes. *Mathematical Foundations of Elasticity.* Dover Publications, 1983.

[43] M. D. McKay, R. J. Beckman, and W. J. Conover. A Comparison of Three Methods for Selecting Values of Input Variables in the Analysis of Output from a Computer Code. *Technometrics*, 21:239–245, May 1979.

[44] Maxime A. Melchior and Laurent Delannay. A Texture Discretization Technique Adapted to Polycrystalline Aggregates with Non-Uniform Grain Size. *Computational Materials Science*, 37:557–564, October 2006.

[45] J. C. Michel, H. Moulinec, and P. Suquet. A Computational Scheme for Linear and Non-Linear Composites with Arbitrary Phase Contrast. *International Journal for Numerical Methods in Engineering*, 52:139–160, 2001.

[46] A. Morawiec. Review of Deterministic Methods of Calculation of Polycrystal Elastic Constants. *Textures and Microstructures*, 22:139–167, 1994.

[47] H. Moulinec and P. Suquet. A Numerical Method for Computing the Overall Response of Nonlinear Composites with Complex Microstructure. *Computer Methods in Applied Mechanics and Engineering*, 157:69–94, 1998.

[48] Jayathi Murthy. Center Overview. TST Meeting presentation at the NNSA PRISM Center, Purdue University, U.S.A., August 28 2008.

[49] Committee on Mathematical Foundations of Verification, Validation, and Uncertainty Quantification; Board on Mathematical Sciences and Their Applications, Division on Engineering and Physical Sciences, National Research Council. *Assessing the Reliability of Complex Models: Mathematical and Statistical Foundations of Verification, Validation, and Uncertainty Quantification.* National Research Council of the National Academies, 2012.

[50] Kenneth A. Peterson, Paiboon Tangyunyong, and Alejandro A. Pimentel. Failure Analysis of Surface-Micromachined Microengines. *Proceedings SPIE 3512, Materials and Device Characterization in Micromachining*, September 1 1998.

[51] Jagannathan Rajagopalan, Jong H. Han, and M. Taher A. Saif. Plastic Deformation Recovery in Freestanding Nanocrystalline Aluminum and Gold Thin Films. *Science*, 315:1831–1834, March 2007.

[52] Valerie Randle and Olaf Engler. *Introduction to Texture Analysis: Macrotexture, Microtexture and Orientation Mapping.* Gordon and Breach Science Publishers, August 7 2000.

[53] A. Reuss. Account of the Liquid Limit of Mixed Crystals on the Basis of the Plasticity Condition for Single Crystal. *Zeitschrift Fur Angewandte Mathematik Und Mechanik*, 9:49–58, 1929.

[54] D. Rodney, G. Martin, and Y. Bréchet. Irradiation Hardening by Interstitial Loops: Atomistic Study and Micromechanical Model. *Materials Science and Engineering: A*, 309-310:198–202, July 2001.

[55] J. Sakurai, M. Fujii, Y. Nakamura, and H. Takaki. Elastic Constants of Ni-Fe and Ni-Cu Alloys. *Journal of the Physical Society of Japan*, 19:308–310, March 1964.

[56] J. C. Simo and T. J. R. Hughes. *Computational Inelasticity.* Interdisciplinary Applied Mathematics, Mechanics and Materials, Springer, 1998.

[57] Laura P. Swiler, Thomas L. Paez, and Randall L. Mayes. Epistemic Uncertainty Quantification Tutorial. In *Proceedings of the IMAC-XXVII*, February 9-12 2009.

[58] Ellad B. Tadmor, Ronald E. Miller, and Ryan S. Elliott. *Continuum Mechanics and Thermodynamics: From Fundamental Concepts to Governing Equations.* Cambridge University Press, 2012.

[59] Thomas C. T. Ting. *Anisotropic Elasticity: Theory and Applications.* Oxford University Press, 1996.

[60] Vijay K. Varadan, A. Sivathanu Pillai, Debashish Mukherji, Mayank Dwivedi, and Linfeng Chen. *Nanoscience and Nanotechnology in Engineering.* World Scientific, 2010.

[61] W. Voigt. *Lehrbuch der Kristallphysik.* B.G. Teubner, 1928.

[62] J. Peter Watt. Hashin-Shtrikman Bounds on the Effective Elastic Moduli of Polycrystals with Orthorhombic Symmetry. *Journal of Applied Physics*, 50:6290–6295, April 1979.

[63] Q. H. Zuo. On the Uniqueness of a Rate-Independent Plasticity Model for Single Crystals. *International Journal of Plasticity*, 27:1145–1164, August 2011.